A hybrid localization method for Wireless Capsule Endoscopy (WCE)

A Thesis Submitted to the College of Graduate and Postdoctoral Studies
in Partial Fulfillment of the Requirements
for the Degree of Doctor of Philosophy
in the Department of Electrical and Computer Engineering
University of Saskatchewan
Saskatoon

By

Seyed Shahim Vedaei

PERMISSION TO USE

In presenting this thesis in partial fulfillment of the requirements for a Postgraduate degree from the University of Saskatchewan, I agree that the Libraries of this University may make it freely available for inspection. I further agree that permission for copying of this thesis/dissertation in any manner, in whole or in part, for scholarly purposes may be granted by the professor or professors who supervised my thesis/dissertation work or, in their absence, by the Head of the Department or the Dean of the College in which my thesis work was done. It is understood that any copying or publication or use of this thesis/dissertation or parts thereof for financial gain shall not be allowed without my written permission. It is also understood that due recognition shall be given to me and to the University of Saskatchewan in any scholarly use which may be made of any material in my thesis/dissertation.

Requests for permission to copy or to make other uses of materials in this thesis/dissertation in whole or part should be addressed to:

Head of the Department of Electrical and Computer Engineering
57 Campus Drive
University of Saskatchewan
Saskatoon, Saskatchewan S7N 5A9 Canada

OR

Dean
College of Graduate and Postdoctoral Studies
University of Saskatchewan
116 Thorvaldson Building, 110 Science Place
Saskatoon, Saskatchewan S7N 5C9 Canada

DISCLAIMER

Reference in this thesis/dissertation to any specific commercial product, process, or service by trade name, trademark, manufacturer, or otherwise, does not constitute or imply its endorsement, recommendation, or favoring by the University of Saskatchewan. The views and opinions of the author expressed herein do not state or reflect those of the University of Saskatchewan, and shall not be used for advertising or product endorsement purposes

ABSTRACT

Wireless capsule endoscopy (WCE) is a well-established diagnostic tool for visualizing the Gastrointestinal (GI) tract. WCE provides a unique view of the GI system with minimum discomfort for patients. Doctors can determine the type and severity of abnormality by analyzing the taken images. Early diagnosis helps them act and treat the disease in its earlier stages. However, the location information is missing in the frames. Pictures labeled by their location assist doctors in prescribing suitable medicines. The disease progress can be monitored, and the best treatment can be advised for the patients. Furthermore, at the time of surgery, it indicates the correct position for operation. Several attempts have been performed to localize the WCE accurately. Methods such as Radio frequency (RF), magnetic, image processing, ultrasound, and radiative imaging techniques have been investigated. Each one has its strengths and weaknesses. RF-based and magnetic-based localization methods need an external reference point, such as a belt or box around the patient, which limits their activities and causes discomfort. Computing the location solely based on an external reference could not distinguish between GI motion from capsule motion. Hence, this relative motion causes errors in position estimation. The GI system can move inside the body, while the capsule is stationary inside the intestine. This proposal presents two pose fusion methods, Method 1 and Method 2, that compensate for the relative motion of the GI tract with respect to the body. Method 1 is based on the data fusion from the Inertial measurement unit (IMU) sensor and side wall cameras. The IMU sensor consists of 9 Degree-Of-Freedom (DOF), including a gyroscope, an accelerometer, and a magnetometer to monitor the capsule's orientation and its heading vector (the heading vector is a three-dimensional vector pointing to the direction of the capsule's head). Four monochromic cameras are placed at the side of the capsule to measure the displacement. The proposed method computes the heading vector using IMU data. Then, the heading vector is fused with displacements to estimate the 3D trajectory. This method has high accuracy in the short term. Meanwhile, due to the accumulation of errors from side wall cameras, the estimated trajectory tends to drift over time. Method 2 was developed to resolve the drifting issue while keeping the same positioning error. The capsule is equipped with four side wall cameras and a magnet. Magnetic localization acquires the capsule's global position using 9 three-axis Hall effect sensors. However, magnetic localization alone cannot distinguish between the capsule's and GI tract's motions. To overcome this issue and increase tracking accuracy, side wall cameras are utilized, which are responsible for measuring the capsule's movement, not the

involuntary motion of the GI system. A complete setup is designed to test the capsule and perform the experiments. The results show that Method 2 has an average position error of only 3.5 mm and can compensate for the GI tract's relative movements. Furthermore, environmental parameters such as magnetic interference and the nonhomogeneous structure of the GI tract have little influence on our system compared to the available magnetic localization methods. The experiment showed that Method 2 is suitable for localizing the WCE inside the body.

ACKNOWLEDGEMENTS

Special thanks to my supervisor, Dr. Khan Wahid, for guidance, support, and valuable lessons during my studies. Without his insightful advice and criticism, this thesis could not be completed. I like to thank my lab mates, especially Reza, Ehsan, and Amir, for the opportunity I had to work with them and share their knowledge and experiences. Thanks to the University of Saskatchewan for awarding me a scholarship. Many thanks to New Frontiers in Research Fund Exploration (NFRFE) and the Natural Sciences and Engineering Research Council of Canada (NSERC) for providing me with the financial means to complete this project. Finally, I would like to express my sincere thanks to my parents and sibling for their support and inspiration.

TABLE OF CONTENTS

LIST OF FIGURES

LIST OF TABLES

LIST OF ABBREVIATIONS

µC	Microcontroller
AI	Artificial intelligence
ASIC	Application specific integrated circuit
CCD	Charge-coupled device
CE	Capsule endoscopy
CNN	Convolutional neural network
CSV	Comma-separated values
CT	Computerized tomography
DOA	Directional of arrival
DSP	Digital signal processing
FPGA	Field programmable gate array
GI	Gastrointestinal
I2C	Inter-integrated circuit
IC	Integrated circuit
IMU	Inertial measurement unit
LED	Light emitting diodes
LM	Levenberg–Marquardt
LSTM	Long short-term memory
MISO	Master input slave output
MLP	Multi-layer Perceptron
MOSI	Master output slave input
MRI	Magnetic resonance imaging

PC	Personal computer
PCA	Principal component analysis
PCB	Printed circuit board
PSO	Particle swarm optimization
RCNNs	Recurrent convolutional neural networks
RF	Radio frequency
RFID	Radio frequency identification
RSS	Received signal strength
RSSI	Received signal strength index
SCK	Serial clock
SCL	Serial clock
SDA	Serial data
SPI	Serial peripheral interface
SVM	Support vector machine
TOA	Time of arrival
TX/RX	Transmitter/receiver
UART	Asynchronous receiver-transmitter
UI	User interface
USB	Universal serial bus
WCE	Wireless capsule endoscopy

Chapter 1

Introduction

1.1 Overview of Wireless capsule endoscopy

Gastrointestinal (GI) diseases constitute about 8 million deaths worldwide [1]. Several severe disorders, such as obscure GI bleeding [2], [3], ulcer infection [4], celiac disease [5], Crohn's disease [6], Barrett's esophagus [7], tumors, and cancer occur [8] in different regions of the GI tract without any symptoms [9]. Hence, the elderly population aged over 50 years old [10] is recommended to be examined by gastroenterologists regularly. Conventional endoscopy (CE) [11] approaches, such as colonoscopy and gastroscopy, are powerful tools for routine GI checkups. CE is used to visually examine the digestive system with a tiny camera attached to the end of a long, flexible tube. In gastroscopy, the CE probe enters from oral, as shown in Figure 1.1(a), and effectively and reliably visualizes the esophagus, stomach, and duodenum. Meanwhile, in colonoscopy, the probe enters from the rectum and operates inside the colon. A specialist in gastroenterologists uses the CE to diagnose and, sometimes, treat digestive diseases. The CE probe is illustrated in Figure 1.1(b), which is invasive and may cause discomfort for patients [12]. Endoscopy is a very safe procedure; however, rare complications, such as bleeding, infection, tearing of the gastrointestinal tract, etc., might happen [13]. The commonly used CE enable diagnosis inside the esophagus, stomach, and duodenum [14]. However, the small bowel remains unseen [15]. The pains and problems with sedation caused by the conventional endoscope make patients quite reluctant to undergo the endoscopy.

(a) (b)

Figure 1.1 a) Human GI system[1], b) conventional endoscopy probe

[1] https://www.jiahui.com/en/healthLibrary/153

Wireless capsule endoscopy (WCE) [16][17][18][19][20] has had a significant impact on the field of endoscopy. WCE is a powerful tool for monitoring the human GI tract in a single step, and it can significantly reduce the patient's discomfort level [21]. Before introducing the WCE, examining the small intestine was impossible for gastroenterologists without performing a surgical operation. Soon this technology became a golden standard for diagnosing the GI tract [22]. A camera, transceiver unit, and a battery to support the device for 8 hours of operation are integrated into a pill-size electronic capsule. The capsule passes through the GI tract by peristalsis motion, shown in Figure 1.2(a). While traveling through the GI tract, the capsule takes images and sends information to a data logger unit attached to the patient's body wirelessly. The data logger records images and can transfer them to a personal computer (PC). Later, a doctor will review these images to diagnose the diseases. Patients are free to perform their daily tasks throughout the WCE process. Figure 1.2(b) depicts a sample image taken by WCE from the small bowel. Image processing algorithms are developed to assist doctors in examining the WCE images. Artificial intelligence (AI) can detect bleeding [23], polyps [24][25], tumors [26], and several other abnormalities [27] from the visual and texture properties of the images.

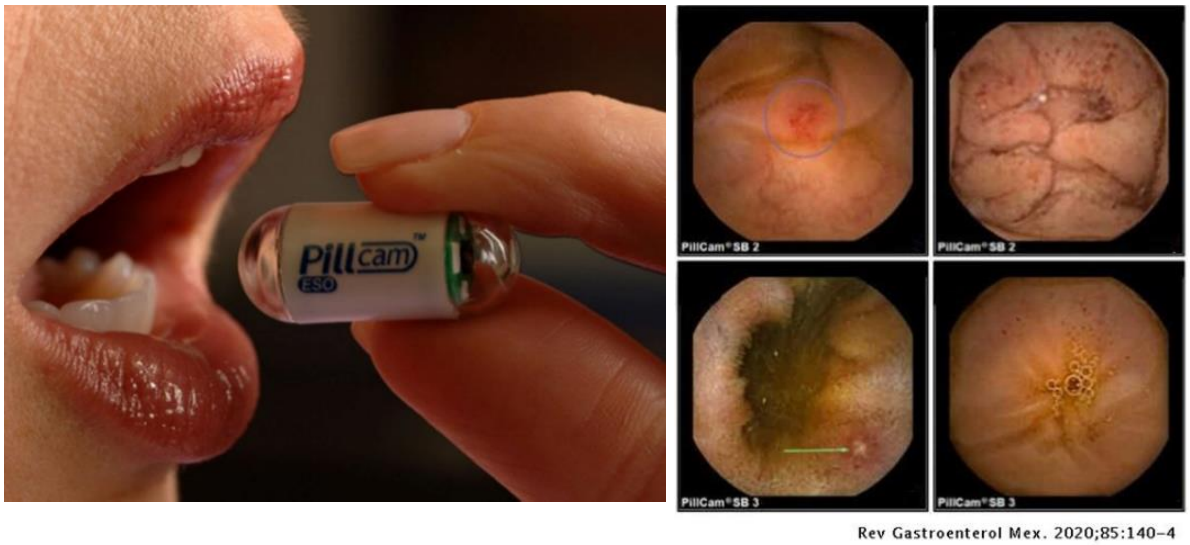

(a) (b)

Figure 1.2 a) WCE[2] a device, d) images were taken by the WCE device

[2] MAYO foundation for medical education and research

1.2 Motivation

The key focus of this research is to propose a novel method to localize the capsule inside the GI tract. Providing position information and tagging the frames by location is a great advantage. The abnormality's location helps doctors determine a suitable treatment plan [28]. It is required at the time of surgery [29]. It is crucial to map the images into the GI tract so that doctors can track the abnormality's progress. Furthermore, capsules can be designed to deliver drugs [30] and release them on abnormality spots [31], [32]. The current WCE devices only provide images of the GI tract, and frames do not provide location information. Several research groups have focused on tracking the position and attitude of the WCE [33]–[37]. Several approaches have been proposed, including image processing, radio frequency, magnetic, ultrasound, medical and radiological imaging, etc. The mentioned methods do not consider the GI motion inside the body coordinate [38]. The GI relative motions cause positioning errors. Available localization methods need a bulky sensor array around the patient's body to capture the data from the capsule. For magnetic and RF-based localization, the sensor array (antenna) acts as a stationary reference point to measure the relative distance between the capsule and the antenna. In this research, a novel method for WCE localization is proposed to distinguish between the capsule's motion and relative motions of the GI tract. A complete prototype of the WCE device consisting of the electronic capsule, sensor belt, and workstation software is developed and tested on a pig intestine.

1.3 Thesis objectives

Several WCE localization methods have been proposed, some of which provide the precise location of the capsule during the WCE process but sacrifice the patients' convenience or require a particular facility and care during the process. On top of that, most of them reduce the positioning error when dealing with the GI involuntary and relative motion. This research aims to develop a localization algorithm to reduce the positioning error caused by GI relative motions. We have developed a prototype WCE system and validated the proposed method's performance with real-world experiments. Considering the challenges faced by WCE localization, the following objectives are investigated for this research.

- To develop a method for localizing the WCE inside the body.
- To develop a robust method, i.e., less affected by the involuntary and relative motions of the GI tract.
- To develop a complete WCE localization system consisting of an electronic capsule, a data logger, or a sensor belt.
- To develop a workstation software that can capture the data, conduct localization algorithms, and visualize the 3D tracking results for the user.
- To validate the localization method for measuring various motions that a capsule experiences inside the GI tract.
- To investigate the performance of the proposed localization algorithm in various scenarios.

1.4 Thesis organization

This thesis is structured into seven chapters. A brief description of each chapter is presented below.

Chapter 1: *Introduction* provides an overview of the endoscopy system, the motivation of the thesis, thesis organization, and research contribution.

Chapter 2: *Research background* presents the literature review of WCE localization methods.

Chapter 3: *Localization using IMU and side wall camera (Method 1)* proposes a novel method for localizing a capsule inside the GI tract. This method uses an IMU sensor and a side wall camera to distinguish the capsule's motion from the GI tract's relative motion. The capsule prototype and the experimental setup are discussed in this chapter.

Chapter 4: *Results and discussion for Method 1* presents the results of experiments to evaluate the performance of the localization Method 1.

Chapter 5: *Localization using magnet sensor and side wall camera – MagnetOFuse (Method 2)* proposes the second localization method to resolve the drifting issue of Method 1 while keeping the same positioning error. The capsule prototype, workstation software, and experimental setup are discussed in this chapter.

Chapter 6: *Results and discussion for Method 2* presents the results of experiments to evaluate the performance of the localization Method 2.

Chapter 7: *Summary and conclusion* provides a summary of this research and a list of publications generated from this research.

1.5 Research contribution

In this research, two localization methods for WCE are proposed. This research focuses on distinguishing the capsule's motion from the relative motion of the GI tract. This achieves by considering the unique properties of the GI system. At the time of writing this thesis, the commercial capsules [39]–[41] do not support localization. Only a rough estimation of the capsule trajectory is possible using RF localization.

The first method uses an IMU sensor to measure the capsule heading vector and a side wall camera to capture the relative displacement. Then, a fusion algorithm combines the data to estimate the traveled trajectory. This method eliminates the need for a fixed, stationary sensor belt wrapped around the patient's body. The contributions of Method 1 are: making use of an IMU sensor to calculate the heading vector, a tiny monochromic camera to measure the displacement in the GI lumen, and a fusion algorithm to combine all information and calculate the 3D traveled trajectory.

Method 2 was developed based on magnetic localization and side wall camera fusion. This method requires a sensor belt attached to the patient's body. The proposed fusion method is robust to positioning errors caused by the relative motion of the capsule. A complete prototype of the WCE system is designed and implemented. This includes an electronic capsule with sensors, a datalogger or sensor belt to receive the information from the capsule, and workstation software to visualize the incoming data. The developed datalogger is portable and can be powered up using a power bank. Patients carry the datalogger throughout the process. The data logger has two options, either log the data in its internal memory or connect to a PC for real-time data transfer using a USB interface. The workstation software is connected to the datalogger to read and plot the information online on a screen. In addition, it can record the data and perform localization algorithms offline. Then, the workstation software plots a 3D track to show the estimated trajectory of the capsule. Finally, ex-vivo experiments of the localization methods have been performed using a pig's intestine, and several capsule motions have been captured to validate its performance.

A list of publications which are generated from this research during the program is presented in Appendix A.

Chapter 2

Research background

Given Imaging introduced the first commercial WCE in 2000 [41] and named it PillCam. Several WCEs are now available in the market, such as PillCam Crohn's, PillCam SB2, and SB3. Other companies also commercialized their product, including Microcam and Olympus. However, they do not support precise localization. Several techniques have been developed for WCE localization, including image processing, radio frequency, magnetic, ultrasound, medical and radiological imaging, etc. In this section, a review of available methods, along with their advantages and limitations, is provided.

2.1 Image-based localization

Localization based on image processing techniques has been studied by several researchers [42]–[44]. WCE sends the raw frames to a datalogger outside of the body. Hence, utilizing these frames to estimate the capsule's position would be a suitable method, as it does not require any extra equipment. A study by Turan *et al.*[45] have proposed a monocular visual odometry for capsule tracking. Their approach uses convolutional neural networks (CNNs) for feature extraction and recurrent neural networks (RNNs). The proposed deep learning network consists of three inception layers and two Long short-term memory (LSTM) layers concatenated sequentially. The inception layers imitate human beings' visual cortex and extract multi-level features. The last inception layer passes the feature representation into the RNN network. RNNs are suitable for modeling the dependencies of image sequences and creating a temporal motion model because they have a memory of hidden states over time. The current hidden state is a function of an arbitrary series of inputs. Due to the lack of sufficient annotated datasets, they have trained the system in an end-to-end manner; hence, the network parameters do not need to be fine-tuned. The method is analyzed and evaluated on a real pig stomach dataset. Their results showed a 3% positioning error in a 1 m long trajectory. Koulaouzidis *et al.*[46] implemented generic visual odometry. Their proposed algorithm uses geometric features of each frame; hence, it does not require any prior information to tune its intrinsic parameters, and it can perform on various frameworks. Furthermore, they exploited color information to increase positioning accuracy. As shown in Figure 2.1, they have prepared an experimental test setup that includes a robotic arm, a bowel model, and a CE device.

The CE is attached to a robotic arm that moves the capsule in a predefined trajectory inside the bowel. They added color features to the bowel, as shown in Figure 2.1 (d). Hence, the capsule can analyze these features during its travel inside the bowel and reconstruct the cylindrical shape of the test experiment with details. They reported a mean absolute error of 4.1 ± 3.9cm.

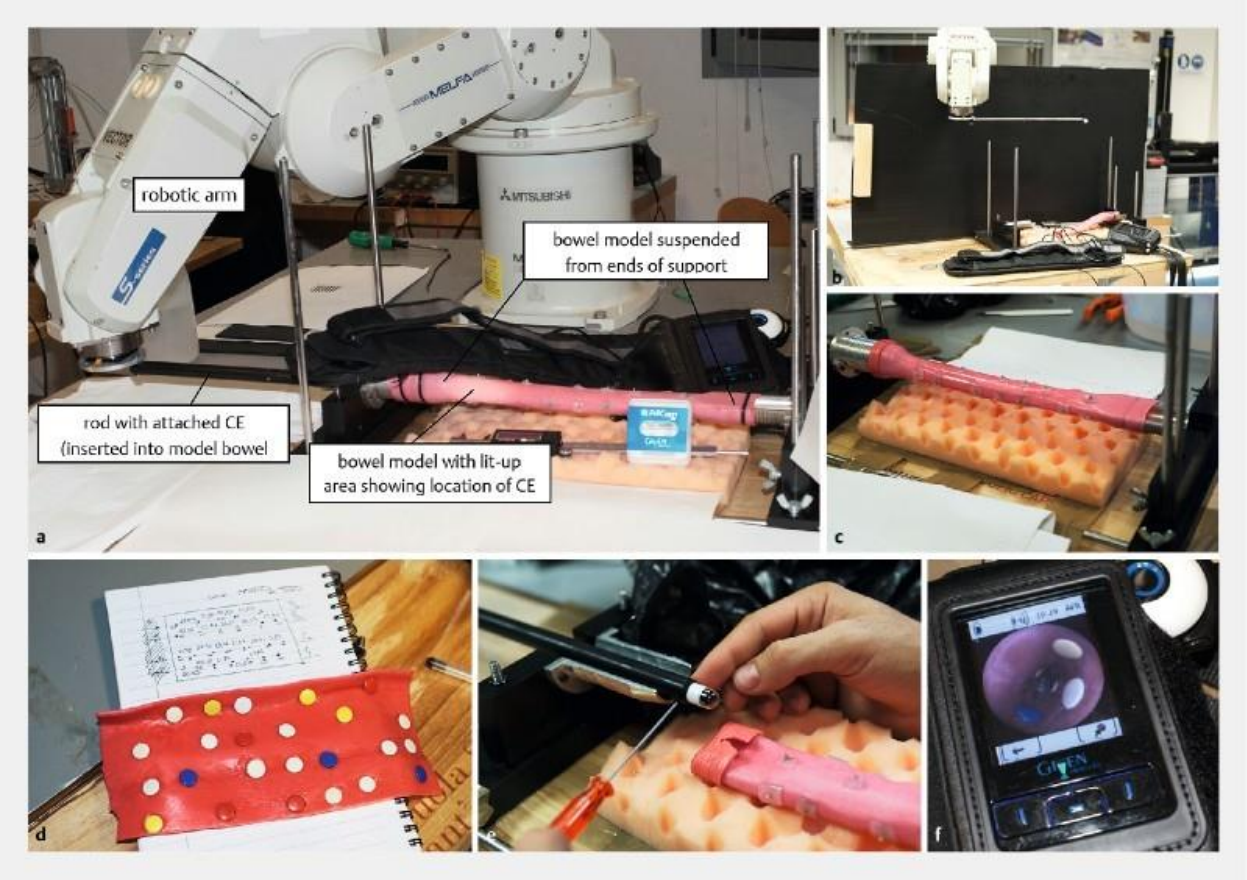

Figure 2.1 a) Overview of experimental test setup for [46]. b) Setup view. c) Detail of assembled bowel model. d) Opened experimental bowel, showing simulated color features. e) capsule endoscopy fixed to the end of a straight plastic rod to enable movement through the model bowel lumen. f) Real-time CE viewer datalogger.

Mackiewicz *et al.* [47] developed a feature vector that incorporates color, texture, and motion information of frames. They utilized multivariate Gaussian classifiers implemented within the framework of a hidden Markov model. Finally, they used color image analysis to automatically discriminate between the esophagus, stomach, small intestine, and colon tissue. Cunha *et al.* [48] utilized a combination of texture and color features with a support vector machine (SVM) for localization. Similarly, they used the median error for the esophagogastric junction, pylorus, and ileocecal valve. They reported 2, 287, and 1057 median frame errors, respectively. Vu *et al.*[49] utilized color features, principal component analysis (PCA), and a customized thresholding

approach for localization. The median error was used for the pylorus and ileocecal valve as a metric defined on the frame difference unit and achieved 105 and 319 median frame error, respectively. Marques *et al.*[50] made use of color features and SVM for the pylorus and ileocecal valve localization. They reported an overall accuracy of 85.2%. Shen *et al.* [51] used the scale-invariant feature transform for extracting local image features. The probabilistic latent semantic analysis model is used to localize the capsule in the esophagogastric junction, pylorus, and ileocecal valve. They reported 99.9%, 98.3%, and 94.7% accuracy, respectively. Bao *et al.* [52] extracted color intensity, motion, and texture features and used a kernel SVM to locate the pylorus and ileocecal valve. This method can map the low-dimensional feature vectors to a higher dimensional space in order to form a non-linear decision hyper-plane. Their results showed that the proposed method could achieve an accuracy of 92%. Bao *et al.*[53] tried to localize the capsule with the aim of speed estimation in video frames. The algorithm is tested under several capsule motion speeds, as shown in Table 2.1. The results showed that the average estimation error is 0.022 mm/s and 0.298 mm/s, while the capsule speed is 1 mm/s and 4 mm/s, respectively. They analyzed consecutive frames to calculate the spatial displacement and achieved an average of 93% accuracy for speed estimation and 2.49 cm error as localization error.

Table 2.1 Average estimation error in video frames

Average speed (mm/s)	**Number of detected feature points**	**Average estimation error (mm/s)**
1	79	0.022
…	…	…
4	32	0.298
10	NA	NA

Dimas *et al.*[54] proposed a novel visual odometry approach based on multi-layer perceptron (MLP), which is applied to SIFT features. They estimated the WCE location according to anatomic landmarks and reported an error of 2.70 ± 1.62 cm. The accuracy of an image processing-based algorithm is proportional to the image quality and framerate; meanwhile, the WCE has the low image quality and can take two to four frames per second. Above all, localization approaches based solely on visual information suffer from the accumulation of errors and deviation from the ground truth, as these methods have no recalibration or feedback process.

2.2 RF-based localization

The WCE takes pictures and sends them by RF signals. As all necessary equipment for RF-based localization methods has already been installed in the capsule, this method became the primary research interest of scientists. Techniques such as Time of arrival (TOA), Direction of arrival (DoA), Received signal strength indicator (RSSI), Radio frequency identification (RFID)-based methods, and hybrid forms are investigated. Nafchi *et al.* [55] introduced an RF-based WCE localization method to track the capsule. They utilized an arrangement of the circular antenna array for receiving the RF signals. Then, with the aim of a Kalman filter, they filtered out all fluctuation in the received signal. Their proposed method has a positioning error of up to 10 mm. Figure 2.2 shows an antenna array wrapped around the patient's body to receive signals from WCE and perform localization.

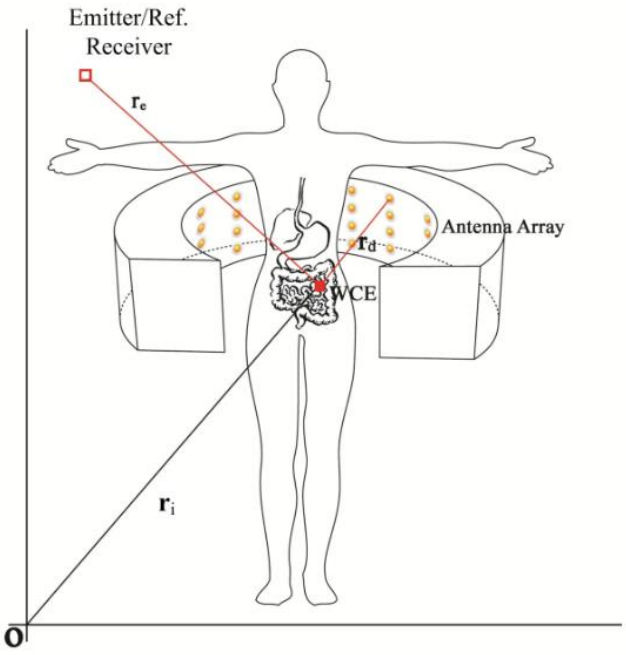

Figure 2.2 An antenna array wrapped around the patient's body to receive signals from WCE and perform localization [55]

In [56], authors proposed a method to estimate the location and orientation of an electronic capsule based on the DOA method by exploiting the Unscented Kalman filter. Hekimian-Williams *et al.* [57] analyzed signals reflecting from an RFID tag by software-defined radio. They successfully estimated the capsule's orientation with a positioning error of up to 0.02°–0.12°. Yi *et al.* [58] have developed an RFID reader consist of a 4×4 sensors array to detect the WCE signals

inside the stomach with a positioning error of about 65 mm. Chandra *et al.*[59] proposed a localization method based on the phase difference method. The proposed technique consists of an antenna array with *N* elements attached to the patient's waist that can capture the received signal from the WCE inside the body. By analyzing the received signal information, the 2D and 3D localizations of the capsule can be determined. They have reported a positioning error of around 5.4 mm. In studies [60]–[63], RSSI measurement and TOA are considered for WCE localization. A study by Khan *et al.*[64] have used a 3D human body representation model for TOA propagation and investigated the localization method based on TOA and Received Signal Strength (RSS) in three different GI organs to determine an optimum number of sensors and their arrangement. They achieved a mean positioning error of 50 mm. Xu and his team [65] adopted a multi-source fusion approach to estimate the capsule location. They have integrated TOA data with an Inertial measurement unit (IMU) sensor, using a Kalman filter and Chebyshev center-based optimization method. The distance information derived from the TOA algorithm and elliptical data from the IMU sensor concurrently feed to a fusion algorithm and efficiently improve localization accuracy and decrease drift error. Studies indicate that RF-based localization approaches for WCE are possible. However, higher positioning errors hindered its further progress. The RSSI-based localization methods depend on the frequency. At higher frequencies, the tracking process suffers from signal scattering and attenuation due to the loss in the human body's non-homogenous structure, such as tissues, muscles, blood, and bones.

2.3 Magnetic-based localization

Magnetic localization is considered a promising option for WCE localization [66] and has been investigated by several researchers till now [67]–[77]. Magnetic localization is known as a promising option for future ingestible capsule localization [66], [78]–[83]. Unlike RF signals, magnetic fields do not scatter by the unstructured environment of the GI. Researchers have developed tracking methods based on magnetic fields. They integrate a permanent magnet inside the capsule, and magnetic fields are measured by an array of magnetic sensors around the body. Then, an optimization algorithm is used to estimate the capsule location. Song and his team [84] have developed a magnetic localization based on differential signals. They used an array of 16 sensors (HMC5883L), each separated by 4 cm distance in a planar sheet. As the sensors are near each other, the geomagnetic field can be considered the same. It uses Levenberg–Marquardt (LM) [85] algorithm to estimate the magnet location. This method achieved an average positioning error

of 5.2 mm and a mean orientation error of 6.6°. A similar work by Zeising *et al.* [86] was performed by placing the magnetic sensors on the surfaces of a box and achieved a better tracking result. Then, they utilized the same differential signal method to compute the magnet location. Their results showed positioning and orientation errors of 4 mm and 2°, respectively. However, the rigid sensor array box will limit the patient's activities. Moreover, the relative displacement of the box and the patient's body could increase positioning error. Boroujeni *et al.*[87] utilized a new magnetic localization by considering the dynamic equations of the capsule's motion. They proposed a fusion method to combine this information using a Kalman filter. In addition, the fusion algorithm could estimate the position if the magnetic data are interrupted during localization. Their magnetic sensor array for experimental setup consists of 16 sensors. Their method achieved a positioning error of 1 mm. Shao *et al*. [88] proposed a method to reduce the drifting effect by introducing simultaneous geo-noise cancellation and adding two sensors on the patient's chest. Their proposed method obtained the initial position guess through the variance-based algorithm. Their proposed method achieved higher localization accuracy. Shao reported a positioning error of less than 10 mm and an average orientation error of 12°. They also investigated the effect of bio-tissue on the magnetic field. It showed that the non-ferromagnetic bio-tissues have a minor impact on the magnetic fields, so human tissues will not influence positioning accuracy. Figure 2.3 shows the experimental setup they have prepared. Figure 2.3 (a) & (b) demonstrate the sensor array, which has four magnetic sensors on each face. Figure 2.3 (b) & (c) show a patient put on the sensor belt while an extra magnetic sensor is attached to its chest. This sensor measures the base magnetic flux of the environment, resulting from the earth's magnetic field and other ferromagnetic material around the patient. Then, this value will be considered as a base offset for the method to compensate for the errors. Xu *et al.*[68] proposed an adaptive simultaneous magnetic actuation and localization for WCE by considering the tubular environment of the GI tract. Their algorithm automatically selects and activates an optimal subset of magnetic sensors during capsule movements. An improved multiple objects tracking [89] algorithm is used to estimate the position and orientation of the capsule in real time. They reported an average position error and orientation estimation of 4.3 mm and 5.4˚, respectively.

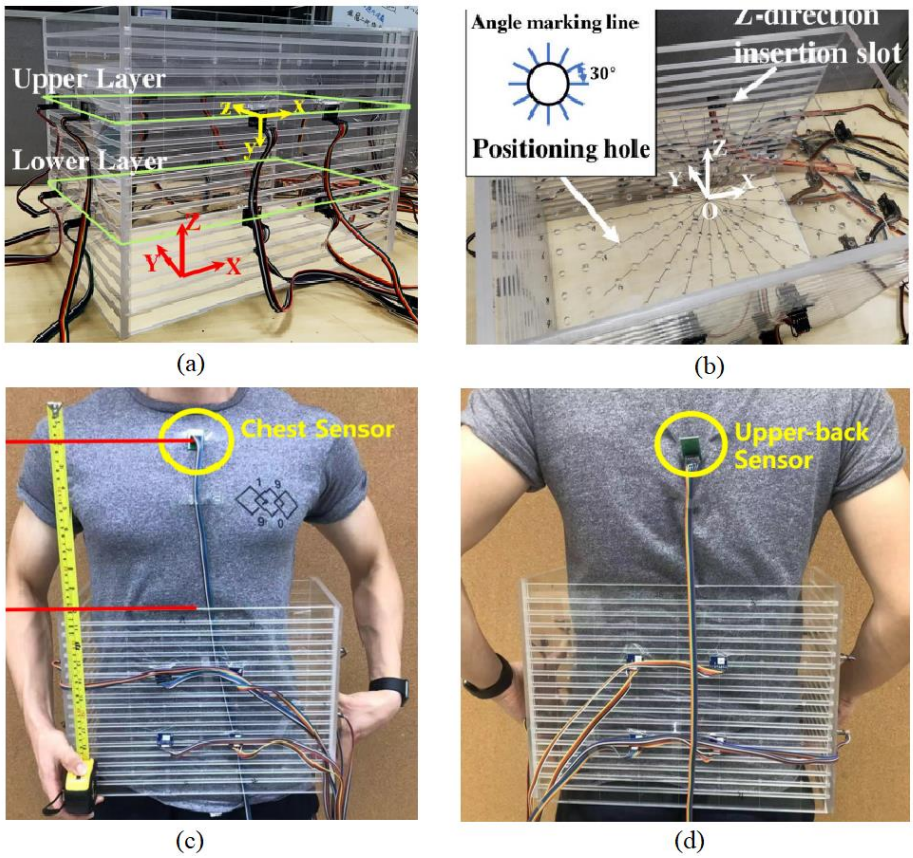

Figure 2.3 Magnetic-based localization experimental setup of [88].

Apart from the advantages of magnetic localization methods, they cannot distinguish between the WCE movements and the relative motion of GI inside the body. This affects localization accuracy and introduces errors.

2.4 Other and hybrid localization methods

Other methods such as Magnetic resonance imaging (MRI) [90], Computerized tomography (CT), ultrasound [91], X-ray [92], and gamma-ray techniques [93] or hybrid methods are investigated for WCE tracking. Although radiation-based methods such as MRI and X-ray offer a high level of accuracy, it is not feasible to perform those methods for long periods due to the risk of radiation exposure. Kalantar-Zadeh and his team [94] integrated oxygen, hydrogen, and carbon dioxide gas sensors into an electronic capsule to measure the GI gas concentration profile. Their results showed that oxygen concentration is at the highest in the stomach, then decreases as the capsule enters Jejunum and Ileum. Finally, the oxygen concentration is almost zero in the colon. Meanwhile, carbon dioxide percentage remains the same in the stomach, then increases in the small bowel. As stated above, the gas content of the GI system could be a potential parameter for localizing the

capsule. Figure 2.4 shows Gas profiles and their association with the capsule location.

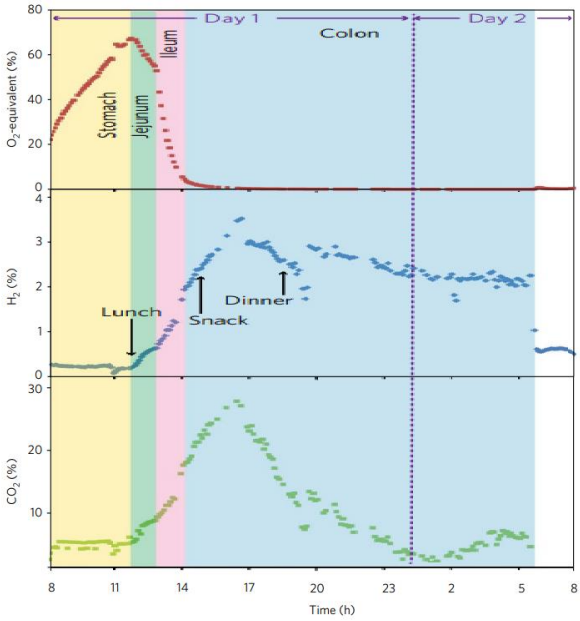

Figure 2.4 Gas profiles and their association with the capsule location [94]

A research team [95] mounted an array of capacitive pressure sensors on the capsule's semi-spherical head. The GI peristalsis motion induces pressure on the capsule. They analyzed this information and estimated the latitude and longitude of the capsule.

The GI involuntary motion is non-predictable, and it leads to inaccurate localization. It is impossible to compensate for these motions with classical mathematics methods. GI relative motion can be modeled as a two-nested coordinate system in which one might freely move against the other. The first system is the array antenna surrounding the body, and the second is the small bowel. The small bowel may move according to an external coordinates system, while the GI organ may move or rotate within the body coordinates in a different direction. Hence, most localization techniques are not able to detect relative motion.

Chapter 3

Localization using IMU and side wall camera (Method 1)

3.1 Introduction

The Human GI tract is a tubular pathway. Using this feature, we have developed a method for WCE localization. The primary focus of the proposed method is to localize the capsule inside the intestine, as CE could not reach out to this section of the GI system. We started this section with an example to shed some light on the method. A train is traveling in a tunnel, and a passenger inside the wagon has a compass and is looking toward the tunnel's wall. The compass gives the wagon's heading direction and points toward the direction of travel. In addition, that person, by looking toward the tunnel's wall, knows how far it has traveled. Similarly, we have proposed a system composed of an IMU sensor, side wall cameras, a processing unit, and a transceiver unit. The device's orientation comes from an IMU sensor, and side wall cameras measure the capsule's displacement. On top of that, a fusion algorithm is introduced to combine the orientation data and the displacement. Finally, the system can plot a traveled trajectory in a 3D space.

3.2 Materials and methods

3.2.1 Displacement measurement using Side wall camera

Odometry originated from the Greek words "hodos metron*,"* which means measure travel. Visual odometry is a technology that measures displacement and orientation using a stream of images. The images contain enough meaningful information, such as color, texture, shape, etc., to estimate the movement of the scene. In principle, a camera captures images. Then the processing unit analyses them to measure optical flow and performs odometry algorithms to measure the displacements. However, image processing is typically computationally expensive, and it involves several steps, including 1) images acquisition, 2) feature extraction (edges, corners, lines, etc.), 3) frame matching to highlight the changes between adjacent frames, 4) position calculation by measuring the pixel displacement between frames. Figure 3.1 illustrates the working principle of visual odometry for WCE localization. Four cameras are placed at the side of the capsule, and they look toward the GI wall and take images. Then, the image processing unit conducts the displacement measurement algorithms. The GI tract is tubular, and peristalsis motions squeeze the

capsule. So, at least one side of the capsule touches the GI wall. Image processing-based algorithms are susceptible to environmental conditions, such as lightning, illumination changes, textures, image blurriness, presence of shadows [96]. A camera takes pictures, and an image processing algorithm calculates the displacement. The image processing can be performed outside or inside the capsule. Adding four cameras on the capsule's side and sending frames require huge power resources and transmission bandwidth. The second approach is to utilize an ASIC, which integrates a low-resolution camera and image processing unit inside the IC. Figure 3.1 shows the working principles of the motion estimation algorithm. h is the fixed distance between the camera and the intestine's wall θ is the angular position of each pixel, and $\vec{D}$ is a vector that shows the displacement of individual pixels compared to the previous frame. The displacement comes from four cameras located at the capsule's side wall. As a rule of thumb, at least one camera should stick to the intestine's wall. The camera takes pictures every 10 ms. Then, images are compared, and distinct points at each frame will be selected. Then, the algorithm looks for the same point at adjacent frames. The algorithm can calculate motion vectors for individual pixels ($\vec{D}_1, \vec{D}_2, \ldots$). Finally, it computes the average vector and finds the average displacement vector ($\vec{D}_m$).

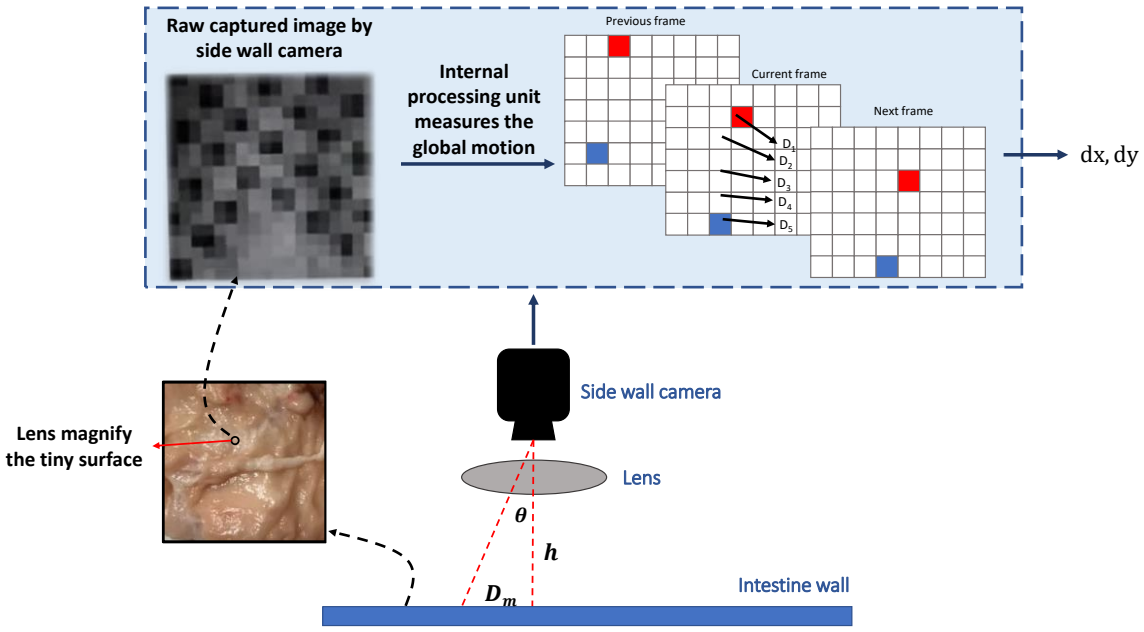

Figure 3.1. The side wall camera is placed toward the intestine wall and takes images. Then, it compares consequence frames and measures the displacement.

3.2.2 Inertial measurement unit

An Inertial measurement unit, commonly known as an IMU, is an electronic device that measures and reports gravitational forces, angular velocity, and magnetic forces using accelerometers, gyroscopes, and magnetometers. The gyroscope measures angular velocity. In other words, the gyroscope reports how fast the device spins about an axis. Rotation about different axes is illustrated in Figure 3.2, which is named roll, pitch, and yaw.

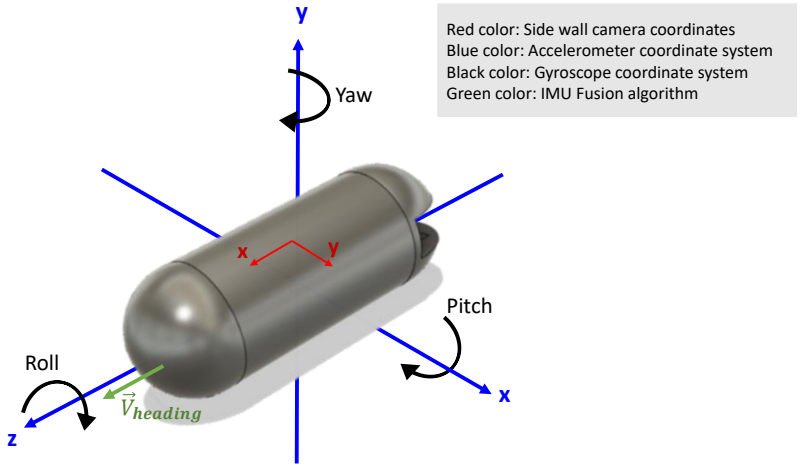

Figure 3.2. Rotation about different axes of the capsule.

The gyroscope gives the rate of change of the angular position over time with a unit of $\left(\frac{\text{deg}}{\text{rees}}\right)$, according to equation 3.1 [99].

$$\dot{\theta} = \frac{d\theta}{dt} \qquad (3.1)$$

We integrate the angular velocity over time to derive the angular position. It can be mathematically shown as equation 3.2.

$$the\ \theta(t) = \int_0^t \dot{\theta}(t)\, dt \approx \sum_0^t \dot{\theta}(t) T_s \qquad (3.2)$$

where T_s is the sampling time and represents the time interval between samples. The gyroscope data is reliable only in the short term and is susceptible to drift. Hence, accelerometer data is used to compensate for the gyroscope data.

The accelerometer measures all forces that are working on the object and sends them as A_x, A_y, and A_z. To obtain the angular position with the accelerometer, we will determine the position of the earth's gravity vector, which is always visible on the accelerometer. This can be done by

using an atan function. In addition, the yaw is derived from a magnetometer, so a fusing algorithm is required to combine the sensors altogether.

The IMU sensor and side wall cameras have different coordinate systems. The IMU's z-axis is placed along the front and back of the capsule, as depicted in Figure 3.2. The heading vector ($\vec{V}_{heading}$) shows the capsule's motion direction (IMU's z-axis) in a 3D space. $\vec{V}_{heading}$ is defined based on the earth's gravity and north magnetic pole.

The IMU sensor must be calibrated before use to compensate for the surrounding conditions and noises. The magnetometer should only perceive the earth's magnetic field to measure a correct orientation. The magnetic measurements will be subjected to two types of distortion - hard iron and soft iron distortions. Objects that produce a magnetic field cause hard iron distortion, which is a permanent bias in magnetometer output. Soft iron distortion, on the other hand, is caused by ferromagnetic objects and leads to deflections or alterations in the existing magnetic field. Bias terms are added to the raw data to cancel the hard iron effect. Meanwhile, correction factors in matrix format will neutralize the soft iron distortion according to equation 3.3 [100].

$$\begin{bmatrix} M_{xc} \\ M_{yc} \\ M_{zc} \end{bmatrix} = \begin{bmatrix} S_{11} & S_{12} & S_{13} \\ S_{21} & S_{22} & S_{23} \\ S_{31} & S_{32} & S_{33} \end{bmatrix} \times \begin{bmatrix} M_x \\ M_y \\ M_z \end{bmatrix} + \begin{bmatrix} B_x \\ B_y \\ B_z \end{bmatrix} \qquad (3.3)$$

where $M_{x,}$ M_y, and M_z are magnetic fields. M_{xc}, M_{yc} and M_{zc} are calibrated magnetic fields. B_x, B_y and B_z are the applied biases to compensate for the hard iron effect, and S_{mn} are correction factors to remove the soft iron distortion.

3.2.3 Compute the heading vector

Information captured by the accelerometer, gyroscope, and magnetometer will be fused using the Attitude heading reference system (AHRS) algorithm [101] to measure the 3D orientation of the capsule. This algorithm creates a model based on the IMU sensor's data, then it estimates the earth's gravity and measures the capsule's orientation with respect to the gravity vector. It uses a Kalman filter to update the orientation and remove the noises from the data. Kalman filters have demonstrated their usefulness in various applications. Kalman filtering is an algorithm that provides estimates of some unknown variables given the measurements observed over time and can minimize the variance of the estimation error. Figure 3.3 (a) demonstrates the IMU sensor fusing schematic described by Roetenberg *et al.*[102]. The accelerometer is designed based on MEMS technology and suffers from noises on its output. Hence, a filter is used to cancel the

noises. The Kalman filter is part of the fusion algorithm and fuses the IMU data to find the capsule's orientation. Figure 3.3(b) shows the 3D orientation result. The output provides an accurate orientation estimation.

The next step toward capsule localization is fusing the orientation with displacement data. The capsule's orientation is derived via the IMU fusion algorithm, and the heading vector can be calculated using roll, pitch, and yaw angles according to equation 3.4. The heading vector should be normalized for further processing. By moving along the heading vector, we could compute the location in 3D space [101].

$$\vec{V}_{heading} = (-\cos(\psi)\sin(\varphi)\sin(\theta) - \sin(\psi)\cos(\theta))\hat{X} + (-\sin(\psi)\sin(\varphi)\sin(\theta) + \cos(\psi)\cos(\theta))\hat{Y} + (cos(\varphi)sin(\theta))\hat{Z} \quad (3.4)$$

where ψ is yaw, φ pitch, and θ roll angles. The $\hat{X}, \hat{Y}$,and $\hat{Z}$ are the unit vectors in a cartesian coordinate system.

The side wall camera sensor provides the displacement along the heading vector. The 3D projection of the capsule's movement will be derived from equation 3.5.

$$\vec{D} = D_{\text{mx}}.\vec{V}_{\text{heading}} \quad (3.5)$$

where $\vec{D}$ shows the 3D displacement vector, and D_{mx} is the $\hat{X}$ component of the $\vec{D}_m$. Finally, to get the 3D position, we have used the following equation:

$$P_{t+1}(x, y, z) = P_t(x, y, z) + \vec{D} \quad (3.6)$$

where P_{t+1} is a new position and P_t is the previous position. Thus, we can calculate the new position of the capsule from the last position. Finally, a 3D trajectory is generated.

Since the capsule is confined in a tubular shape track and peristalsis motion pushes the capsule through the cylindric structure, it moves only along $\vec{V}_{\text{heading}}$ (IMU's z-axis, and not along *the x* or *y* direction). The capsule can move either forward or backward (± IMU's z-axis) depending on how it is entered into the small bowel. As shown in Figure 3.2(b), the red vector shows the $\vec{V}_{\text{heading}}$, which points out the direction of the capsule. The algorithm ignores motions that are not along the $\vec{V}_{\text{heading}}$. As a result, intestinal motions inside the body will not interfere with capsule tracking. An overview of the heading vector and fusion algorithm is depicted in Figure 3.2(c).

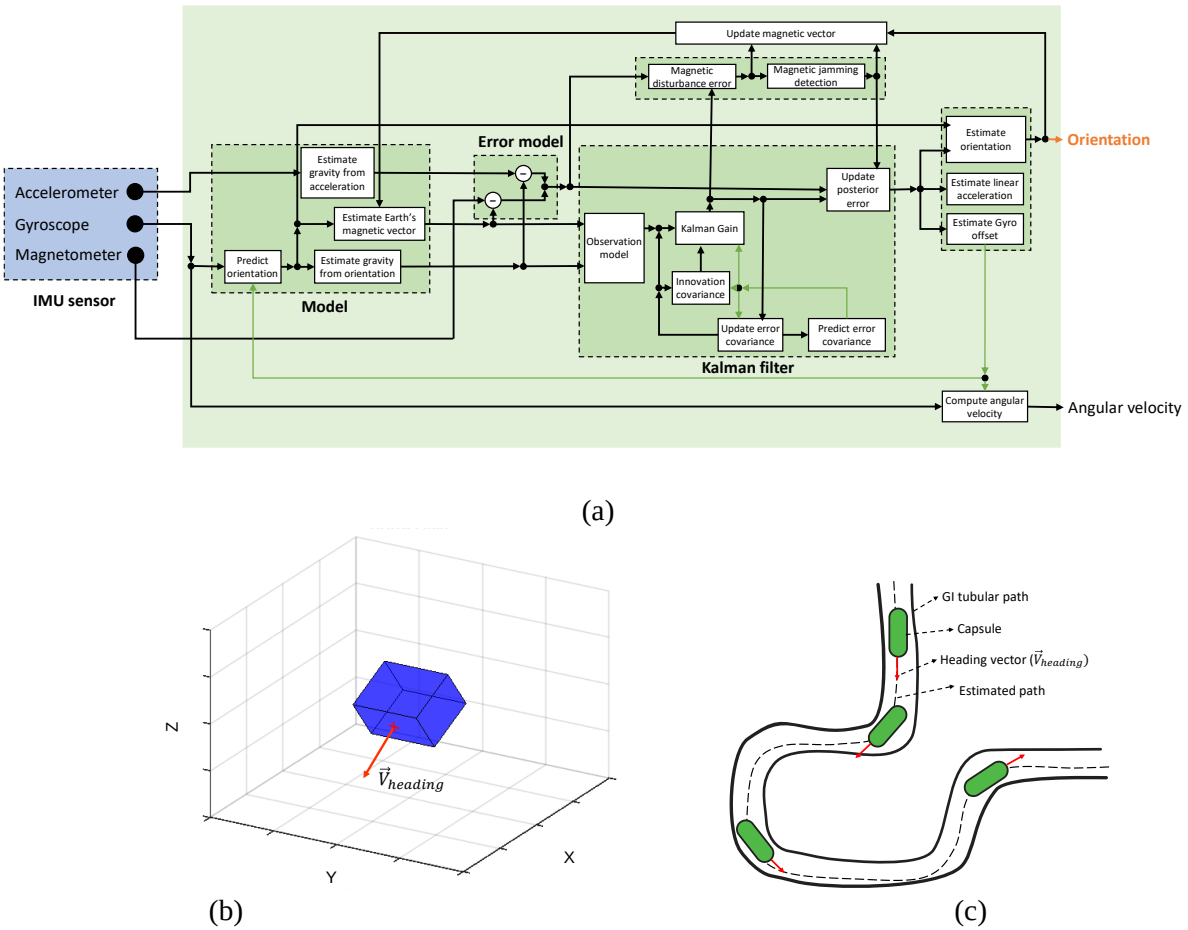

Figure 3.3. (a) AHRS algorithm, which computes the orientation of the capsule using IMU sensor data, (b) 3D orientation result, and (c) overview of the fusion algorithm

3.3 Hardware prototype

The proposed capsule and its necessary components are provided in this section.

3.3.1 Capsule architecture

The block diagram of the capsule is shown in Figure 3.4. The microcontroller unit is a bridge between different parts of the system, and it controls all modules, including the IMU sensor, side wall cameras, and RF transceiver unit. The capsule is equipped with four cameras, one for each side; however, to make it easy for presentation, only two of them are depicted in the schematic. Side wall cameras have an Inter-integrated circuit (I2C) interface and need two pins for their communication. Serial data (SDA) pin is a line for the master and slave to send and receive data. The Serial clock (SCL) pin is used to carry the clock signal. They are shared between all modules. The RF transceiver unit uses UART communication protocol. This interface needs two pins, a TX pin to transmit and RX pin to receive the data. The IMU sensor is connected via a Serial peripheral

interface (SPI) with three pins for communication. The Master output slave input (MOSI) pin sends the data from the microcontroller to the sensor. The Master input slave output (MISO) pin sends the data from the sensor to the microcontroller, and the Serial clock (SCK) pin shares the clock between devices. The capsule captures the data and sends them in a raw format to the data logger outside the body; therefore, it does not require any data processing inside the capsule, significantly reducing the design complexity. After receiving the data, a computer-based program is responsible for applying algorithms and calculating the 3D result. The final prototype is shown in Figure 3.5. The capsule size is 3.5 cm × 3.5 cm × 4 cm.

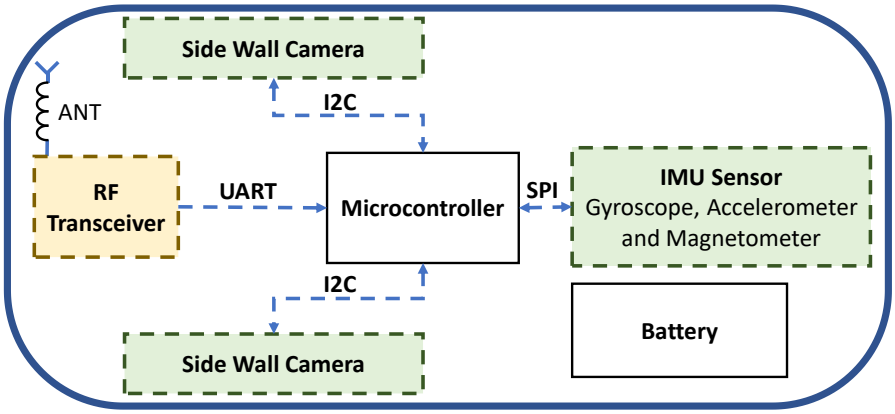

Figure 3.4 Schematic overview of the capsule. The microcontroller unit is connected to the IMU, side wall cameras, and RF transceiver units.

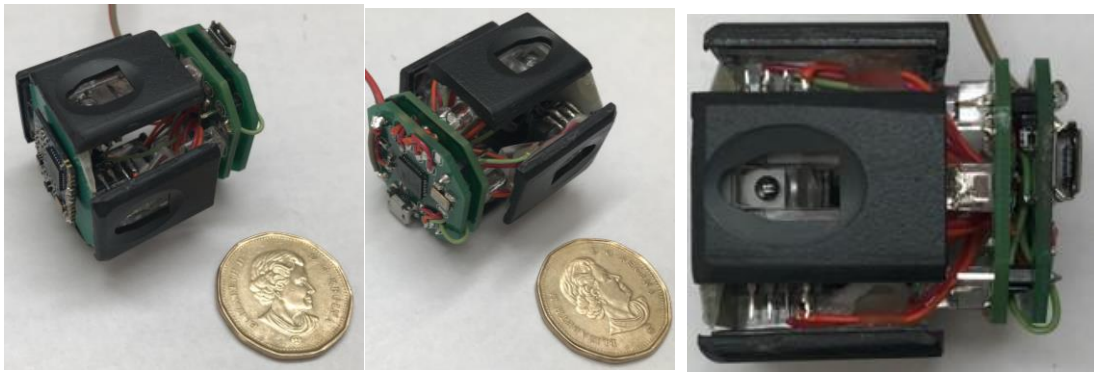

(a) (b) (c)

Figure 3.5 Capsule prototype designed in the lab from different view angles

3.3.2 Microcontroller unit

A microcontroller (µC) is responsible for connecting all components to work as a system. Individual sensors are connected to the µC through specific protocols. For this project, ATmega32U4 is used as a processing unit. This µC has built-in I2C and SPI, making it easier for different applications.

The µC reads all sensors and sends the raw data using a wireless link. The capsule reads 2 Bytes from each side wall camera and 18 Bytes from the IMU sensor. Finally, the µC creates a frame of 28 Bytes with all data and headers, then sends them to a data logger outside the body. The µC only sends the frame when it detects a motion to reduce the transmission power. Figure 3.6 shows the designed PCB for the microcontroller unit.

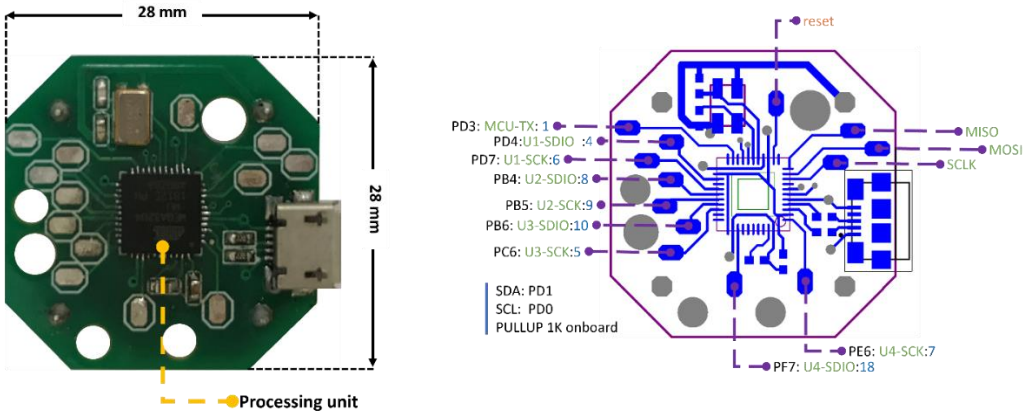

(a) (b)

Figure 3.6 a) PCB layout and its dimension b) pinout for microcontroller unit

3.3.3 Side wall camera

Visual odometry is a technology that measures the displacement using the optical flow of the scene. In principle, a camera captures the pictures and sends the frames out of the body for processing. Then an image processing algorithm calculates the displacement. However, adding four cameras on the capsule's side and sending frames require huge power resources and transmission bandwidth. While processing images inside the capsule adds complexity to the design. A motion measurement camera is an IC with a low-resolution camera with onboard Digital signal processing (DSP) unit to run the image processing algorithms and communication interface, all on a tiny silicon dye. Figure 3.7 illustrates the side wall camera. The actual size of this IC is 1 mm × 2 mm. The light-sensitive part is a Charged coupled device (CCD) camera with an 18×18 pixels sensor

array. A chip with part number YS8008B is selected for the design. This IC works with a 3 V power supply and has an I2C interface protocol.

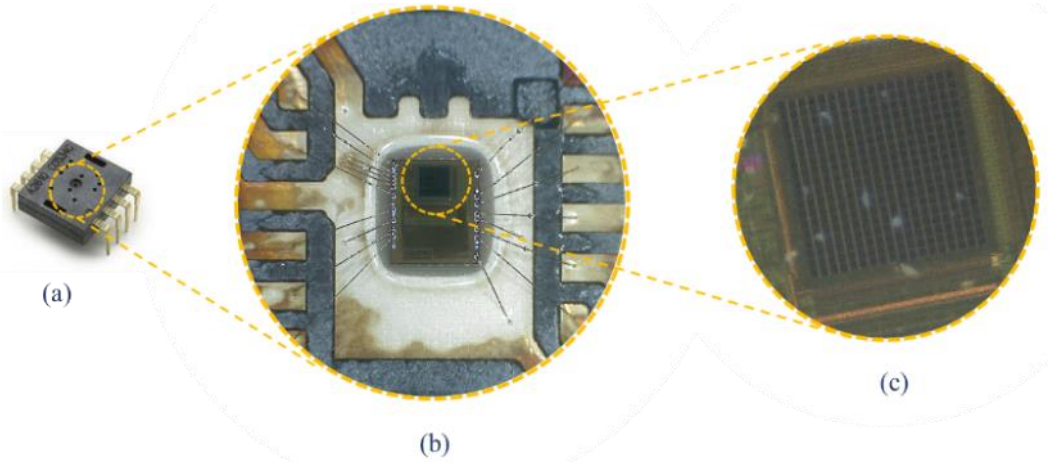

Figure 3.7 Optical motion measurement sensor (similar to the one used in computer optical mouse today), (a) Dual inline package IC, (b) Microscopic view, and (c) 18×18 pixels CMOS camera.

The technology inside the side wall camera is similar to the one used in PC's optical mouse today. It consists of three essential components: motion sensor (monochromatic camera), optical lens, and lighting source. Figure 3.8 illustrates the camera and related optical system. The optical system consists of a prism and a focus lens. The prism guides the light source so that it lights up the camera view then the lens focuses the reflected light from the surface to the CCD. The light guider is positioned to receive the light rays from the right side and guides the beams with a correct angle to be emitted to the surface and reflected precisely to the CCD. In addition, a Light emitting diode (LED) with red color is selected to have the highest reflection rate in the GI tract. A magnifier (lens) is placed between the side wall camera and the surface.

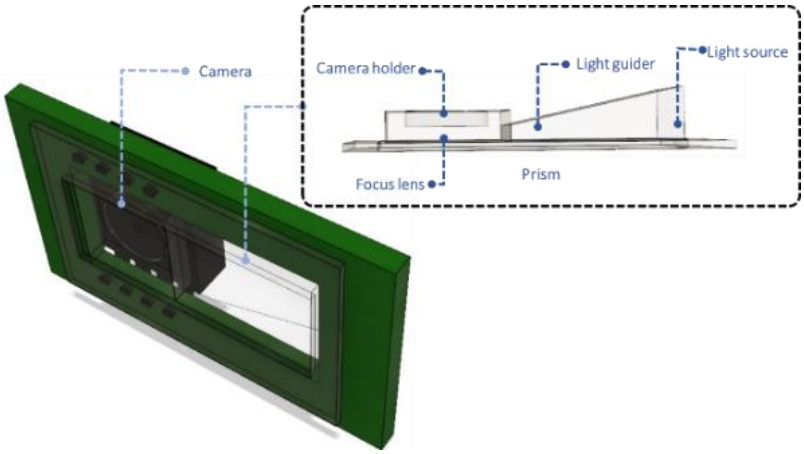

Figure 3.8 Side wall camera and its optical parts, including prism, light guider, and lens

The lens magnifies the surface and makes it possible to see several small markers. The raw image has only 18×18 pixels of a macroscopics' view of the surface. Hence, motion sensing depends on these tiny markers on GI walls. The processor inside the side wall camera is responsible for measuring the global motion vectors. The side wall camera takes pictures every 20 ms, and by looking at the global motion of pixels frame to frame, it can detect the size and direction of movements. The side wall camera uses a separate light source to adjust the brightness. In addition, due to the configuration of side wall cameras around the capsule, at least one of them is always attached to the GI wall.

3.3.4 RF transceiver unit

At this stage of designing, we are not concerned about the capsule's size, so we have hired a Lora RF module operating at 433 MHz. The Lora is configured on Transmitter/Receiver (TX/RX) mode to create a serial wireless bridge. The µC sends and receives data through the Universal asynchronous receiver-transmitter (UART) protocol.

3.3.5 IMU sensor

An Inertial measurement unit, commonly known as an IMU, is an electronic device that measures and reports orientation, velocity, and gravitational forces using accelerometers, gyroscopes, and magnetometers. The gyroscope measures angular velocity. In other words, the gyroscope says how fast the device is spinning about an axis. For this design, we have used a 9-axes IMU sensor with part number MPU-9250 and designed a PCB, as shown in Figure 3.9.

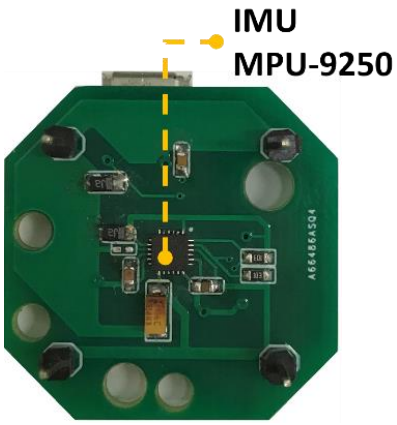

Figure 3.9 IMU sensor board

3.4 Experimental setup

A robotic arm with five axes of freedom is used for all experiments to have a precise ground truth for verification, as shown in Figure 3.10. The robotic arm is connected to a PC using RS485 cable. All information receives through a serial communication port from the PC. The robotic arm is programmed using GCODEs to simulate the capsule's motions inside the GI tract, including peristalsis, involuntary, and random movements across different trajectories. Hence, the ground truth is defined and can be used to compare with the estimated trajectory. The robotic arm has five axes of freedom, making it a suitable testbed for all experiments. The robotic arm has a grabber to pick up the capsule. The grabber is made of a non-ferromagnetic material and does not interfere with magnetic fields. So, the magnetometer inside the IMU sensor will measure the earth's magnetic fields without distortion. The test surface is placed on a tray, and the robotic arm moves the capsule on the test surface.

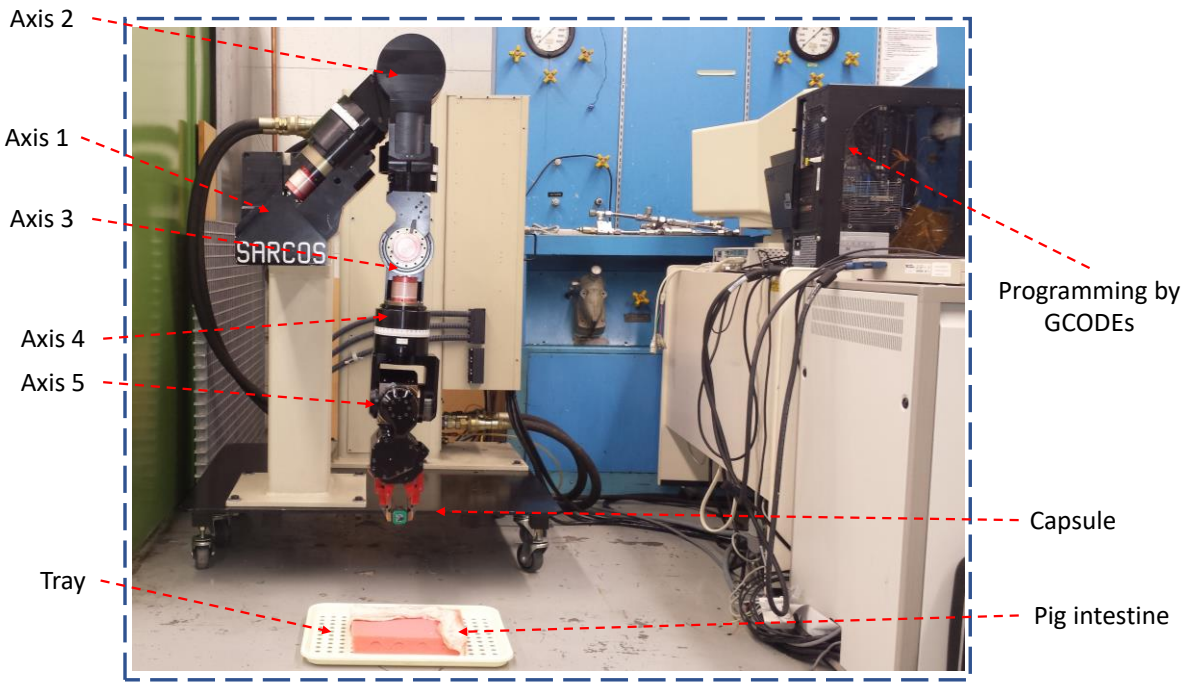

Figure 3.10 A 5 axes robotic arm experimental setup for Method 1, and a PC to control the arm

Figure 3.11 shows more details on the test setup. The surface material is another important factor and should be similar to the human intestine. A piece of pig intestine is selected and cut so the internal surface of the intestine is exposed. Figure 3.11 (d) illustrates the pig intestine.

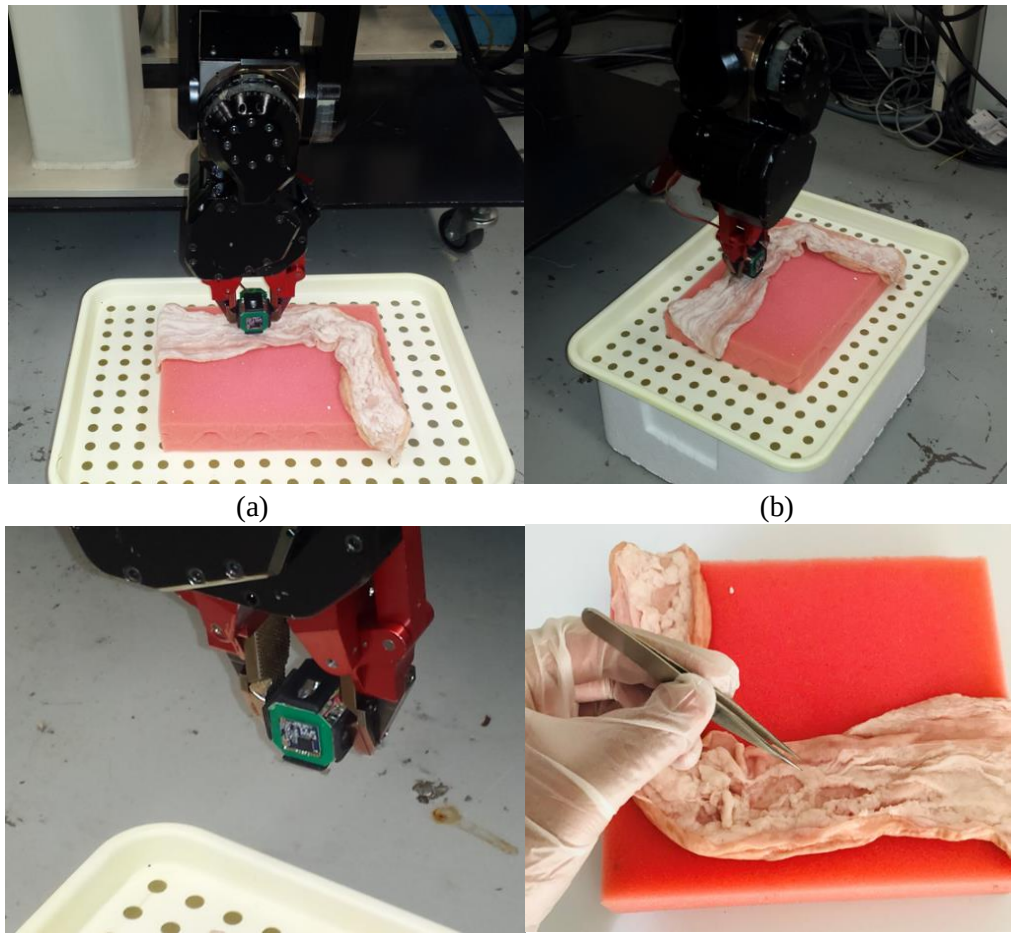

(a) (b)

(c) (d)

Figure 3.11. a & b) Robotic arm for the experimental setup, c) grabber holds the capsule, and d) porcine intestine as the test surface

One of the significant challenges in wireless communication is the possibility of data corruption during transmission and reception. The transceiver unit has a built-in capability of cyclic redundancy check (CRC)-based error detection and replies with an acknowledgment (i.e., it resends the data packet until it is successfully received), which makes it a reliable choice. However, several retries may hamper the data transmission rate in a noisy environment. To verify the performance of our prototype, we performed two additional experiments using an equivalent liquid phantom and minced meat, as shown in Figure 3.12. Since the transceiver module has a CRC functionality (i.e., detects error bits automatically), it is impossible to measure the exact BER (Bit error rate, the ratio of the number of bits received in error to the total number of bits received) in this experiment. However, considering the loss of the entire packet, we implemented test cases to measure the number of bytes lost per test case. The prototype was placed in a liquid phantom and then in minced meat of 4 pounds, as shown in Figure 3.12. The liquid phantom was made of

distilled water, methanol, and sodium chloride to mimic human GI fluids [103], [104]. The chamber size of liquid phantom and minced meat were: 40 cm × 30 cm × 16.5 cm (Length × Width × Height) and 26 cm × 17cm × 7cm (Length × Width × Height), respectively. The capsule was placed in the middle of the chamber in all test cases. The distance between the capsule and the data logger varied gradually from 0.3 m to 10 m.

(a) (b)

Figure 3.12 Experimental setup to test the transmission rate of the capsule in (a) liquid phantom and (b) minced meat

3.5 Data structure

Figure 3.13 shows the raw recorded data in excel format. As illustrated, each file consists of 13 columns. From left to right, columns A and B present the internal timer, and the algorithm uses this information for synchronization. Columns C and D present displacement in the y and x-axis, respectively. As mentioned earlier, the capsule can only move in the x direction due to the GI tract's tubular shape. Hence, the algorithm ignores the y displacements. Columns E, F, and G are accelerometer data for the x, y, and z axes, respectively. H, I, and J columns are the gyroscope data. Finally, K, L, and M columns present data for the magnetometer.

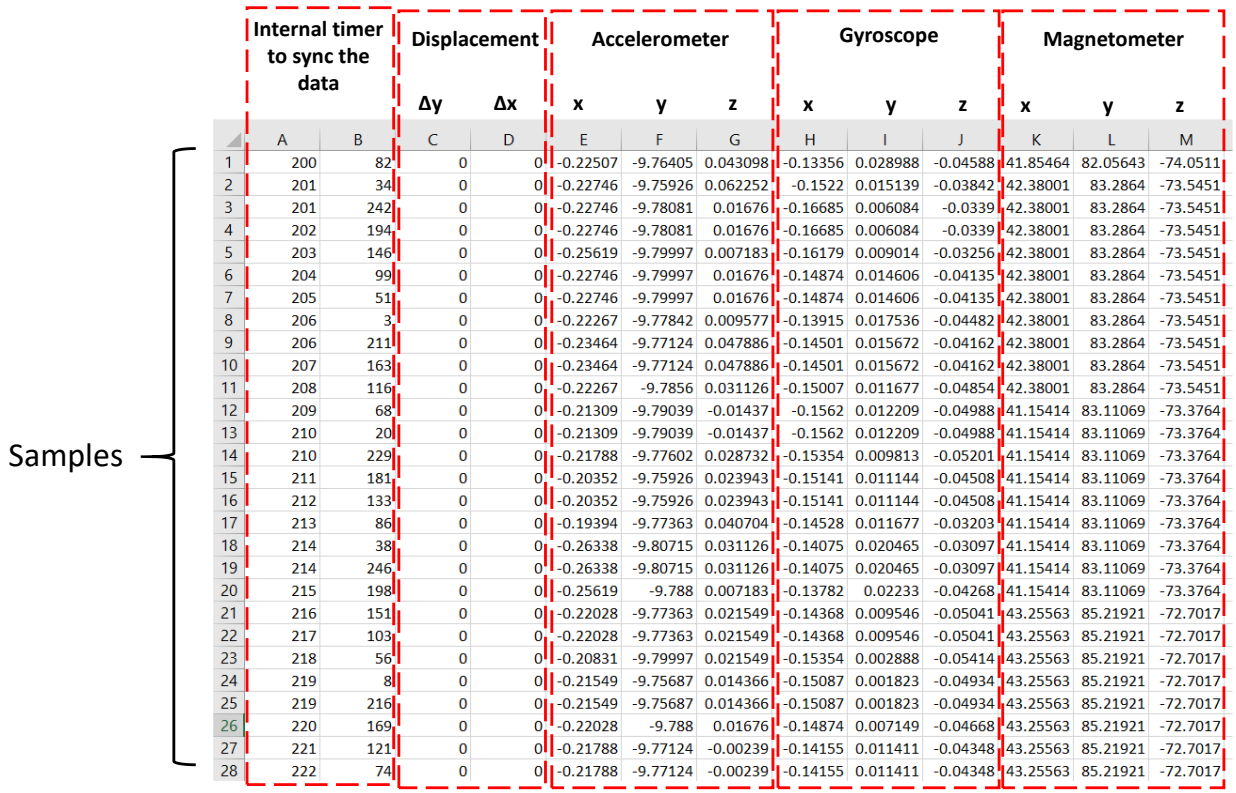

	A	B	C	D	E	F	G	H	I	J	K	L	M
1	200	82	0	0	-0.22507	-9.76405	0.043098	-0.13356	0.028988	-0.04588	41.85464	82.05643	-74.0511
2	201	34	0	0	-0.22746	-9.75926	0.062252	-0.1522	0.015139	-0.03842	42.38001	83.2864	-73.5451
3	201	242	0	0	-0.22746	-9.78081	0.01676	-0.16685	0.006084	-0.0339	42.38001	83.2864	-73.5451
4	202	194	0	0	-0.22746	-9.78081	0.01676	-0.16685	0.006084	-0.0339	42.38001	83.2864	-73.5451
5	203	146	0	0	-0.25619	-9.79997	0.007183	-0.16179	0.009014	-0.03256	42.38001	83.2864	-73.5451
6	204	99	0	0	-0.22746	-9.79997	0.01676	-0.14874	0.014606	-0.04135	42.38001	83.2864	-73.5451
7	205	51	0	0	-0.22746	-9.79997	0.01676	-0.14874	0.014606	-0.04135	42.38001	83.2864	-73.5451
8	206	3	0	0	-0.22267	-9.77842	0.009577	-0.13915	0.017536	-0.04482	42.38001	83.2864	-73.5451
9	206	211	0	0	-0.23464	-9.77124	0.047886	-0.14501	0.015672	-0.04162	42.38001	83.2864	-73.5451
10	207	163	0	0	-0.23464	-9.77124	0.047886	-0.14501	0.015672	-0.04162	42.38001	83.2864	-73.5451
11	208	116	0	0	-0.22267	-9.7856	0.031126	-0.15007	0.011677	-0.04854	42.38001	83.2864	-73.5451
12	209	68	0	0	-0.21309	-9.79039	-0.01437	-0.1562	0.012209	-0.04988	41.15414	83.11069	-73.3764
13	210	20	0	0	-0.21309	-9.79039	-0.01437	-0.1562	0.012209	-0.04988	41.15414	83.11069	-73.3764
14	210	229	0	0	-0.21788	-9.77602	0.028732	-0.15354	0.009813	-0.05201	41.15414	83.11069	-73.3764
15	211	181	0	0	-0.20352	-9.75926	0.023943	-0.15141	0.011144	-0.04508	41.15414	83.11069	-73.3764
16	212	133	0	0	-0.20352	-9.75926	0.023943	-0.15141	0.011144	-0.04508	41.15414	83.11069	-73.3764
17	213	86	0	0	-0.19394	-9.77363	0.040704	-0.14528	0.011677	-0.03203	41.15414	83.11069	-73.3764
18	214	38	0	0	-0.26338	-9.80715	0.031126	-0.14075	0.020465	-0.03097	41.15414	83.11069	-73.3764
19	214	246	0	0	-0.26338	-9.80715	0.031126	-0.14075	0.020465	-0.03097	41.15414	83.11069	-73.3764
20	215	198	0	0	-0.25619	-9.788	0.007183	-0.13782	0.02233	-0.04268	41.15414	83.11069	-73.3764
21	216	151	0	0	-0.22028	-9.77363	0.021549	-0.14368	0.009546	-0.05041	43.25563	85.21921	-72.7017
22	217	103	0	0	-0.22028	-9.77363	0.021549	-0.14368	0.009546	-0.05041	43.25563	85.21921	-72.7017
23	218	56	0	0	-0.20831	-9.79997	0.021549	-0.15354	0.002888	-0.05414	43.25563	85.21921	-72.7017
24	219	8	0	0	-0.21549	-9.75687	0.014366	-0.15087	0.001823	-0.04934	43.25563	85.21921	-72.7017
25	219	216	0	0	-0.21549	-9.75687	0.014366	-0.15087	0.001823	-0.04934	43.25563	85.21921	-72.7017
26	220	169	0	0	-0.22028	-9.788	0.01676	-0.14874	0.007149	-0.04668	43.25563	85.21921	-72.7017
27	221	121	0	0	-0.21788	-9.77124	-0.00239	-0.14155	0.011411	-0.04348	43.25563	85.21921	-72.7017
28	222	74	0	0	-0.21788	-9.77124	-0.00239	-0.14155	0.011411	-0.04348	43.25563	85.21921	-72.7017

Figure 3.13 Raw data received from the capsule and stored in an excel file

Chapter 4

Results and discussion for Method 1

4.1 Surface pattern

The surface pattern is one of the critical properties that can influence the side wall camera performance. As depicted in Figure 4.1 (a), some basic patterns are prepared and printed on a sheet to understand the behavior of the side wall camera on various surface patterns. Patterns are expanded on horizontal columns and printed on a white sheet. The side wall camera is placed on these patterns, and the robotic arm moves the capsule on a predefined trajectory. The results showed that the YS8008B could measure the displacement in all patterns except parallel patterns. Furthermore, the sensor's sensitivity and lens' focal length are important properties. In the real-world scenario, the capsule is placed on intestine tissues. Our experiments are extended to explore the side wall camera performance on colored patterns, as shown in Figure 4.1 (b).

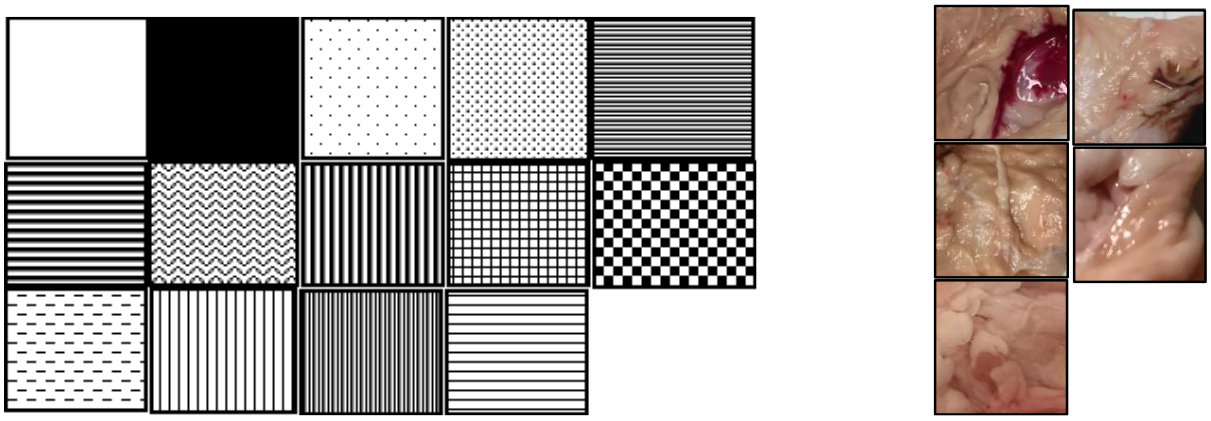

(a) (b)

Figure 4.1. (a) Basic patterns, (b) colored patterns that are printed on a sheet

The next objective is to see whether the camera can track the motion on a soft surface (like animal skin or meat). The surface's material defines the optical reflection properties of that surface. Several materials are selected, such as porcine intestine, ground meat, and human skin. The capsule is equipped with four side wall cameras. Hence, at least one of them is attached to the surface, and it can measure displacements. The initial experiment shows that the side wall camera can measure the traveled distance on soft surfaces like the porcine intestine.

Figure 4.2 shows that the surface consists of several tiny patterns visible under a magnifier, and the side wall camera captures these tiny patterns. The image processing unit tracks these

patterns and calculates the global motion. The side wall camera reports the displacement toward its *x* and *y*-axis.

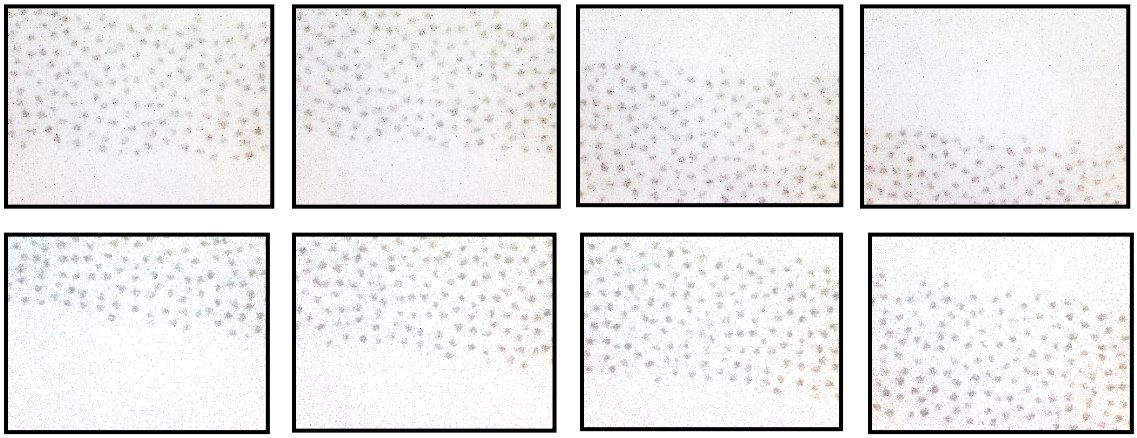

Figure 4.2. A surface consists of several tiny patterns visible under a magnifier, and the side wall camera captures these tiny patterns

4.2 1D tracking

This experiment is designed to evaluate the accuracy of the side wall camera for distance measurements. A robotic arm moves the capsule toward the *x* direction, and the side wall camera measures the distances. Figure 4.3 presents the 1D tracking data, in which Figure 4.3(a) is the raw data from the side wall camera. The slope of the traveled distance plot indicates the velocity. Figure 4.3(b) illustrates the IMU data and shows minimal changes in gyroscope and magnetometer outputs, which means that the heading vector was not changed. Figure 4.3(c) is the output of our fusion algorithm (estimated trajectory).

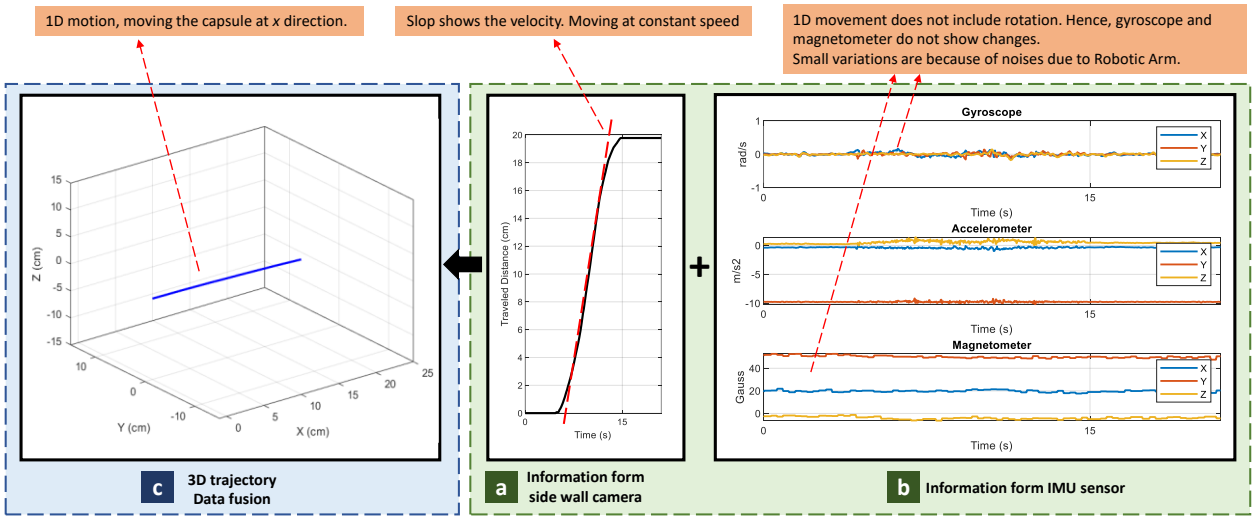

Figure 4.3. Results of 1D tracking, in which a) shows the cumulative displacement captured by side wall camera, b) IMU sensor data, and c) estimated 3D trajectory by Method 1

Figure 4.4 illustrates another experiment to evaluate the motion sensors' accuracy. In this experiment, the capsule traveled 15, 30, and 60 cm in a straight line. Each experiment was repeated three times. Figure 4.4 (a) shows that positioning errors are 3%, 3.1%, and 3.71% for 15, 30, and 60 cm displacements, respectively. Figure 4.4 (b) illustrates the positioning error. It is shown that the positioning error will increase as the capsule moves farther due to the accumulation of errors caused by the side wall camera.

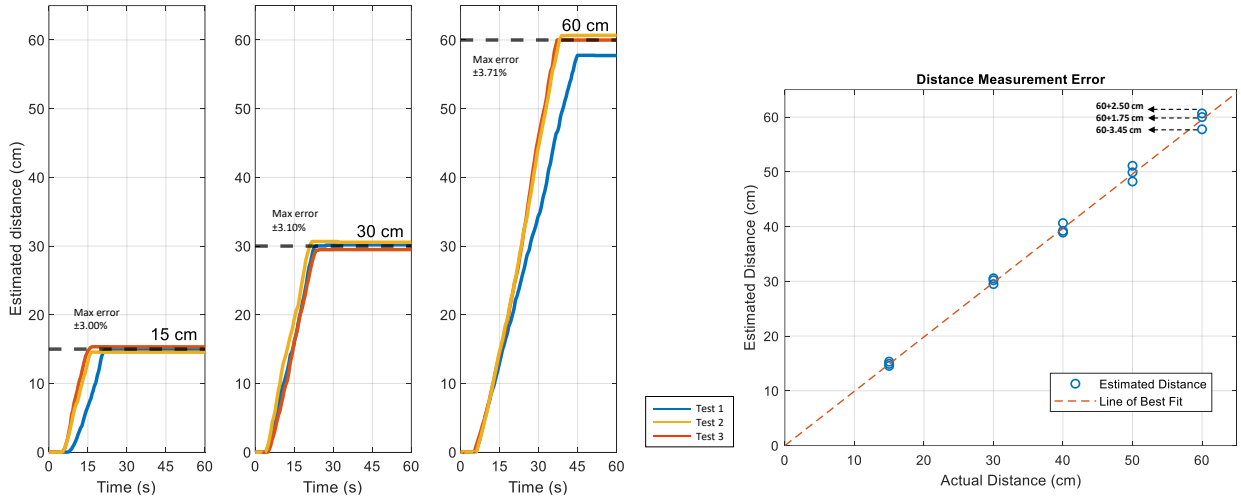

(a) (b)

Figure 4.4. (a) Estimated distance captured by side wall camera for 15, 30, and 60 cm. (b) positioning error of various path lengths.

4.3 Leap and peristalsis motions

Leap and peristalsis motions are two common motions inside the GI system. Leap motion consists of a series of fast and small movements. This experiment is performed to understand whether the side wall camera can detect surge motions. The side wall camera captures images at every sampling time (T_s). So, the frame rate plays a key role. The YS8008B measures the displacement between two samples and sends the information to the host. Hence, T_s limits the maximum speeds. Shorter T_s makes the buffer overflow and misses the displacement; as a result, the positioning error will increase. On the other hand, longer T_s leads to higher drift error. The capsule is moved at 0.5 cm/s, 2 cm/s, 5 cm/s, and 7 cm/s as depicted in Figure 4.5. The results show that the side wall camera can successfully track velocity up to 7 cm/s.

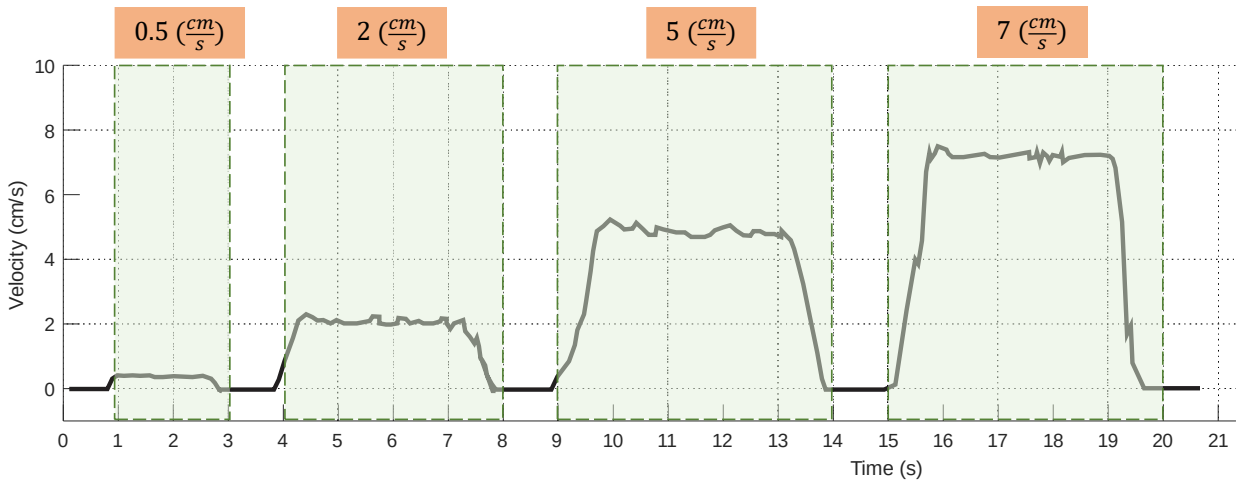

Figure 4.5. Leap motion analysis while the capsule is moving at different speeds.

In another experiment, the peristalsis motion is investigated. Peristalsis motion is an involuntary contraction and relaxation of muscles that push the foods ahead of the wave. The muscle's contraction behind the food keeps it from moving backward. Then longitudinal contraction pushes the capsule forward. Commonly, peristaltic waves exist in the small intestine at irregular intervals and travel for different distances. Tracking an object under peristalsis motion could be difficult since the object might go forward and slightly backward.

In this experiment, the robotic arm moves forward and backward in the *x* direction to simulate the GI peristalsis motion. Figure 4.6 illustrates a peristalsis motion. Figure 4.6(c) shows the estimated 3D trajectory. The results show a relationship between the direction of travel and acceleration, as shown in Figure 4.6(b). The blue and yellow plots show accelerations across the *x* and *z* axes. The acceleration is visible only in the heading vector direction.

The peristalsis motion's sequence includes:

1) Forward motion
   i. constant speed (velocity: +, acceleration: 0)
2) Backward motion
   i. slow down until complete stop (velocity: +, acceleration: -)
   ii. speed up at opposite direction (velocity: -, acceleration: +)
3) Forward motion
   i. slow down until complete stop (velocity: -, acceleration: -)
   ii. speed up at opposite direction (velocity: +, acceleration: +)

This sequence is depicted in Figure 4.6. The size of acceleration depends on the rate of velocity changes.

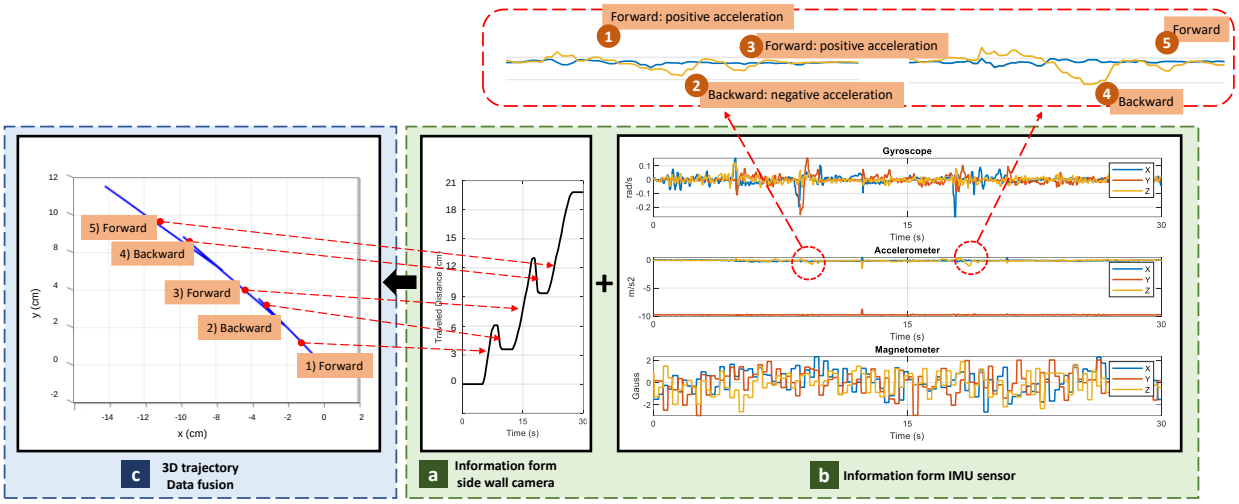

Figure 4.6. Peristalsis motion analysis. The capsule is pushed forward. Then slightly, it is pushed backward.

Figure 4.7(a) shows how peristalsis motion works. Due to the contraction of muscles, we could ensure that side wall cameras will stick to the GI wall. The experiments are performed in Two-Dimensional (2D) space to monitor the side wall camera behaviors in such movement. Figure 4.7(b) illustrates the effect of peristalsis motion in the experiment. The capsule travels on a 15 cm path, and it moves forward and backward several times during the path. The results show that the error in the estimated distance is around 7.4%.

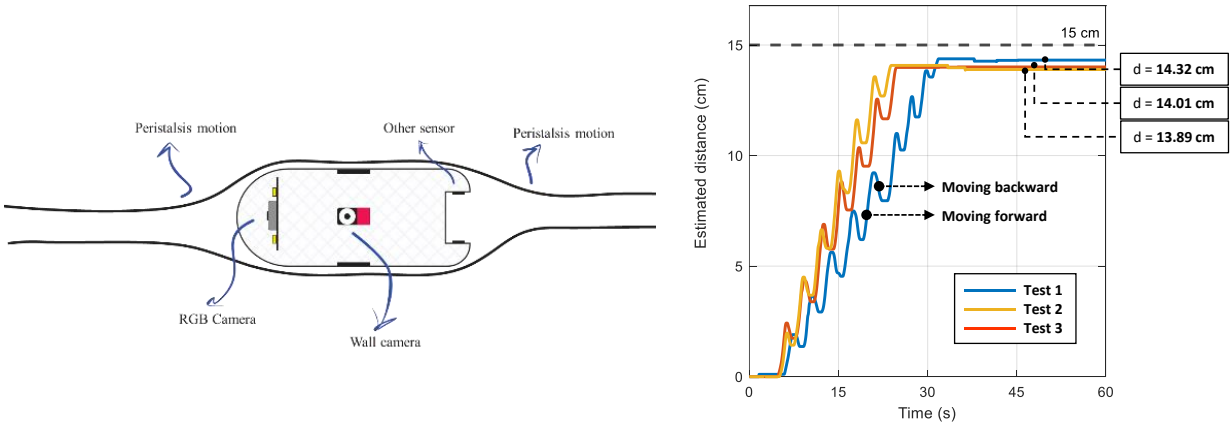

(a) (b)

Figure 4.7. (a) Peristalsis motion, contraction, and relaxation of muscles which leads to pushing food ahead of the wave, (b) experiment results.

4.4 Relative motion

In relative motion, the capsule remains stationary with respect to the GI tract, but it moves with respect to the body coordinate. The capsule is placed inside the intestine, and the side wall camera will not detect any motion during relative motion (Figure 4.8 (a)). However, the relative motion changes IMU data (Figure 4.8 (b)). Based on the proposed Method 1, if the displacement is zero, the 3D trajectory shows a single point with no motion (Figure 4.8 (c)). The results show that Method 1 can reject the relative motion of the GI tract and only consider the actual motion of the capsule inside the intestine.

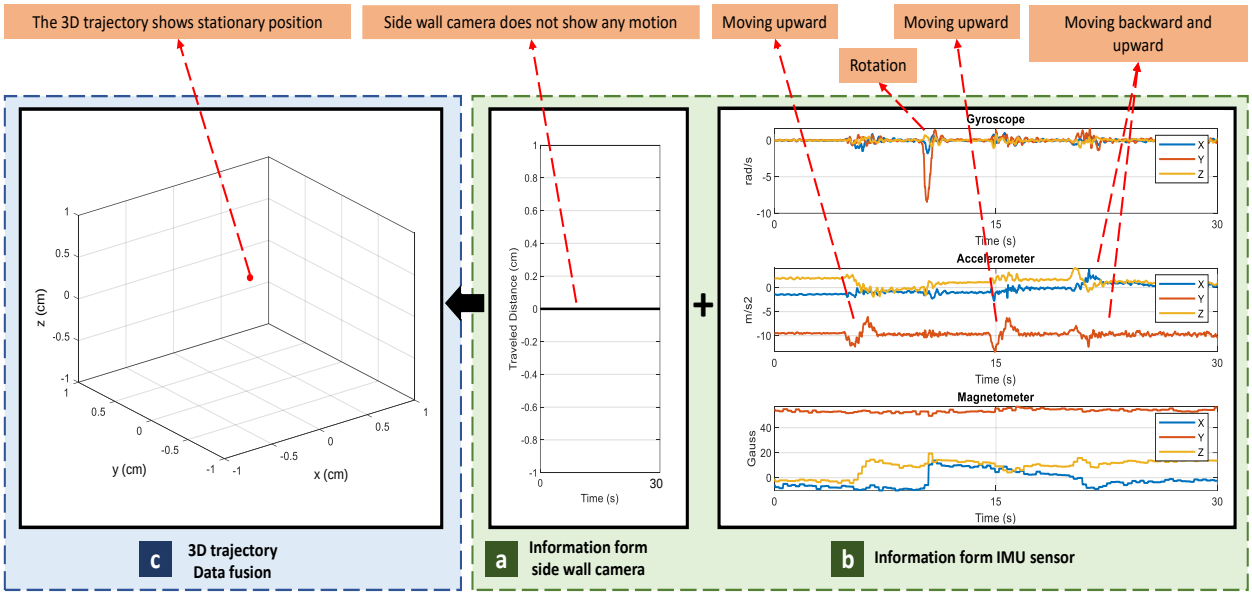

Figure 4.8. Results of Involuntary motion analysis. The side wall camera does not show any motion, as the capsule is stationary with respect to the GI tract.

4.5 3D tracking

A robotic arm moves the capsule based on a predefined trajectory (ground truth). Several tracks are examined, but only three of them are shown in Figure 4.9. Then, the proposed algorithm fuses the side wall camera and IMU sensor information to estimate the 3D trajectory. For the sake of explanation, the recorded data from the trajectory of Figure 4.9 (a) will be described.

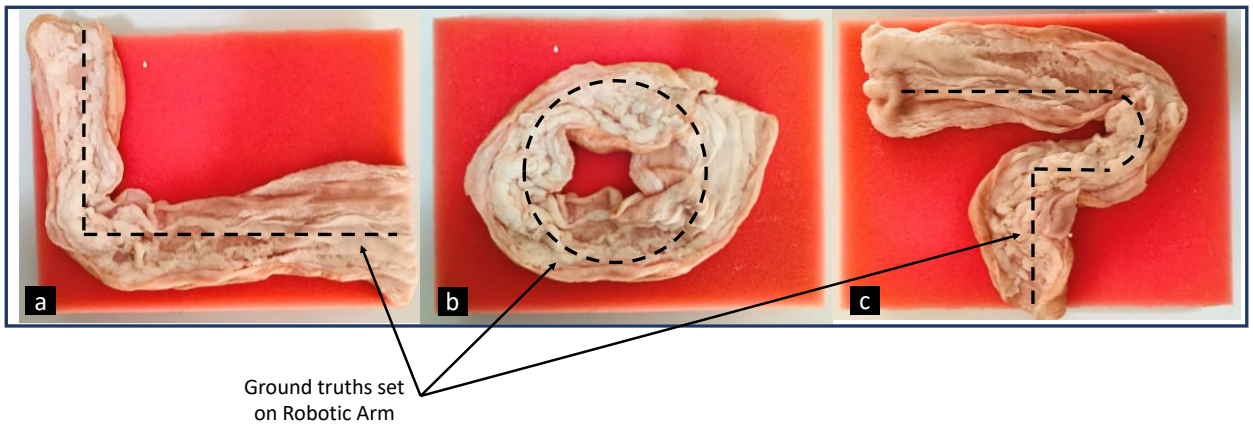

Figure 4.9. A piece of porcine intestine for the test surface

As illustrated in Figure 4.10, the trajectory is divided into three sections, 1) moving with constant speed at $V_{heading(1)}$, 2) 90-degree rotation, 3) moving with constant speed at $V_{heading(2)}$. As shown in Figure 4.10(a), during (1) and (3), the side wall camera detects motions, but during (2), it does not show any motion. Instead, IMU data shows rotation during this time.

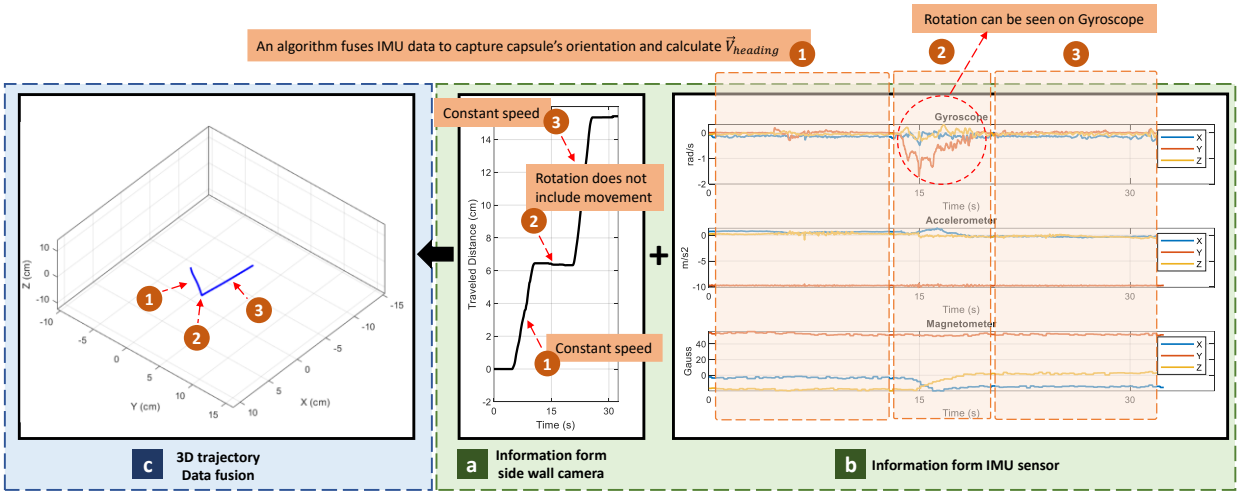

Figure 4.10. Results of 3D tracking analysis of L shape motion.

Several experiments are shown in Figure 4.11. For each experiment, three plots are reported, (a) Cumulative displacement data from the side wall camera, which is denoted as traveled distance, (b) Raw data from the IMU sensor, and (c) The 3D traveled trajectory. In this plot, the dashed line shows the ground truth, and the blue line indicates the estimated trajectory from the proposed algorithm. According to the results, the proposed method could estimate the position with 7.4% accuracy.

The side wall cameras should touch the GI wall; otherwise, it does not measure the displacement correctly. In the stomach, the side wall camera will not touch the surface, which may result in positioning errors.

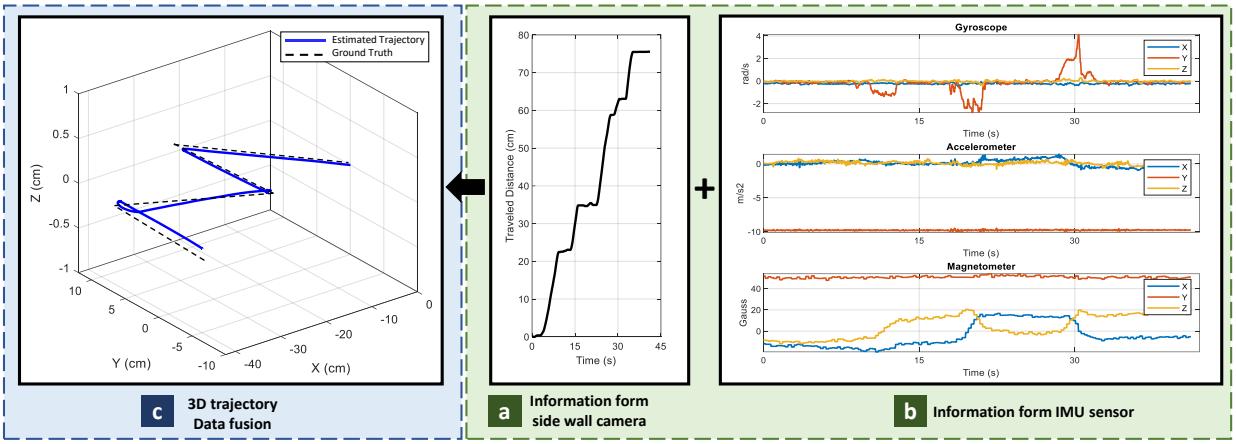

(a)

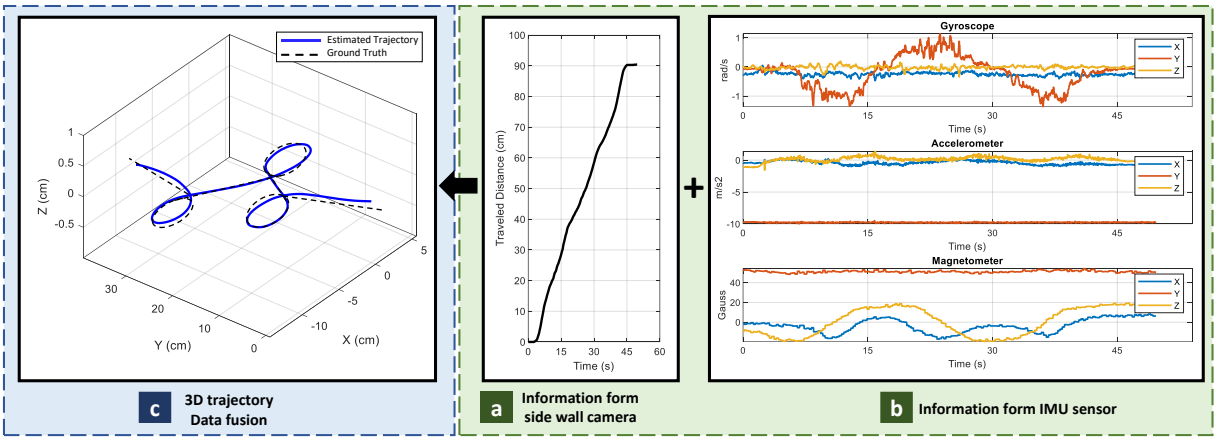

(b)

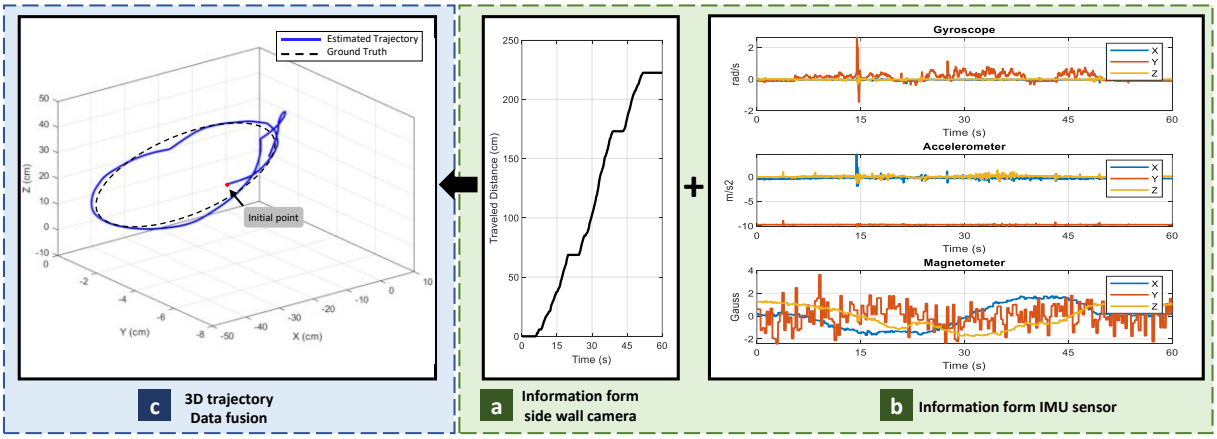

(c)

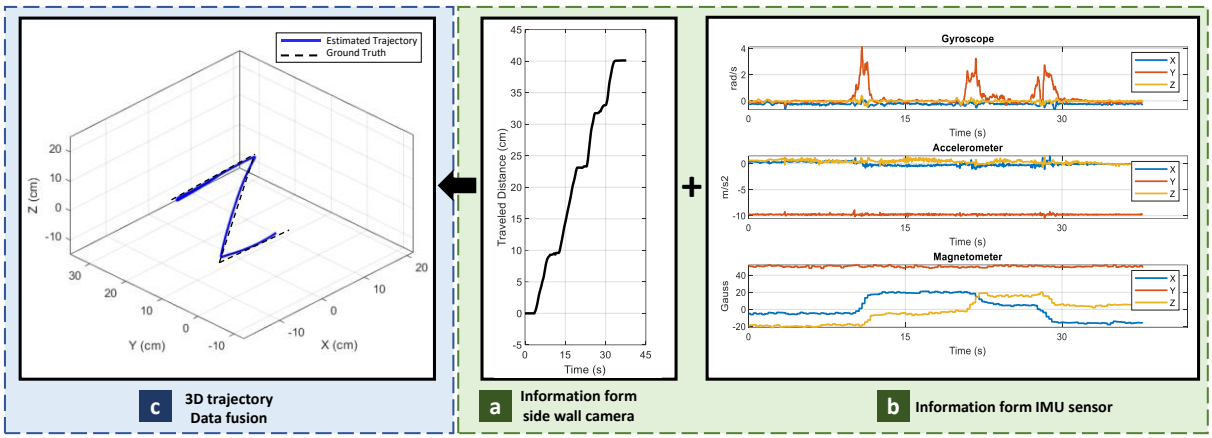

(d)

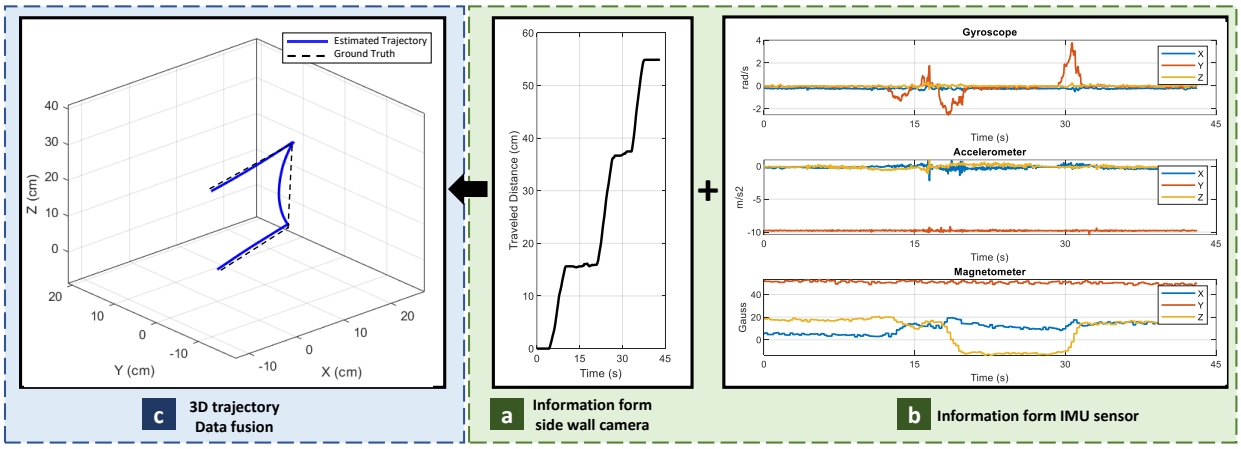

(e)

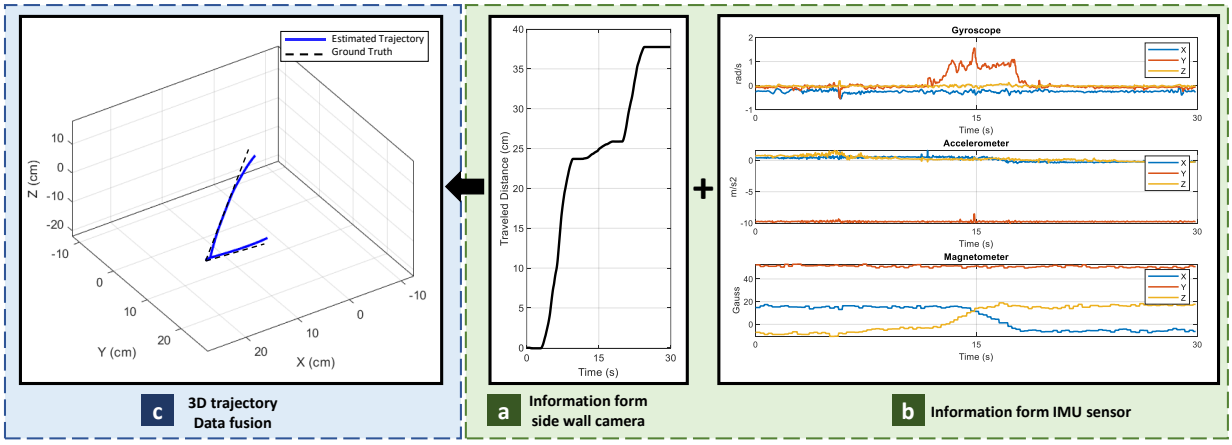

(f)

Figure 4.11. 3D tracking for several trajectories is reported, including traveled distance, IMU data, and computed trajectory.

4.6 Validation experiment

This experiment aims to examine the feasibility of tracking inside the intestine. Figure 4.12 shows the test setup for validation experiments. The capsule was manually inserted into the porcine intestine and pushed through it. Since it is an in-vitro experiment, the ground truth is measured by hand. The results show that the capsule can enter the pig's intestine.

(a) (b) (c)

Figure 4.12. Test setup with the porcine intestine. The capsule is placed inside the pig intestine

4.7 Pseudo-body effect

In a real-world scenario, the capsule enters the digestive system, and human tissues, bones, etc., surround it. Hence, it is important to investigate the effect of the body on the localization method. The capsule is placed at a pseudo-body setup for this experiment, as illustrated in Figure. 4.13, then the capsule starts to send the data out.

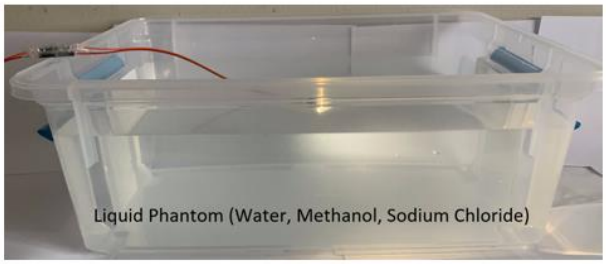

(a)

(b)

Figure 4.13 Measurement setup to test the transmission rate of the proposed capsule in (a) liquid phantom (b) minced meat

All data were transmitted to the data logger with no loss when the distance between the data logger and the capsule in the liquid phantom was up to 5 m. When the distance increased to 10 m, we noticed the loss of data packets, and the transmission rate was 90%. In another test case, the capsule was placed in minced meat. Like before, when the distance between the capsule and the data logger was varied up to 5 m, no loss of data packets was observed. However, when the distance increased to 10 m, we noticed that the transmission rate was affected by 80%. Since the data logger is wearable and generally worn around the waist in practice, the distance between a swallowed capsule and the data logger is generally about 0.3 m [105]. Therefore, we expect our prototype to work with no loss of data during communication.

Table 4.1: Transmission performance of the capsule

Experiment	**Distance between capsule and data logger (m)**	**Transmitted bytes**	**Received bytes**	**Percentage of transmitted data (%)**
Liquid phantom	0.3	20	20	100
	3	20	20	100
	5	20	20	100
	10	20	18	90
Minced meat	0.3	20	20	100
	3	20	20	100
	5	20	20	100
	10	20	16	80

4.8 Extra experiments

Several experiments have been performed, and their estimated trajectories are depicted below in Figure 4.14. The blue line shows the estimated trajectory, and the black dashed line is the ground truth. The results show that the proposed method can track the capsule, but it has some limitations. First, due to the accumulation of errors from the side wall camera, the tracking method tends to drift in position over time. Second, this method cannot track the sharp edges. In a 90-degree rotation, the robotic arm rotates the capsule; however, during this motion, the side wall camera still measures displacement along its *x* axis, resulting in a curve edge. It should be noted that sharp edge movements do not occur due to the characteristics of the GI path.

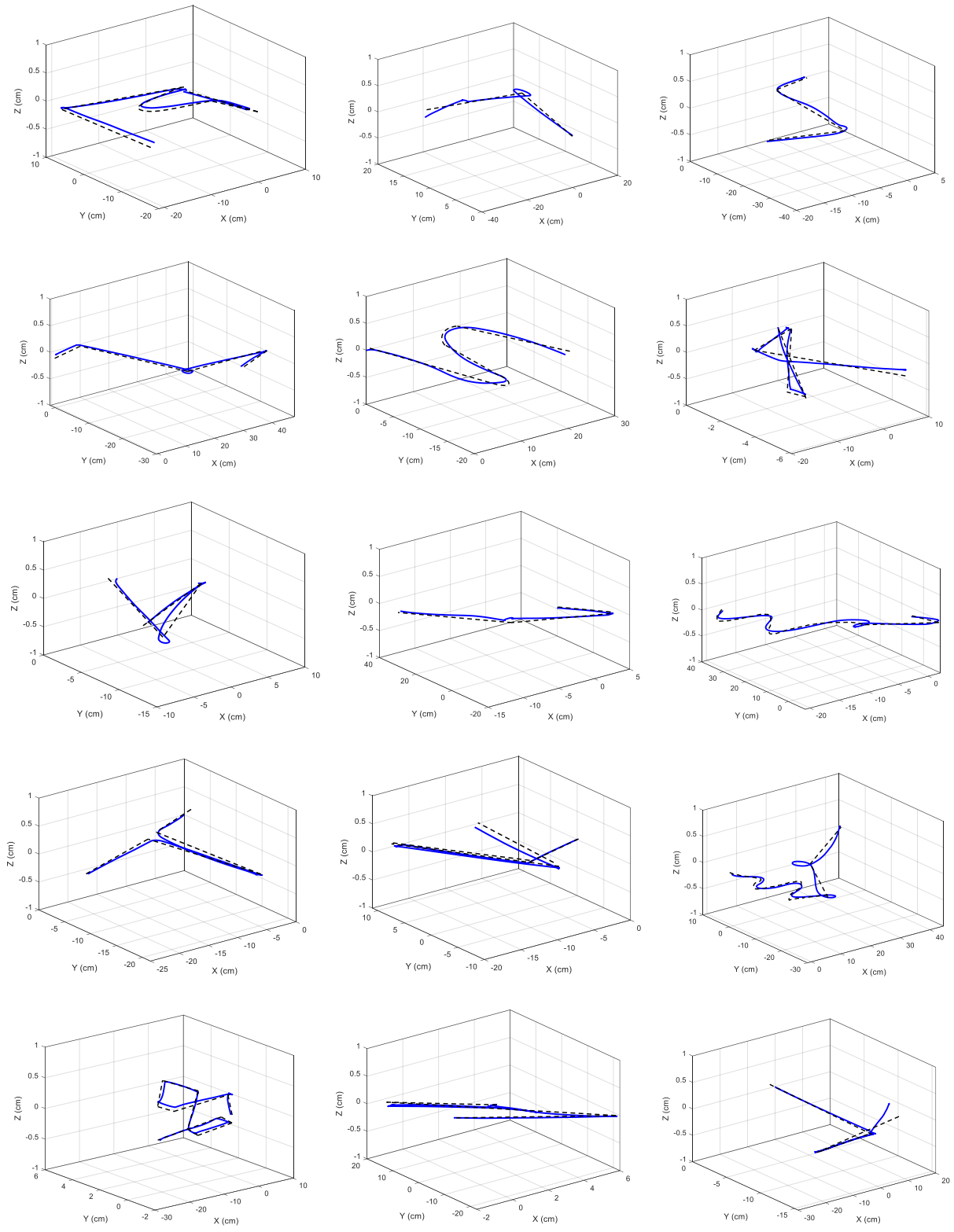

Figure 4.14 The estimated trajectories for some of the experiments

4.9 Power consumption

Due to the small size of the capsule, there is limited space remaining for batteries, and it must power up the device throughout the process, which takes around 8 hours. In this section, the power consumption of the capsule is investigated. Table 4.2 presents the device's operating voltage and current in active mode at 3.3 V. To work properly for 8 hours, the capsule needs a battery with a 94 mAh capacity. However, integrating all the required components in an integrated chip (IC) will lower the power consumption significantly.

Table 4.2. Power consumption of the capsule prototype

Component	**Current (mA)**	**Power Consumption (mW)**
MPU9250	1.84	6.07
ATmega32	1.23	4.06
Red LED	1.28	4.22
Lora	5.25	17.32
Motion sensor	2.10	6.93
Total	**11.70**	**38.61**

Chapter 5

Localization using magnet senor and side wall camera (Method 2)

5.1 Introduction

In Method 1, the side wall camera can distinguish between the capsule's motion and the relative motion of the GI tract. However, side wall cameras' errors will accumulate, so the estimated track tends to deviate from its ground truth, worsening over time. Furthermore, there is no global positioning defined in Method 1 to recalibrate the capsule's position. In Method 2, a magnetic localization is added to the capsule to recalibrate the capsule's position and compensate for the side wall camera's errors. Magnetic localization is considered a promising option for WCE localization [66] and has been investigated by several researchers till now. However, this method has deficiencies that could be overcome by a hybrid method proposed in this chapter. The primary focus of the Method 2 is to localize the capsule inside the intestine, as CE could not reach out to this section of the GI system. The capsule is integrated with a tiny permanent magnet and a magnetometer sensor array wrapped around the patient's body to measure the magnetic field and estimate the capsule's global position. In addition, the magnetic moment vector ($\vec{H}$) will be calculated simultaneously. The magnetic moment shows the capsule's direction of travel while side wall cameras [38] distinguish the capsule's motion from the GI tract's relative motion.

5.2 Materials and methods

5.2.1 Magnetic localization

Magnetic localization has two main elements: a small magnet integrated inside the capsule and a sensor array (sensor belt) placed on the patient's body. The sensor belt is an array of magnetometer sensors that can measure the magnetic field in three axes. Figure 5.1 shows an overall view of this method. Equation (5.1) represents the magnetic field [84]:

$$B_i = \nabla \times \left(\frac{\mu_r \mu_0 M_T}{4\pi r_i^2} . \frac{\vec{H} \times \vec{P}_i}{r_i} \right)$$

$$B_i = \frac{\mu_r \mu_0 M_T}{4\pi} \left(\frac{3(\vec{H}.\vec{P}_i)\vec{P}_i}{r_i^5} - \frac{\vec{H}}{r_i^3} \right)$$

$$B_T \left(\frac{3(\vec{H}.\vec{P}_i)\vec{P}_i}{r_i^5} - \frac{\vec{H}}{r_i^3} \right) = \left[B_{ix}, B_{iy}, B_{iz} \right]^T \qquad (5.1)$$

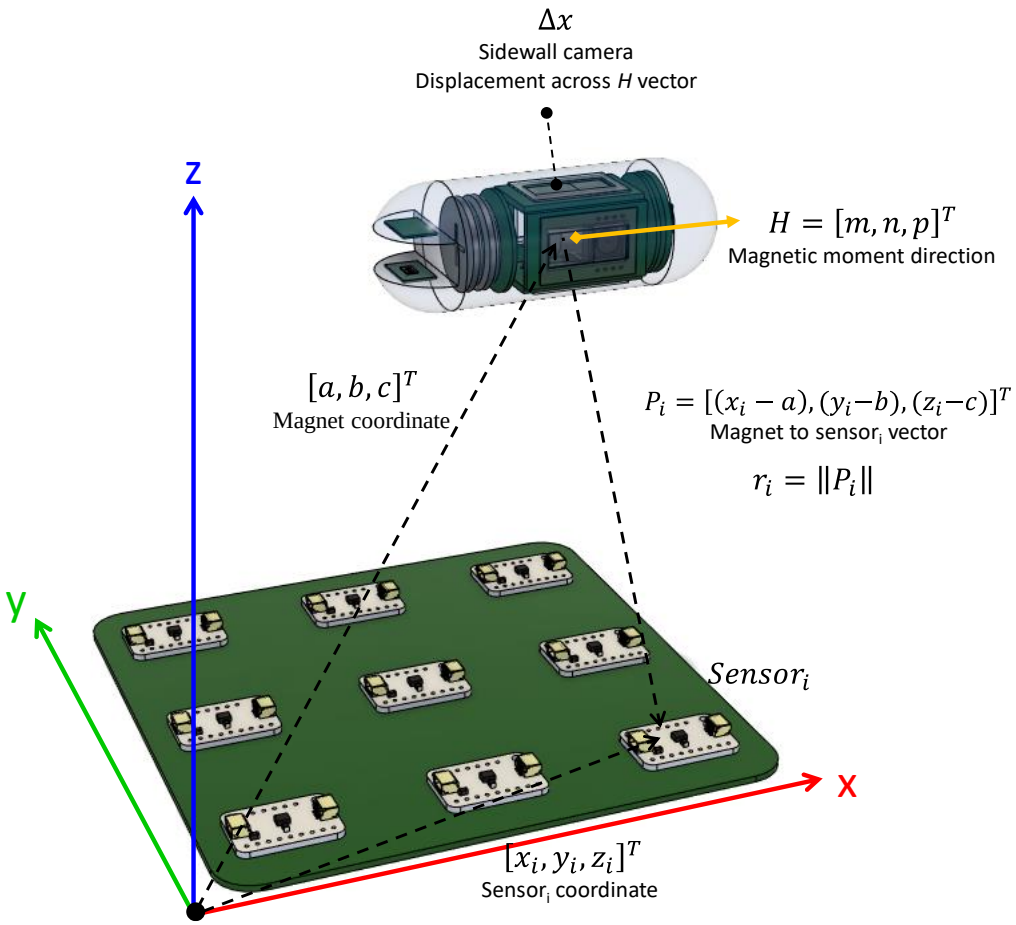

Figure 5.1 An overview of the magnetic localization method. A small magnet is integrated into the capsule, and an array of magnetometer sensors is provided to capture the magnetic fields.

which, B_i is the magnetic field at the i^{th} sensor, and $\left[B_{ix}, B_{iy}, B_{iz}\right]^T$ presents its matrix form. μ_r is relative permeability, μ_0 is permeability in a vacuum, and M_T is a constant based on the magnet. $\vec{H}$ is the magnet moment unit vector. $\vec{P}_i$ is a vector span from the magnet to the i^{th} sensor with the norm of r_i. The $\frac{\mu_r \mu_0 M_T}{4\pi}$ is abbreviated to B_T for further simplification. According to equation (5.2), the $\vec{H}$ is shown in matrix format and consists of three elements *m*, *n*, and *p*. The magnet coordinates are $[a, b, c]^T$, and $the\ i^{th}$ sensor is placed at $[the\ x_i, y_i,\ and\ z_i]^T$ coordinates.

$$\begin{cases} H = [m, n, p]^T \\ s.t.\ m^2 + n^2 + p^2 = 1 \\ P_i = [x_i - a, y_i - b, z_i - c]^T \\ r_i = \|P_i\| = \sqrt{(x_i - a)^2 + (y_i - b)^2 + (z_i - c)^2} \end{cases} \quad (5.2)$$

By combining equation (5.2) with equation (5.1), we have equation (5.3).

$$B_{\mathrm{ix}} = B_T \left\{ \frac{3[m(x_i - a) + n(y_i - b) + p(z_i - c)](x_i - a)}{r_i^5} - \frac{m}{r_i^3} \right\}$$

$$B_{\mathrm{iy}} = B_T \left\{ \frac{3[m(x_i - a) + n(y_i - b) + p(z_i - c)](y_i - b)}{r_i^5} - \frac{n}{r_i^3} \right\}$$

$$B_{\mathrm{iz}} = B_T \left\{ \frac{3[m(x_i - a) + n(y_i - b) + p(z_i - c)](z_i - c)}{r_i^5} - \frac{p}{r_i^3} \right\} \qquad (5.3)$$

Hence, a set of six parameters ($[a, b, c]^T$ and $[x_i, y_i, z_i]^T$) is unknown in each sensor. B_{im} is the measured magnetic field by an i^{th} sensor which is a superposition of B_i, earth magnetic field (B_{ig}), noises (B_{noise}), and differential magnetic caused by the dipole (ΔB_{dipole}) as equation (5.4) shows [84].

$$B_{im} = B_i + B_{ig} + B_{noise} + \Delta B_{dipole} \quad (5.4)$$

The ΔB_{dipole} is usually tiny, and B_{noise} can be ignored. To remove the effect of the earth's magnetic field, every binary combination of i^{th} and j^{th} sensor measurement will be subtracted. This mathematically can be presented as equation (5.5).

$$B_{im} - B_{jm} = B_i - B_j + B_{ig} - B_{jg} \quad (5.5)$$

The earth's magnetic field will be the same for adjacent sensors. Hence, the result would be equation (5.6).

$$B_{ig} = B_{jg}$$

$$B_{im} - B_{jm} = B_i - B_j$$

$$\Delta B_{ijm} = \Delta B_{ij} \qquad (5.6)$$

The matrix form equation (5.6) can be represented as equation (5.7).

$$\begin{bmatrix} B_{imx} - B_{jmx} \\ B_{imy} - B_{jmy} \\ B_{imz} - B_{jmz} \end{bmatrix} = \begin{bmatrix} B_{ix} - B_{jx} \\ B_{iy} - B_{jy} \\ B_{iz} - B_{jz} \end{bmatrix} \qquad (5.7)$$

The error between the differential signal of measured data and theoretical measurement can be written as equation (5.8).

$$E_{l_{\mathrm{ij}}} = \left\|\Delta B_{\mathrm{ijm}} - \Delta B_{\mathrm{ij}}\right\|^2 \qquad (5.8)$$

where, $E_{l_{\mathrm{ij}}}$ is the error of differential signals. Finally, the total error would be equation (5.8). A particle swarm optimization (PSO) [106] algorithm minimizes the total error. Consequently, the magnet location $[a, b, c]^T$ and magnet moment $[m, n, p]^T$ will be driven.

$$E_L = \sum_{i,j} E_{l_{\mathrm{ij}}} \qquad (5.9)$$

Two types of distortion may influence magnetic sensors - hard iron and soft iron distortions. Hard iron distortion is created by materials that produce magnetic fields. This distortion applies a constant additive field to the magnetic sensor output. Hence, a bias should be added to the measured data to cancel that. Soft iron distortion is caused by ferromagnetic materials, leading to deflections and magnetic field alterations. A correction matrix should be used to compensate for that. The calibration formula is expressed mathematically in equation 5.10 [100].

$$\begin{bmatrix} B_{cx} \\ B_{cy} \\ B_{cz} \end{bmatrix} = \begin{bmatrix} S_{11} & S_{12} & S_{13} \\ S_{21} & S_{22} & S_{23} \\ S_{31} & S_{32} & S_{33} \end{bmatrix} \times \begin{bmatrix} B_{\mathrm{mx}} \\ B_{\mathrm{my}} \\ B_{\mathrm{mz}} \end{bmatrix} + \begin{bmatrix} b_x \\ b_y \\ b_z \end{bmatrix} \qquad (5.10)$$

where, B_{cx}, B_{cy}, and B_{cz} are calibrated magnetic fields. B_{mx}, B_{my}, and B_{mz} measure magnetic fields from a magnetic sensor. b_x, b_y, and b_z are biasing matrix elements to cancel the hard iron effect, and S_{mn} is correction matrix elements to eliminate the soft iron distortion.

5.2.2 Side wall camera

The GI system uses a mechanism known as peristalsis motion to push food ahead of its track. It contracts and relaxes muscles around the food in a wave pattern to push the food through its cylindrical structure. A method is developed to localize the capsule using a side wall camera. A miniaturized monochromic camera is integrated into the capsule's side and uses odometry techniques to measure displacement. As shown in Figure 5.2 (a), when the capsule enters the GI, the muscles are contracted and continuously surround it. Hence, the side wall camera touches the GI wall, and its on-die image processing unit uses an odometry algorithm to measure displacements in adjacent frames, then sends the data out. The capsule is confined by the GI wall and can only move forward or backward through this tubular track, which shows the direction of travel in Figure 5.2 (a). The side wall camera will measure both *x* and *y* displacement. However,

only displacement in the x-axis will be considered and presented by (D_{mx}), as mentioned in chapter 3. Because the direction of travel is the same as $\vec{H}$. Peristalsis's motion pushes the capsule forward and slightly backward. As a result, positive values from the side wall camera indicate displacement along the $\vec{H}$, and negative values show backward displacement with the direction of $\vec{H}$.

The displacement vector in 3D ($\vec{D}$) is expressed in equation (5.11).

$$\vec{D} = D_{\mathrm{mx}}.\vec{H} \quad (5.11)$$

Then, to calculate the next location (P_{t+1}), the current location (P_t) adds on to $\vec{D}$, as shown in equation (5.12).

$$P_{t+1}(x, y, z) = P_t(x, y, z) + \vec{D} \quad (5.12)$$

For the next iteration, P_t will be stored, and it changes to P_{t+1} to keep updating the loop for the next location. Finally, all locations will be plotted for the estimated 3D trajectory. Figure 5.2(b) illustrates a schematic view of the human GI tract and capsule moving inside the intestine. The $\vec{H}$ is always toward the capsule's motion, and at the same time, displacement information is derived from the side wall camera.

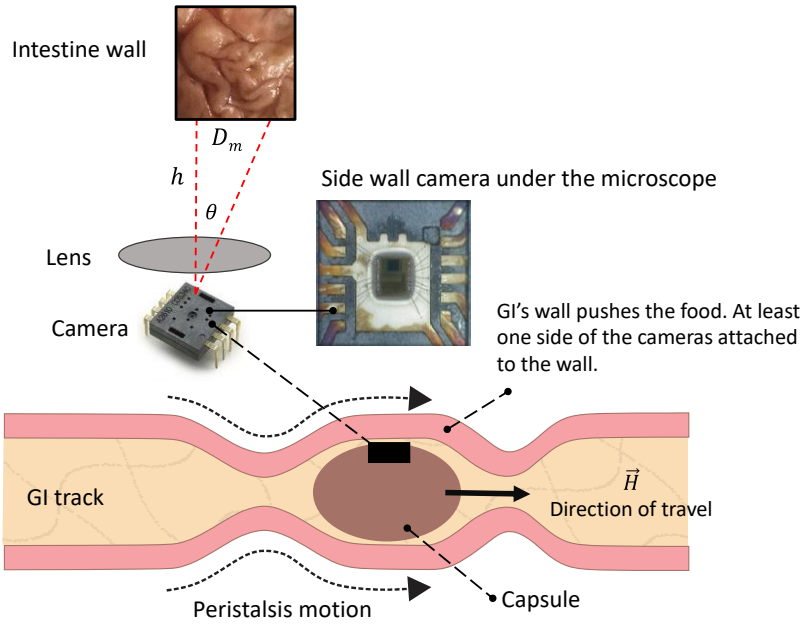

(a)

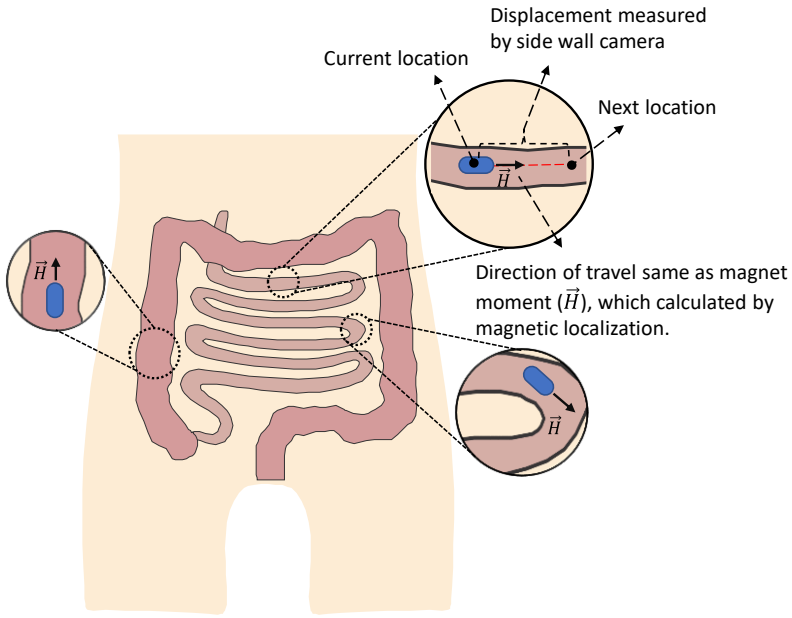

(b)

Figure 5.2 a) Peristalsis motion and side wall camera displacement measurement, b) Human gut and capsule moving inside it.

5.2.3 Fusion Algorithm

The positioning information comes from two different sources: magnetic localization and side wall camera. The environment and magnetometer sensors' noises lead to a jittery estimated position.

However, as magnetic localization measures the absolute position of the capsule from the sensors, the time parameter does not affect the positioning error. Hence, magnetic localization is reliable for extended tracking, which means this method is robust against drifting error but has lower accuracy in the short term. Also, the relative motion of the GI tract has a negative effect on localizing the capsule. Meanwhile, the side wall camera has higher accuracy in the short term, and it can distinguish between the capsule's motion and involuntary motion of the GI tract, but it is susceptible to accumulation of error. A complementary filter with a dynamic mixture coefficient (α) is used to fuse two localization methods. The location derived from magnetic localization is multiplied by α factor, and the estimated location from the side wall camera is multiplied by the $(\alpha - 1)$ factor. The $\vec{D}$ coming from side wall camera localization is fed to the dynamic coefficient controller, and based on the length of this vector which represents the velocity of displacements, α is adjusted from 0.001 to 0.200. Figure 5.3 shows the fusion algorithm with the dynamic coefficient controller.

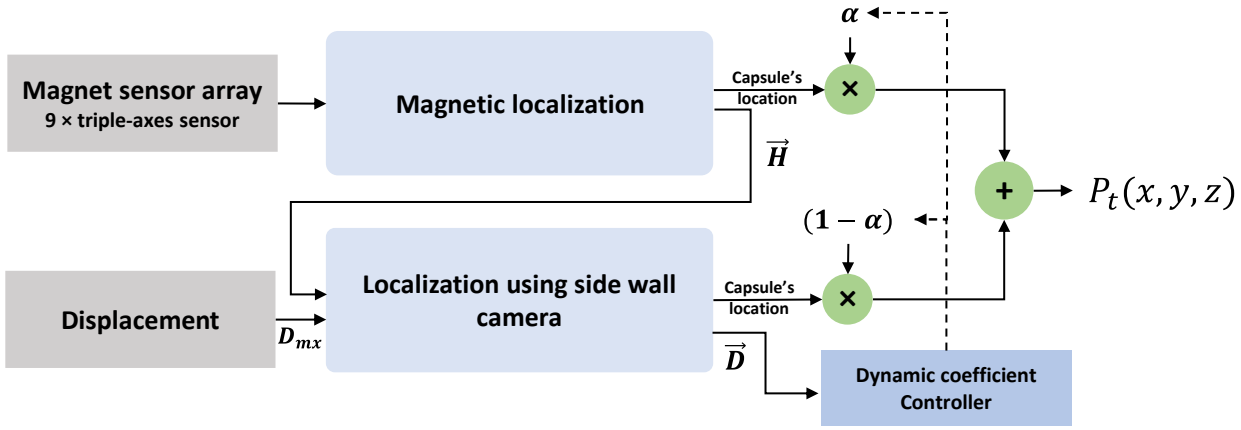

Figure 5.3 Fusion algorithm to mix magnetic and side wall camera localization methods.

5.3 Hardware prototype

5.3.1 Capsule architecture

The capsule consists of a magnet, side wall cameras, a microcontroller (µC), an RF transceiver, and power supply units, as shown in Figure 5.4. In the following sections, we will elaborate on each part. PCBs are designed so each unit will connect to the other using appropriate connectors.

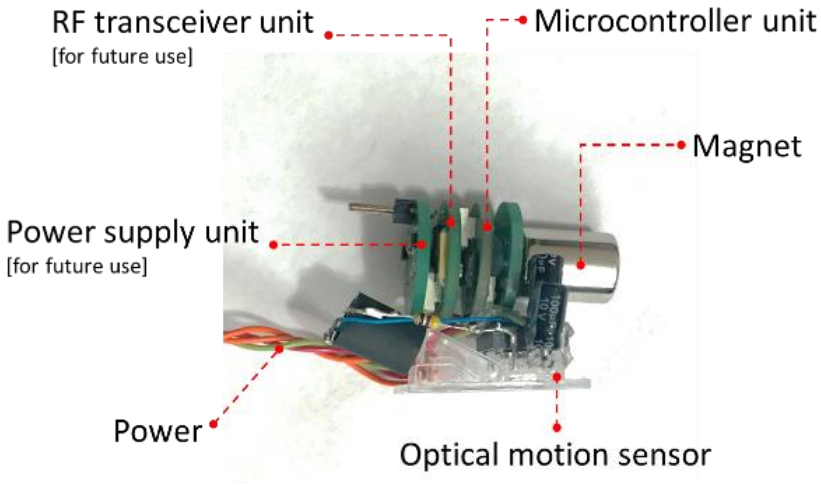

Figure 5.4 Capsule prototype for Method 2

5.3.2 Microcontroller unit

ATmega32U4 is selected for the µC unit due to its smaller footprint. It is connected to the side wall camera using I2C protocol and reads *x* and *y* displacements. Then, it sends the data by a wireless link to the sensor belt outside the body. To reduce the transmission power and increase the battery life, the µC only sends the data when it detects a motion. Figure 5.5 shows the microcontroller unit, which has a diameter of 16 mm.

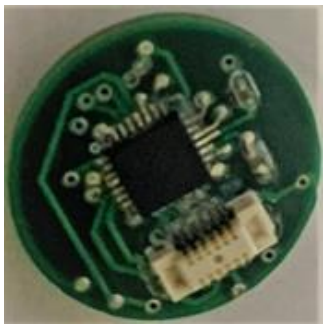

Figure 5.5 Microcontroller unit

5.3.3 Side wall camera

The same technology is used as described in Method 1. To reduce the diameter of the capsule, only one side wall camera is used. However, extending the design to work with four side wall cameras is possible.

5.3.4 Magnet

A Neodymium Iron Boron permanent magnet with dimension of 10 mm × 12 mm is used. Figure 5.6 illustrate the magnet. The magnet is attached to the center of the capsule in the final prototype.

Figure 5.6 Permanent magnet

5.3.5 RF Transceiver unit

Selecting a suitable RF module is essential when it comes to capsule design. The module should be power efficient and operate at a suitable frequency. Higher frequencies are prone to be absorbed by the water, and up to 60% of the human adult body is composed of water—moreover, the RF signals are scattered by human tissues. According to the literature [107], 433 MHz is a suitable frequency for the data transceiver of the ingestible capsules. Figure 5.7 demonstrate the RF transceiver unit, which has 16 mm diameter.

Figure 5.7 RF transceiver unit

5.3.6 Power supply unit

Low dropout regulators (LDO) with miniature footprints are utilized for the power board, each having a rated voltage and current of 3.3 V and 150 mA, respectively. The capsule prototype could

be powered up with any silver oxide or Li-ion battery with a voltage range over 3.7 V. Figure 5.8 shows the PCB of the power supply unit.

Figure 5.8 Power supply unit

5.3.7 Sensor Belt

Magnetometer sensors are spaced 5 cm apart in a 3 by 3 array and formed a belt to fasten around the patient's waist. LIS3MDL is a triple-axis magnetometer with a sensing range of ±1.6 mT with ultra-high precision at a sampling rate lower than 155 Hz. All 9 sensors are connected to an I2C multiplexer controlled by the µC unit. The µC samples magnetometers' data and data received from the capsule every 20 ms. Then, it transfers the data to a PC using a USB cable or stores them in its local memory. The sensor belt is illustrated in Figure 5.9.

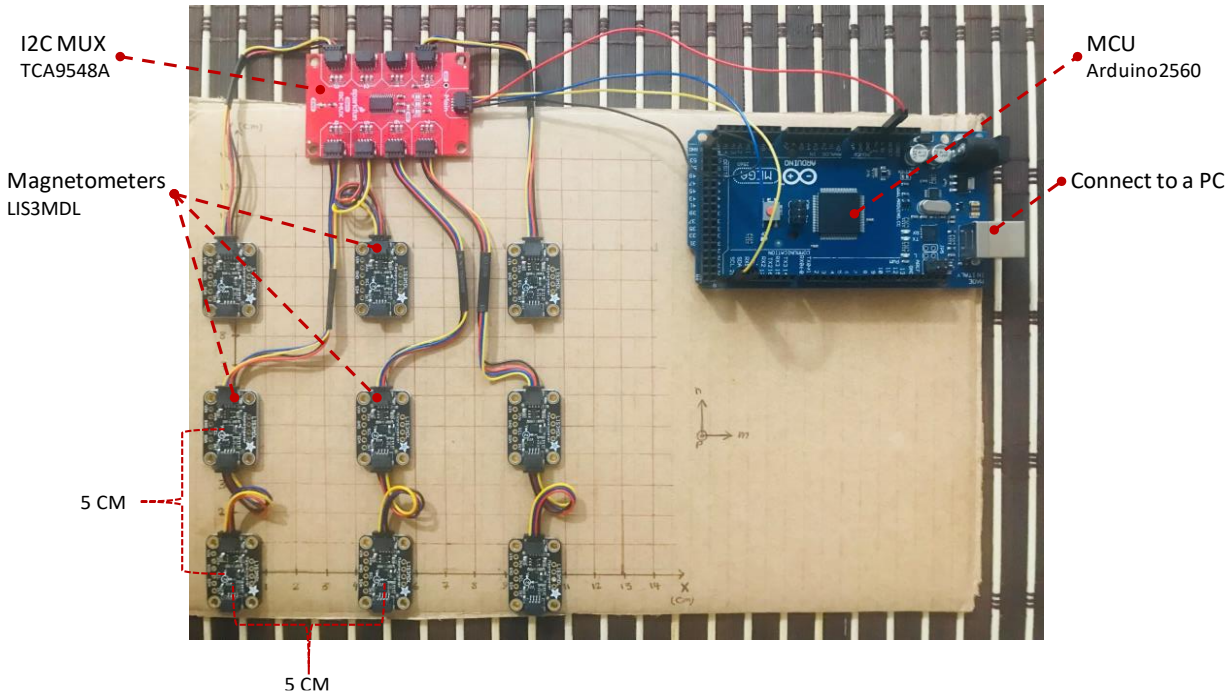

Figure 5.9 Sensor belt consists of 9 triple axes magnetometer sensors, an I2C multiplexer, and an Arduino.

5.4 Experimental setup

For Method 2, the test setup of Method 1 is changed to meet the requirement of the new method. In this method, the localization is based on magnetic localization and the side wall camera. For magnetic localization, a sensor belt must place at a fixed distance against the capsule. In addition, the side wall camera needs a surface to be attached to its surface and becomes functional. As shown in Figure 5.10, a tray is installed on top of the sensor belt at a fixed distance. To perform the experiments, a 5 axes robotic arm is used. The robotic arm moves the capsule in a predefined path programmed on a PC. The robotic arm has a non-ferromagnetic body, and it does not cause interference with magnetic localization. The same PC is used to connect and capture the data from the sensor belt.

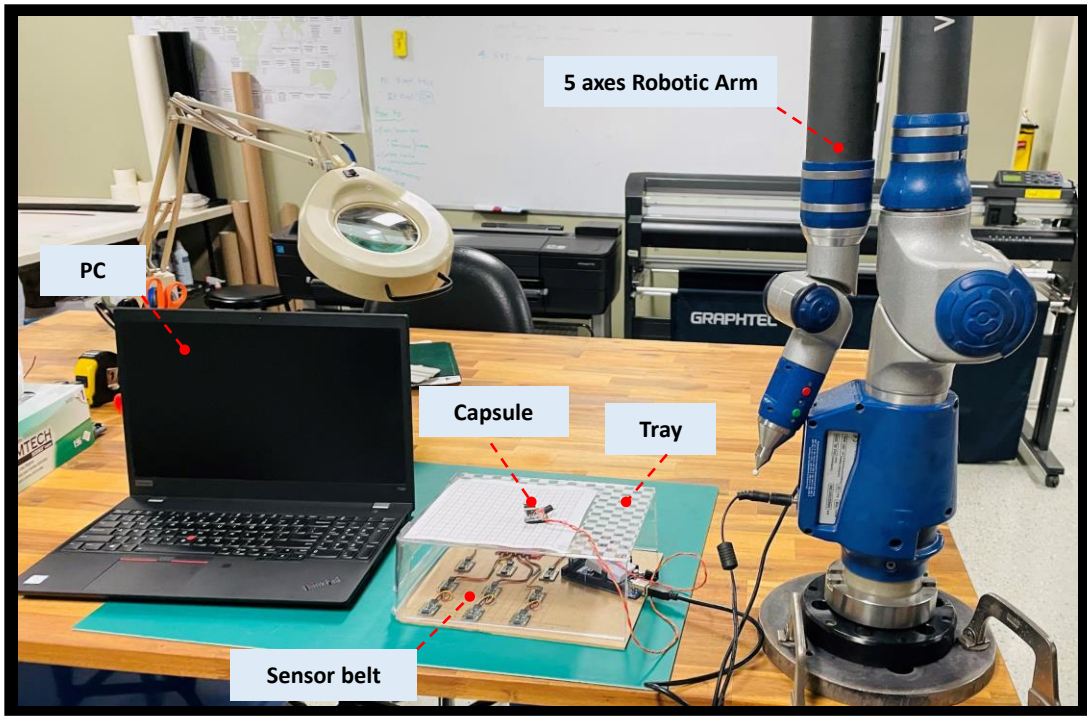

Figure 5.10 Experimental setup for Method 2. A 5 axes robotic arm and a laptop to control the arm.

5.5 Workstation software

A workstation software is prepared to communicate with the sensor belt and perform the localization algorithms. The front end is designed to visualize all plots and results, while the back end processes the data. As shown in Figure 5.11, a graphical user interface (GUI) is designed for the software to interact with the user using python QT. It has both online and offline functionality. In the online mode, the software connects to the sensor belt, captures all data, and plots them on

the screen in real-time. While in the offline mode, the software can read the data from a file and perform the required analysis on them. In the following, we will elaborate on some of the software features. In the Device tab, the user searches for existing serial ports to connect to the sensor belt. The user selects the correct serial port and clicks on the connect button. The connect label turns to blue if the software receives a correct acknowledgment from the sensor belt, and finally, the status changes to "The device is connected". On the next tab, the user calibrates the magnetic sensors and compensates the output data for hard iron and soft iron effects, according to chapter 3.3. A calibration method named "offset equalizer" is provided for testing. To use that, place the sensor belt in a stationary position and keep the sensors away from any external magnetic field. Then, click the offset equalizer button, and it takes 50 samples, measures all input signals from magnetic sensors, and calculates the offset from the zero states. Finally, it creates a table of all biases and adds them to the reading. The next tab is "One-shot tracking", it calculates the position by magnet localization merely for one location. It takes an average of 5 consequence samples from magnetic sensors, performs the PSO algorithm to estimate the capsule's location, and shows them on the screen. This mode shows the exact location of the magnet and the magnetic moment or heading vector on the same plot so that the user can visualize the capsule in 3D space. Every time the user clicks on the run button, the new position will calculate and depict on the screen. To clear the screen the user might use a clear plot button to clear the screen so that the new position will be shown on a new plot. The Data capture tab visualizes the real-time information from the sensors. As shown in Figure 5.11, the raw data from all 9 magnetic sensors and the information received from the side wall camera are available in real time. According to the proposed method, it tracks the capsule. The sensor belt can record all information and act as a stand-alone device. Later, when the capsule is connected to a PC, it transfers all information for further processing. The software reads the data and stores them in a comma-separated values (.csv) format.

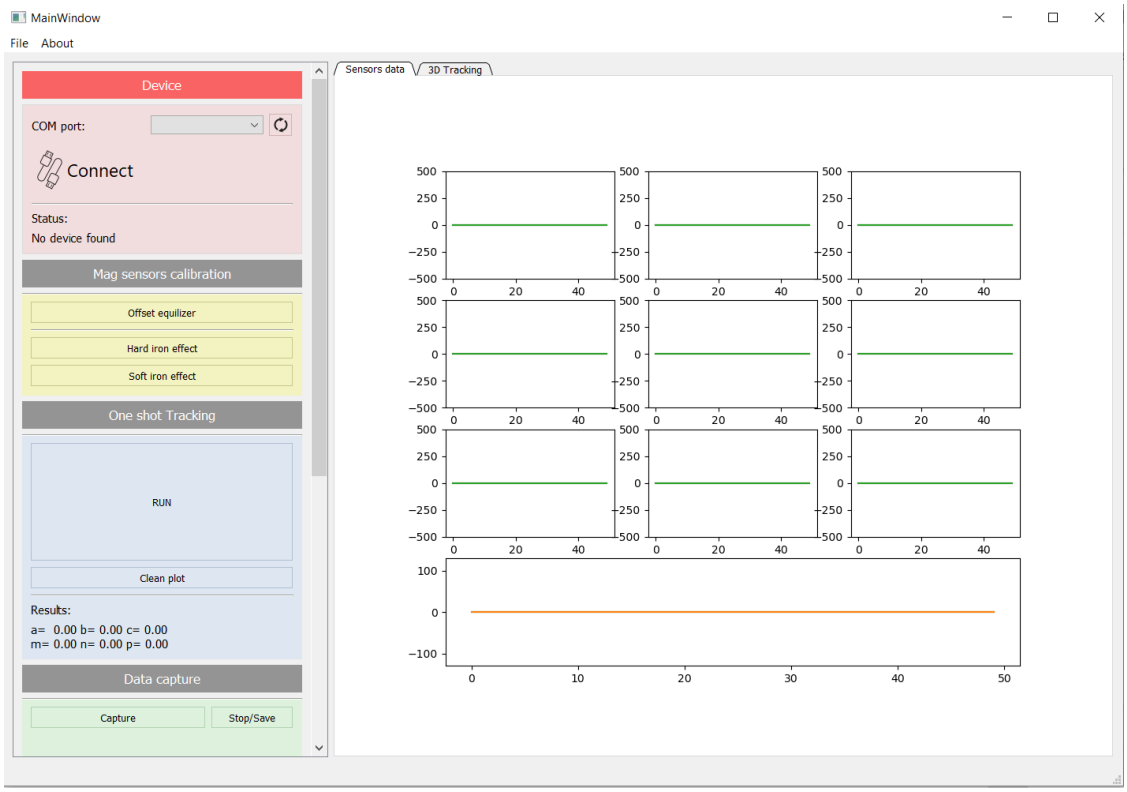

Figure 5.11 Graphical user interface for the software which can connect to the sensor belt and perform localization algorithms

5.5.1 User define variables

The software is designed with a high level of flexibility. Several parameters are accessible to the user to be set. Figure 5.12 shows a brief review of them. "alpha_min" and "alpha_min" is the dynamic range of the α used for the complementary fusion algorithm. "disp_alpha_max" is the displacement in which α reaches its maximum. "dx_coef" is a constant value to convert the side wall camera outputs to the displacement, this parameter is calculated by experiment. The software makes it possible to investigate a different number of sensors and their configuration. The parameter "MAG_SENSOR_NUM" indicates the total number of magnetometers installed in the sensor belt. "OPTIC_SENSOR_NUM" is the number of side wall cameras on the capsule. Using "MAG_SESNOR_COORD," the coordinate of the magnetometers can be specified. "serial_baudrate" is the baud rate of the serial connection between the sensor belt and the PC. "MAX_BUFFER_LEN" indicates the size of the display buffer. A higher value means more samples will be displayed on the real-time plot display. However, it also slows down the PC as it consumes more memory. The optimizer section provides the variables of PSO and LM algorithms. Using "PSO_OPTIONS," parameters c1, c2 and w are accessible. "PSO_PARTICLES" sets the

number of particles to solve the PSO. "PSO_ITERATION" sets the number of iterations. "OPT_BOUNDS" indicates a boundary for the optimizer. Optimizers accept the answers which are inside the bounds. This parameter should be set up based on the magnetometer coordinates. "UPDATE_LOC_INTERVAL" is the refresh interval time for localization in real-time mode. The LM needs less computational power and gives the result faster; however, PSO is precise but requires more time. As the capsule will not move fast and its previous position is adjacent to the current position, "MAX_OPT_CYCLE" provides the number of performing LM algorithms before using the PSO algorithm. The "OPT_AVG_SAMPLE_NUM" parameter defines the number of samples that should be averaged for each estimated position.

```
# ---------------------------- Fusion ------------------------------
alpha_min = 0.01
alpha_max = 0.1
disp_alpha_max = 70
dx_coef = 0.0035

# ---------------------------- Sensors ------------------------------
MAG_SENSOR_NUM = 9
OPTIC_SENSOR_NUM = 1
MAG_SESNOR_COORD = [(10, 10, 0),
                    (10, 5, 0),
                    (10, 0, 0),
                    (5, 10, 0),
                    (5, 5, 0),
                    (5, 0, 0),
                    (0, 10, 0),
                    (0, 5, 0),
                    (0, 0, 0)]
serial_baudrate = 115200
MAX_BUFFER_LEN = 50

# ---------------------------- Optimizer ----------------------------
PSO_OPTIONS = {"c1": 0.5, "c2": 0.3, "w": 0.9}
PSO_PARTICLES = 150
PSO_ITERATION = 150
OPT_BOUNDS = ([-3, -3, -3, -1, -1, -1], [15, 15, 15, 1, 1, 1])
UPDATE_LOC_INTERVAL = 100
MAX_OPT_CYCLE = 50
OPT_AVG_SAMPLE_NUM = 5
```

Figure 5.12 User defines a variable for the software

5.5.2 Data structure

Similarly, the software saves the raw data of magnetometers and side wall cameras in an excel format. As shown in Figure 5.13, each row indicates one sample. Every three columns are dedicated to a magnetometer where the measured data for axes *x*, *y*, and *z* are stored. The last two

columns, AB and AC, record the displacements measured by the side wall camera in directions *x* and *y*, respectively. Unlike method 1, magnetic localization does not require to capture the precise sample's time. Hence, it was no longer needed to store the internal timer of the microcontroller. The software has the flexibility to set up various configurations of sensors, so the number of columns in the excel file depends on the software configuration. The magnetometer output data have a float value between -100 to 100 depending on its resolution parameter. At the same time, the side wall camera has an integer value between -127 to 127.

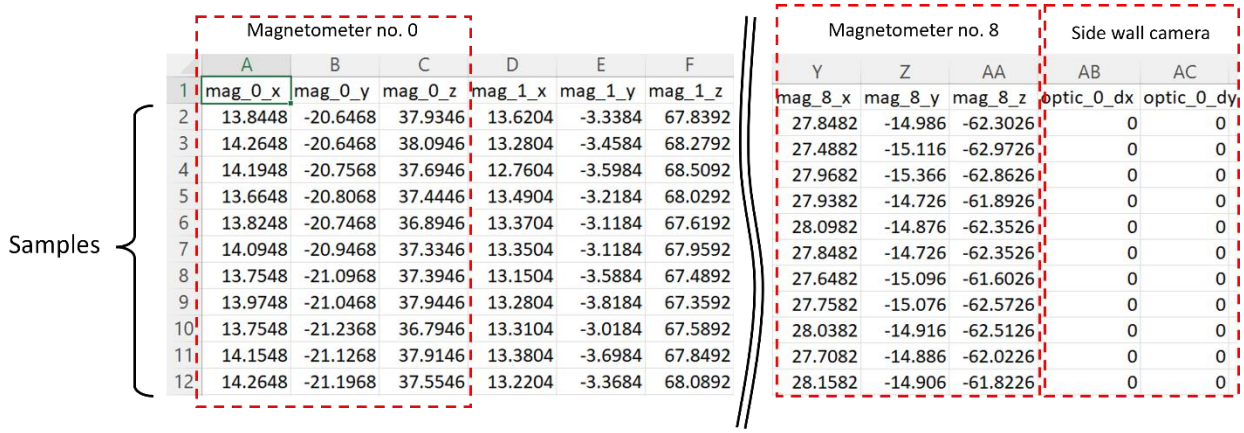

	A	B	C	D	E	F	Y	Z	AA	AB	AC
1	mag_0_x	mag_0_y	mag_0_z	mag_1_x	mag_1_y	mag_1_z	mag_8_x	mag_8_y	mag_8_z	optic_0_dx	optic_0_dy
2	13.8448	-20.6468	37.9346	13.6204	-3.3384	67.8392	27.8482	-14.986	-62.3026	0	0
3	14.2648	-20.6468	38.0946	13.2804	-3.4584	68.2792	27.4882	-15.116	-62.9726	0	0
4	14.1948	-20.7568	37.6946	12.7604	-3.5984	68.5092	27.9682	-15.366	-62.8626	0	0
5	13.6648	-20.8068	37.4446	13.4904	-3.2184	68.0292	27.9382	-14.726	-61.8926	0	0
6	13.8248	-20.7468	36.8946	13.3704	-3.1184	67.6192	28.0982	-14.876	-62.3526	0	0
7	14.0948	-20.9468	37.3346	13.3504	-3.1184	67.9592	27.8482	-14.726	-62.3526	0	0
8	13.7548	-21.0968	37.3946	13.1504	-3.5884	67.4892	27.6482	-15.096	-61.6026	0	0
9	13.9748	-21.0468	37.9446	13.2804	-3.8184	67.3592	27.7582	-15.076	-62.5726	0	0
10	13.7548	-21.2368	36.7946	13.3104	-3.0184	67.5892	28.0382	-14.916	-62.5126	0	0
11	14.1548	-21.1268	37.9146	13.3804	-3.6984	67.8492	27.7082	-14.886	-62.0226	0	0
12	14.2648	-21.1968	37.5546	13.2204	-3.3684	68.0892	28.1582	-14.906	-61.8226	0	0

Figure 5.13 Raw data from the lab capsule prototype

5.6 Cost breakdown

Table 5.1 shows the breakdown of the material costs of our capsule prototype. The miscellaneous cost in Table 5.1 includes packaging and fabrication costs.

Table 5.1 Cost breakdown of the proposed capsule prototype.

Component	Model/Specification	Cost ($USD)
Side wall camera		10
Magnet	Magnet Neodymium Iron Boron	3
Microcontroller	ATMEGA328P-MMHR	5
Transceiver	RFM96W	20
Antenna		2
PCB		10
Miscellaneous		40
Total Cost		90

Chapter 6

Results and discussion for Method 2

Several experiments are performed in this section, and their results are compared with magnetic localization [84] and Method 1 [38]. RF-based and image-based methods have lower localization accuracy and do not provide acceptable positioning errors. So, we do not consider them for comparison study.

6.1 Optimizing the alpha parameter

Several experiments have been performed to select the optimum α. In the following, we have demonstrated a couple of examples. In the first step, let us disable the dynamic coefficient controller. Hence, $\alpha_{min} = \alpha_{max}$. Two extreme cases are 1) $\alpha_{min} = \alpha_{max} = 1$, leading to localization solely based on the magnetic method. 2) $\alpha_{min} = \alpha_{max} = 0$, which leads to localization solely based on the side wall camera method.

Several experiments in the manuscript show the difference between magnetic localization and odometry. In the following we will test several $0 < \alpha_{min} = \alpha_{max} = \alpha < 1$.

Figure 6.1 illustrates several α tests. Figure 6.1(a) the α is set to 0.001, and as a result, it could testify that the MagnetOFuse tends to Method 1, which causes the offset issue of the side wall camera. In Figure 6.1(b), the α is set to 0.01, which means that 1% of the estimated track comes from magnetic localization and 99% comes from side wall cameras. Figure 6.1(e) shows the results of α equal to 0.7. In this case, the estimated track gets its behavior mostly from magnetic localization, which involves jittery and noisy results. However, the results of α equal to 0.2 in Figure 6.1(c) have lower positioning error with smooth tracking.

On the next experiments the $0 < \alpha_{min} \neq \alpha_{max} < 1$ is investigated. The α coefficient will be determined by the dynamic coefficient controller, which uses the size of $\vec{D}$ to adjust the α on the given range. As shown in Figure 6.2, α_{min} does not significantly affect the results of a normal motion. However, the dynamic coefficient controller shows its behavior in relative motions.

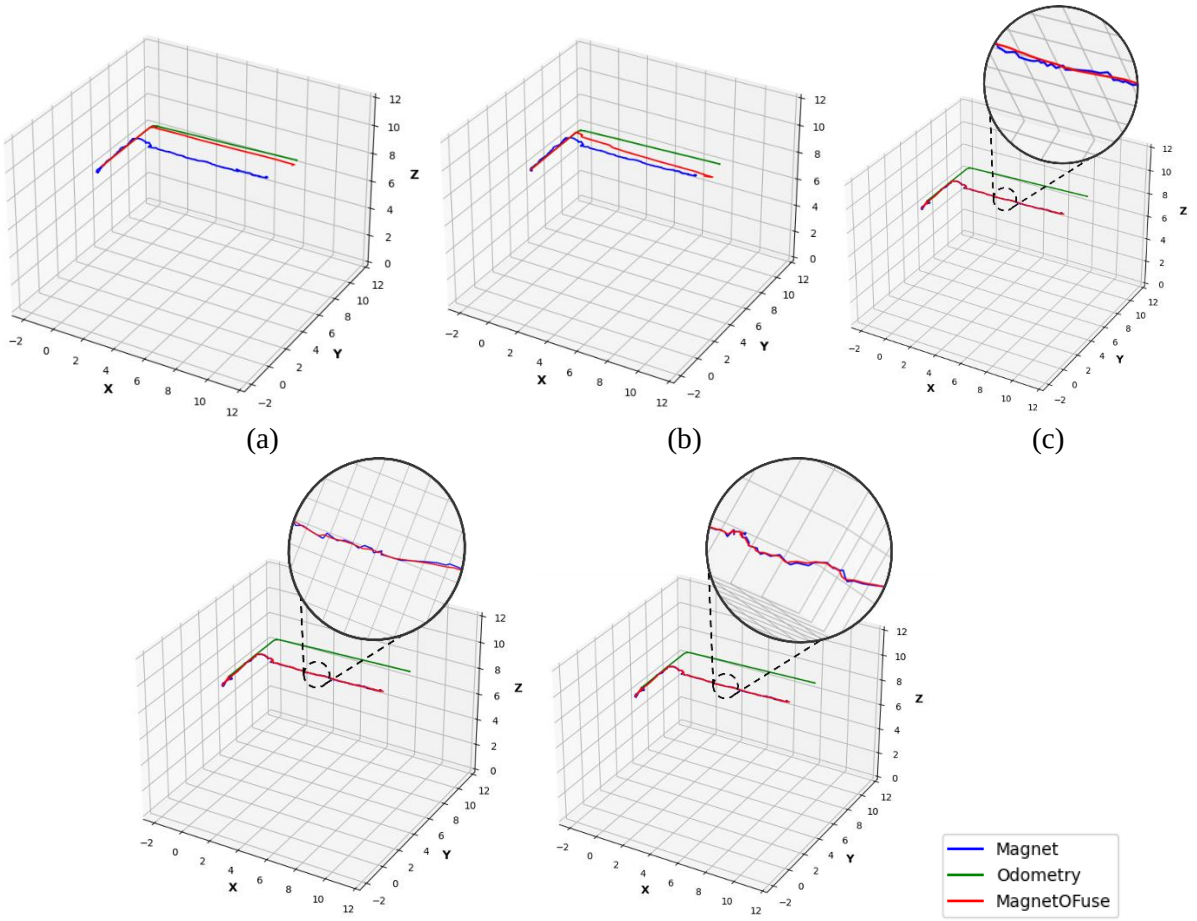

Figure 6.1 Investigating the effect of α while the dynamic coefficient controller is disabled ($\alpha_{min} = \alpha_{max} = \alpha$), a) $\alpha = 0.001$, b) $\alpha = 0.01$, c) $\alpha = 0.2$, d) $\alpha = 0.5$, e) $\alpha = 0.7$

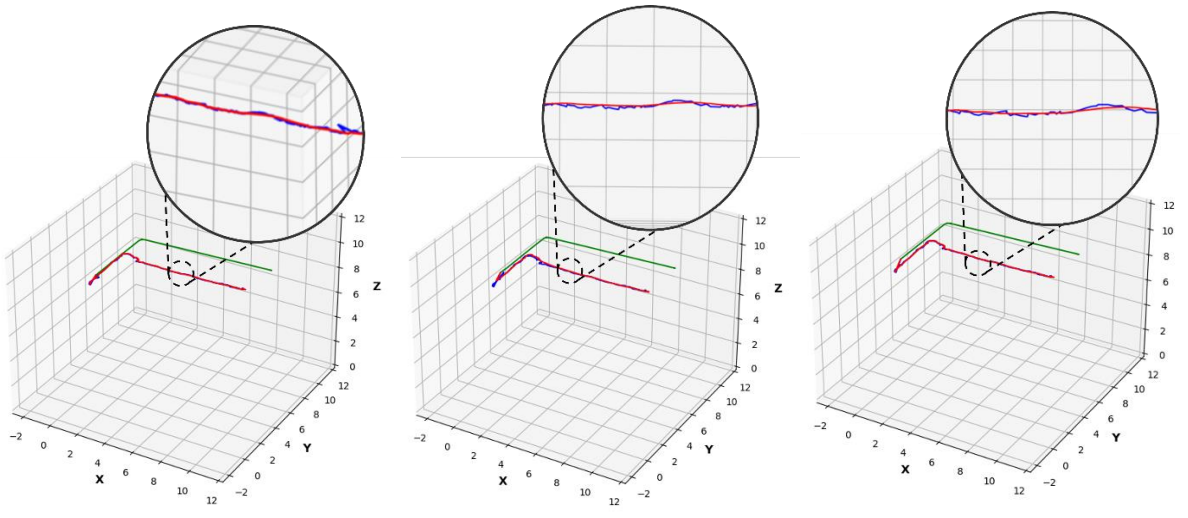

Figure 6.2 Investigating the effect of α on normal motion, a) $\alpha_{min} = 0.001$ and $\alpha_{max} = 0.2$, b) $\alpha_{min} = 0.01$ and $\alpha_{max} = 0.2$, c) $\alpha_{min} = 0.1$ and $\alpha_{max} = 0.2$

Figure 6.3 illustrates the effect of α_{min} in a relative motion. Two test cases are performed with different α_{min}. Smaller α_{min} results higher rejection rate of the relative motion. However, considering the capsule has a relative motion and seats in a new position, if α_{min}=0, then the algorithm will fail to follow the capsule's position (it ignores all relative motions). Hence, α_{min}>0 makes it possible to sit in the stationary position after some iterations.

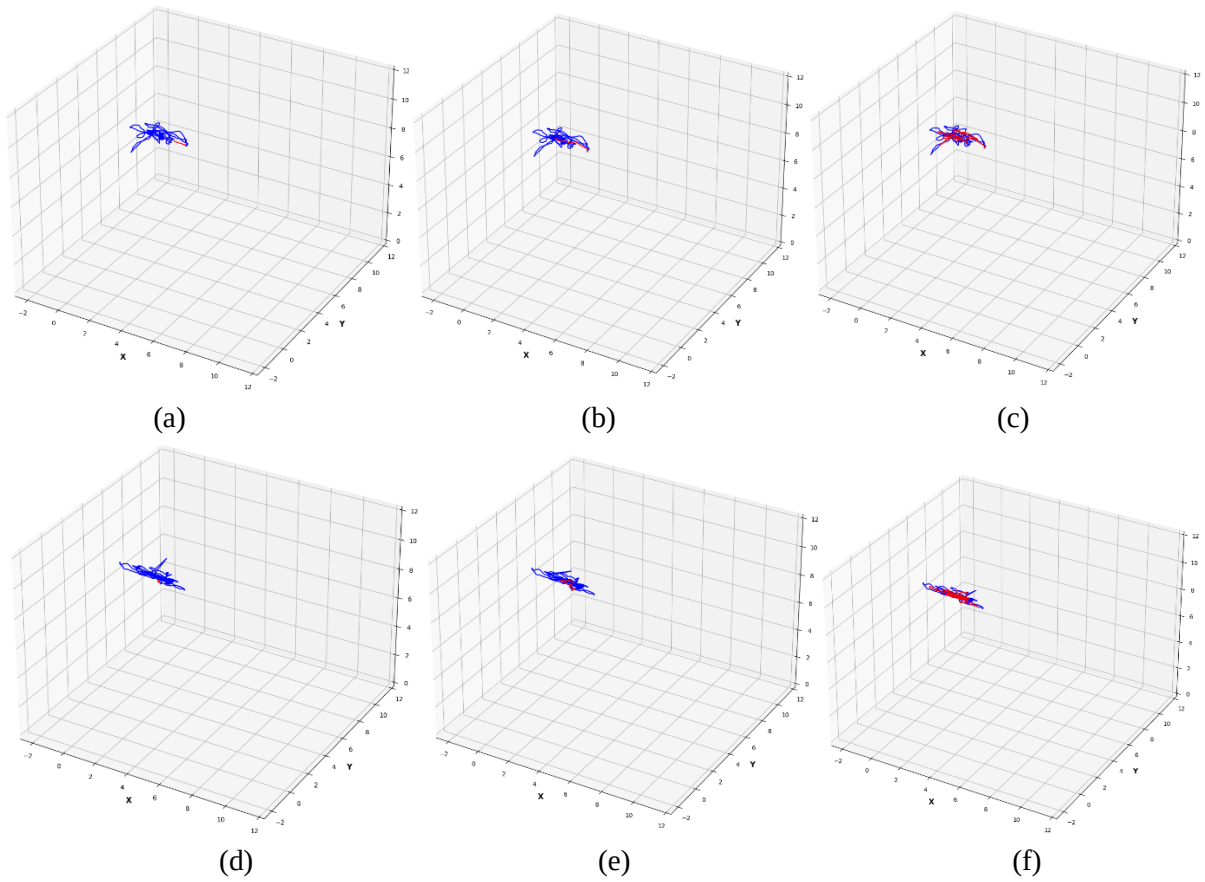

(a) (b) (c)

(d) (e) (f)

Figure 6.3 Investigating the effect of α on relative motion, a) Test case 1. α_{min} = 0.001, α_{max} = 0.2, b) Test case 1. α_{min} = 0.01, α_{max} = 0.2, c) Test case 1. α_{min} = 0.1, α_{max} = 0.2, d) Test case 2. α_{min} = 0.001, α_{max} = 0.2, e) Test case 2. α_{min} = 0.01, α_{max} = 0.2, f) Test case 2. α_{min} = 0.1, α_{max} = 0.2

6.2 Stability experiments

The stability experiment is initially performed to compare the proposed method with some available techniques. In this experiment, the capsule is placed at a stationary position, and the algorithm localizes the capsule for 60 s. As illustrated in Figure 6.4, the blue line shows the magnetic localization. The data is quite noisy because several noise sources are involved in magnetic localization, such as environmental conditions, sensors' noise, and optimization

algorithms, leading to unstable and jittery results with average and standard deviations of 1.82 and 0.86 mm, respectively. Method 1 showed in green. The side wall camera in this method does not detect any motion, so the positioning error remains constant, and the initial position of the capsule determines it. The MagnetOFuse is shown with red color, and it has lower position error with average and standard deviation of 0.84 and 0.25 mm, respectively.

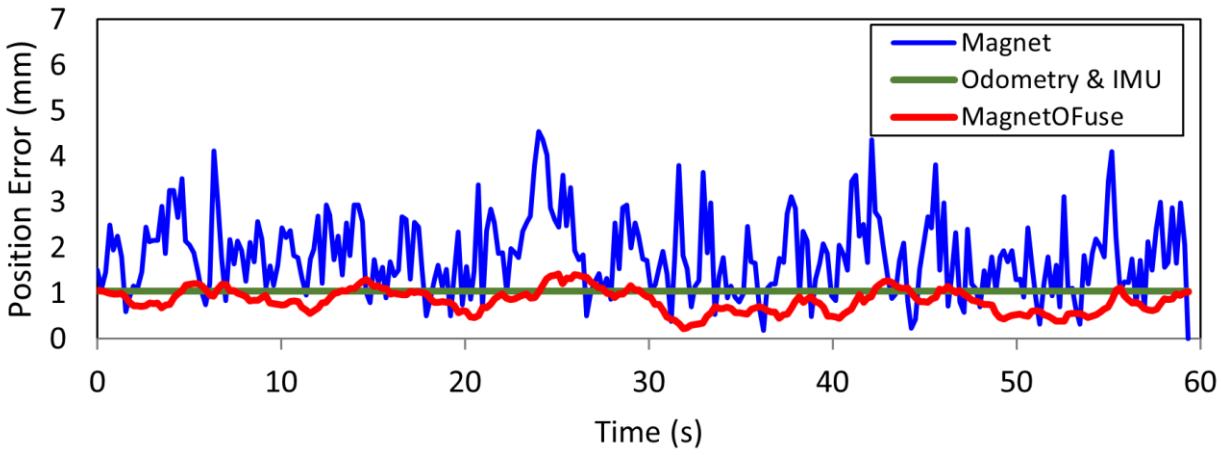

Figure 6.4 Position error in stationary localization experiment.

6.3 Localization experiments

In the second experiment, a robotic arm moves the capsule in a predefined track known as the ground truth. Results for some trajectories are shown in Figure 6.5. The black line shows the ground truth, the blue line shows the magnetic localization, and the red line shows the MagnetOFuse. It can be observed that magnetic localization tends to have higher localization noises. Hence, the estimated track jumps to the wrong location. Meanwhile, the MagnetOFuse has a smoother path. Figure 6.5 (a) shows that the Odometry localization diverges from the ground truth. Since this method has no feedback mechanism, a small error accumulates, and the positioning error increases over time. Figure 6.5 (b) shows that although the capsule moves in a straight line, the magnetic localization has errors due to the ambient magnetic noises. However, MagnetOFuse has lower jittering and positioning errors.

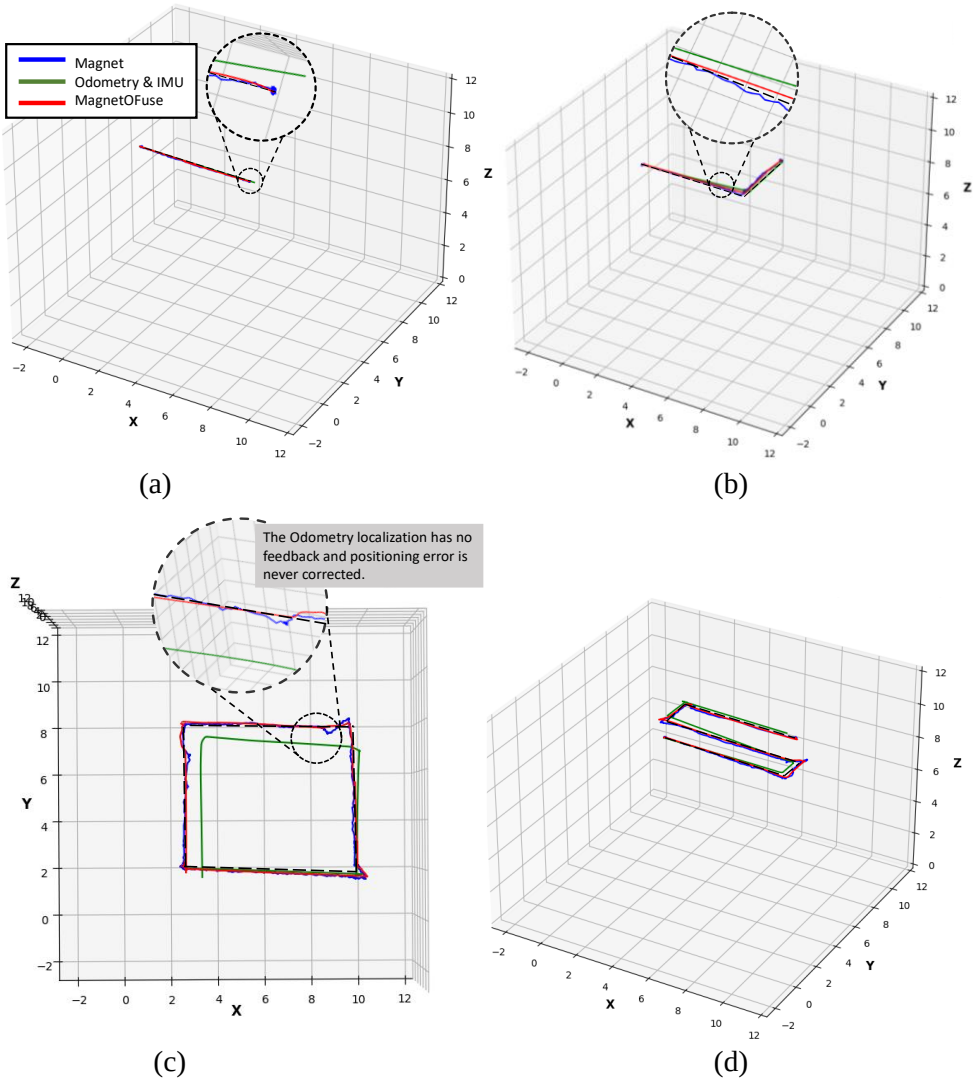

Figure 6.5 Path tracking results of Magnetic, Odometry & IMUand MagnetOFuse localization methods

Figure 6.6 illustrates the position error of the test trajectories. For example, in test 1, magnetic localization has maximum and minimum positioning errors of 7 mm and 1 mm, respectively. The odometry has an average positioning error of 4.2 mm. Finally, MagnetOFuse has maximum and minimum positioning errors of 4 mm and 1 mm, respectively. Considering all experiments, the average positioning error for magnetic localization and odometry is about 5.5 mm and 8.2 mm, respectively, while it is 3.5 mm for MagnetOFuse.

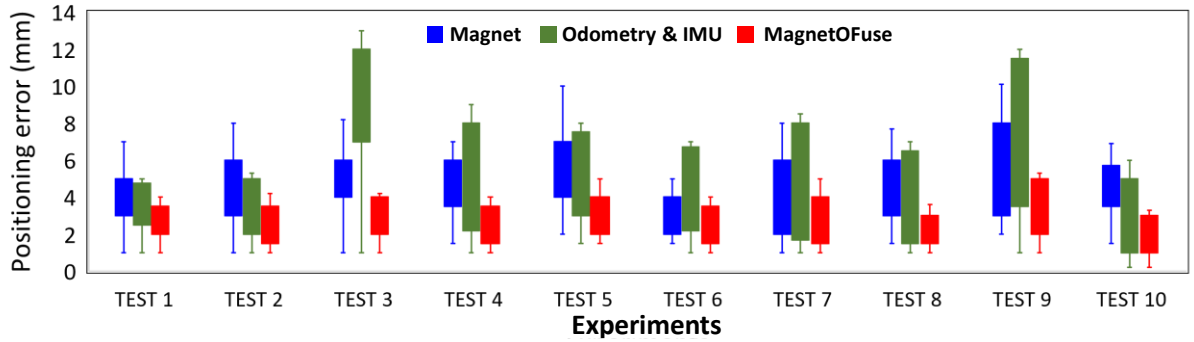

Figure 6.6 The mean position error for magnet, odometry & IMU, and MagnetOFuse test trajectories.

6.4 Relative motions

As stated earlier, the relative motions cause significant error accumulation in all the existing localization methods. Two relative motions can be defined as: I) the GI tract's involuntary motion and II) the relative motion between the sensor belt and the abdomen.

First, the GI system has the freedom to move inside the body. At the same time, the capsule might be stationary with respect to the GI tract, which causes some localization errors. Magnetic localization measures the actual location of the capsule where the reference point is the sensor belt; in contrast, side wall camera localization measures the translations working on the capsule. During the GI tract's motion, $\vec{D}$ is zero, which leads to α becoming α_{min}. Thus, localization relies heavily on side wall camera data. However, if the GI tract returns to its initial position, all the relative motions will be ignored as soon as the capsule starts to move. Otherwise, based on the size of $\vec{D}$, α will be modified to adjust the estimated location. The capsule is placed on top of an intestine for this experiment to simulate the GI tract's motion. Both the intestine and capsule are manually displaced. In this case, the capsule still has a relatively stationary position while the intestine is moving. Then, the capsule starts to move. As shown in Figure 6.7 (a), the GI tract has changed its position, and the displacements are reflected in magnetic localization; however, the GI tract reverts to its previous state, which means that the relative motion is ignored for odometry and MagnetOFuse. Figure 6.7 (b) shows another experiment in which the GI tract's relative motion does not end at the initial position. In this case, the relative motion is captured by magnetic localization, showing a 4 cm upward jump followed by a 2 cm downward jump. Odometry does not capture any motion because the side wall camera was stationary with respect to the GI tract's wall. However, the MagnetOFuse only sees the 2 cm jump while ignoring the relative motions.

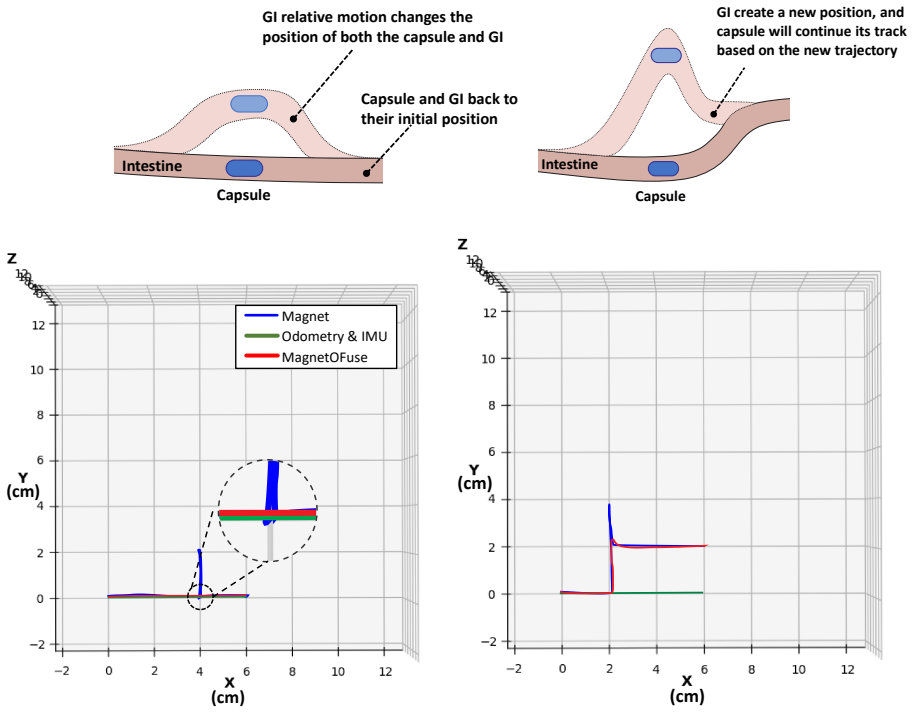

(a) (b)

Figure 6.7 GI involuntary motion, a) GI returns to its initial position, and b) GI is in a new position after its motion.

The relative movement between the sensor belt and the patient's abdomen is another source of error. In this experiment, the capsule and intestine have a stationary position. However, the sensor belt is moving, as shown in Figure 6.8 (a). The blue lines show the magnetic localization, and the red lines show the MagnetOFuse method. A small portion of the plot is magnified to have a better view. The magnetic localization measures the absolute position of the capsule with respect to the sensor belt. Therefore, it captures all motion. On the other hand, the MagnetOFuse ignores a significant portion of the relative motions because the side wall cameras do not measure any motions during relative motions. The results show that this motion leads to a considerable positioning error for magnetic localization. In contrast, the MagnetOFuse can reduce the positioning error by about 70%. Figure 6.8 (b) and (c) illustrate two random relative motions of the sensor belt.

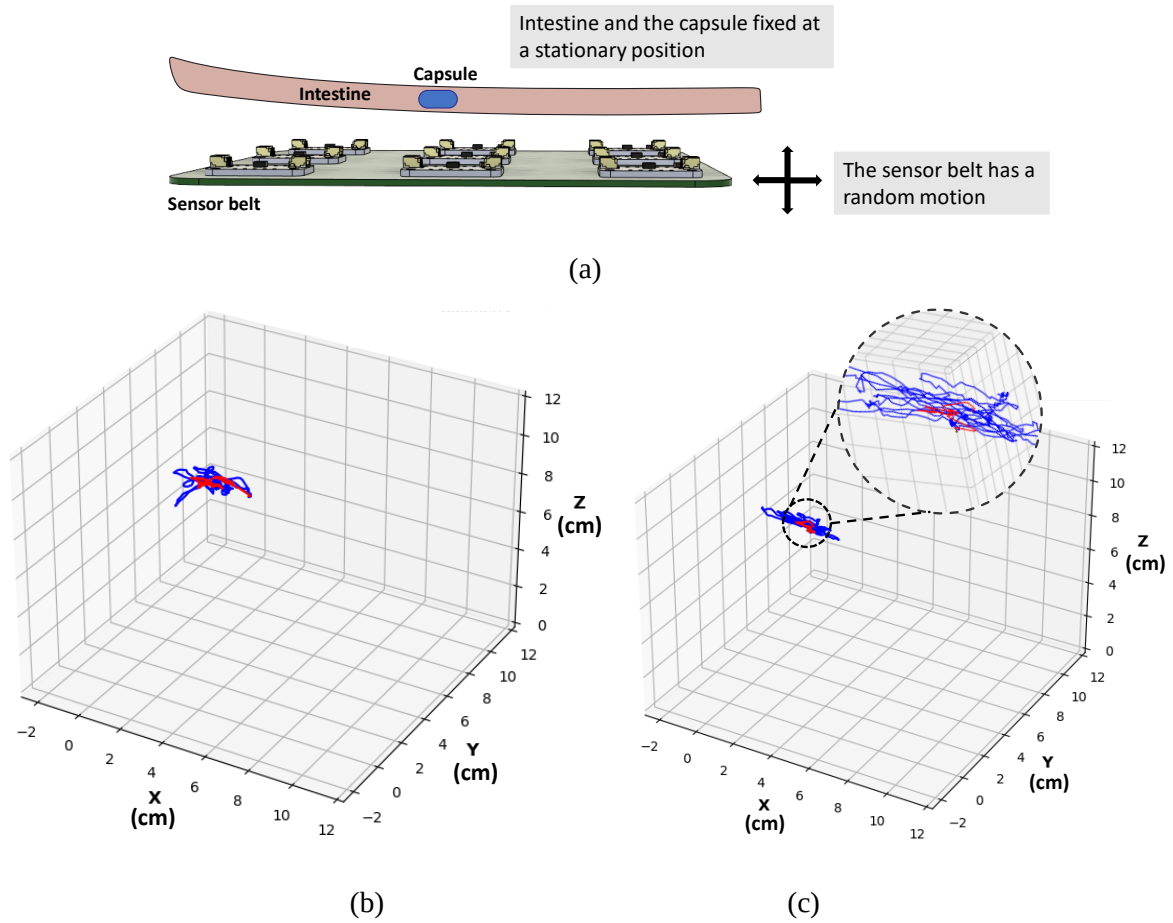

Figure 6.8 Relative motion between the sensor belt and the abdomen. The blue lines show the magnetic localization, and the red lines show the MagnetOFuse method.

6.5 Surge motions

Surge motion is a kind of sudden movement or a fast displacement at a short time, which the capsule might experience in the body due to the peristalsis motion. The sensor belt reads magnetometer data at T_s of 20 ms. To measure the surge motions, T_s should be as small as possible. However, shorter T_s leads to higher noise level and errors in reading the magnetometers' data. Hence, magnetic localization cannot capture surge motion. On the other hand, the side wall camera can detect every tiny displacement of the capsule and measure the surge motions. In addition, the integrated processing unit inside the side wall camera is independent of the T_s and reports total displacements over T_s. Hence, accuracy remains the same. For this experiment, the robotic arm moves the capsule at short distances with different movement speeds. Table 6.1 shows the experiment results for MagnetOFuse and localization solely based on the magnetic method.

At lower velocities, the fusion algorithm has a higher gain for the side wall camera localization method because this method has higher short-term accuracy. For example, at 0.5 cm/s, the α is equal to 0.001. As velocity increases, the α rises to 0.2, which means the magnetic localization contributes the most to track, and it leads to compensate for the drift issue of side wall cameras over time. Results show that the magnetic localization has almost the same positioning error regardless of the capsule's displacement velocity, which is about 5.5 mm. Meanwhile, for MagnetOFuse, the positioning error at lower speeds is around 1.2 mm, and at higher speeds, the positioning error rises to 3.5 mm.

Table 6.1 Effect of capsule velocity over positioning error

Velocity (cm/s)	Average positioning error (mm)	
	Magnet	MagnetOFuse
0.5	3.8	1.2
1	4.8	1.2
2	5.2	1.5
3	5.5	2.5
4	5.5	2.7
5	5.5	3.4
6	5.5	3.5
7	5.5	3.5

6.6 Pseudo-body effect

In a real-world scenario, the capsule enters the digestive system and is surrounded by human tissues, bones, etc. Hence, it is essential to investigate the effect of the body on localization. For this experiment, the space between the capsule and the sensor belt was filled with an inhomogeneous material, including ground beef and water. Figure 6.9 (a) shows the test setup. The grounded beef packs are inserted between the sensor belt and capsule plane. Then, the robotic arm moves the capsule in a predefined trajectory. Figure 6.9 (b) illustrates the positioning error over time while the filling material changes. Results show that the positioning error for grounded beef, water, and air are almost similar. Hence, the inhomogeneous environment of the human body will

not affect the positioning error. The non-ferromagnetic materials do not affect magnetic localization. Furthermore, the side wall camera method is independent of filling materials.

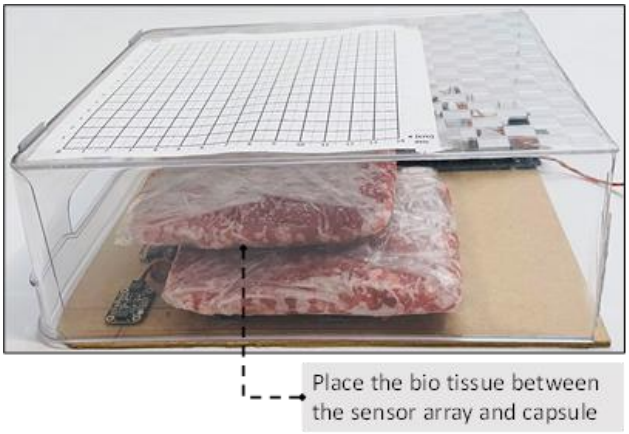

(a)

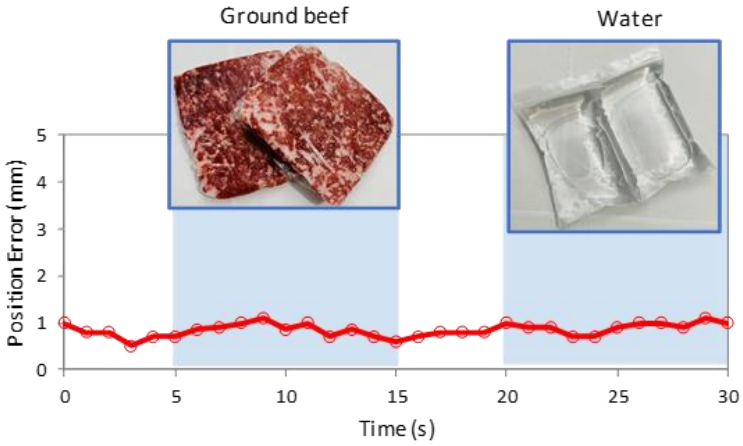

(b)

Figure 6.9 a) Test setup for placing the bio-tissue, b) Effect of bio-tissue in position tracking

6.7 Power consumption

The capsule is designed with a small and limited battery size. The WCE process takes about 8 hours; hence, batteries should power up the device for the entire process. The data shows that the capsule consumes 29.83 mW. Therefore, the capsule requires a battery with 72.32 mAh capacity to work properly for 8 hours of operation. The sensor belt consumes 260.14 mW and uses a battery pack attached to the belt. It should be noted that power consumption could be significantly reduced with the aim of an IC in commercial products.

Chapter 7

Summary and conclusion

7.1 Summary

The work done in this thesis can be summarized as follows:

- Based on the unique properties of the GI tract, two methods are developed to track the WCE inside the GI system. These methods take advantage of the new use of side wall cameras, IMU sensor, and magnetic localization followed by optimization and fusion algorithms.
- To fuse IMU sensor information with the side wall camera to distinguish between the capsule's motion and the involuntary motion of the GI tract inside the body coordinate.
- To fuse magnetic localization information with a side wall camera to increase the tracking accuracy and distinguish between the capsule's motion and involuntary motion of the GI tract inside the body coordinate.
- To propose methods that consider the GI tract's involuntary and relative motion.
- To develop a prototype consisting of electronic capsules, a data logger, sensor belt.
- To develop a workstation software that can capture the data, conduct localization algorithms, and visualize the 3D tracking results for the user.
- To investigate the effect of pseudo-body on proposed localization methods.
- To develop a robotic arm test setup to simulate the GI motions, such as peristalsis, relative, surge, linear, etc.
- To perform ex-vivo experiments in the pig's intestine and validate the performance of the proposed localization algorithms.

7.2 Conclusion

7.2.1 Method 1

In chapter 3, we discussed Method 1 for WCE localization. This method is developed based on the tubular shape of the GI tract, which confines the capsule to move through this path. Method 1 tracks the capsule in a 3D space by knowing the direction and size of the capsule's displacement. The method uses an IMU sensor and four side wall cameras. The IMU sensor has a gyroscope, accelerometer, and magnetometer. The IMU data are fused with the aim of the AHRS algorithm to estimate the capsule's orientation. The side wall cameras use 18×18 pixels CCD and a processing unit in the same IC to measure the displacements. The four-camera topology ensures that at least one of them will be in touch with the GI wall to measure the displacement. Finally, the fusion algorithm combines orientation and displacement to generate a 3D trajectory. The proposed capsule has no external reference point. Therefore, compared with other capsule localization methods, this system has many robust features, including no interference from the patient's movement or GI involuntary movements. The RF and Magnetic-based localization methods have lower positioning errors compared to Method 1. However, these methods require a static reference antenna surrounding the patient body. Radiation and ultrasound-based methods are not feasible as they need hospital facilities and expose patients to unwanted radiation. Image-based tracking methods are unreliable for complete localization due to the lack of fixed markers inside the GI tract. Furthermore, all the above methods fail to consider the involuntary motion of the small bowel, which leads to localization errors.

The proposed method has several significant advantages. Hospital facilities and technicians are not required in this method, and it does not confine patient movement. Most importantly, the involuntary motions of the GI tract will not interfere with the localization, so the capsule’s actual displacement can be projected. Side wall cameras reject involuntary motions and eliminate the GI tract motion inside the body. As described in chapter 2, accuracy alone is not the ultimate factor for comparing different methods. Instead, several factors contribute to select the suitable method, such as considering GI involuntary motion, patient's comfort, need for a fixed external reference point, hospital facility, etc. Finally, the proposed method is experimentally verified in laboratory conditions. Table 7.1 provides a list of intra-body capsule localization methods and compares them based on the accuracy (how much the estimated measurement is close to the ground truth), extra hardware or weight inside the capsule, patient's comfort (i.e., patients' mobility during the period

of diagnosis), fixed reference point (patient's outside movement vs. capsule's inside movement), interference of transmitted signal with other sources, involuntary GI motion, and prototype validation (in vitro or in vivo).

7.2.2 Method 2

Method 1 has high accuracy in the short term. But, due to the accumulation of errors from side wall cameras, the estimated trajectory tends to drift over time. In chapter 5, Method 2 was developed to resolve the drifting issue while keeping the same positioning error. This hybrid method utilizes magnetic localization and side wall camera techniques to track the capsule. Magnetic localization provides the global position, while the side wall camera measures the precise motions. This hybrid method can distinguish between the capsule's motions and the relative motion of the GI system. Localization techniques that solely rely on magnetic fields measure the absolute position of the magnet with respect to the sensor belt, which results in a miss interpretation of the GI tract relative motions and the capsule's motions; hence, it increases the positioning error. On the other hand, side wall camera localization methods are based on measuring the capsule's motion, so the GI tract relative motions do not interfere with the localization. However, they suffer from the accumulation of errors. This work combines both methods to improve tracking accuracy. Several experiments have been conducted to evaluate the performance of the proposed method. The results showed that Method 2 has an average of 0.84 mm, and 3.5 mm for tracking a stationary and a moving capsule, respectively. According to the experiments, MagnetOFuse can detect surge motions up to 7 mm/s and slow motions less than 0.5 mm/s, with a positioning error of 1.2 mm. Method 2 has a lower positioning error, and it can distinguish the capsule's motion from the GI tract's relative motions. Table 7.2 shows a comparison between this work and some promising methods. This table demonstrates that the proposed method is suitable for localizing the WCE inside the body, and it paves the path for further investigation.

Table 7.1 Comparing Method 1 with competitive WCE localization methods

Localization Method		Accuracy	Additional hardware inside the capsule	Additional hardware for patients (Patient's comfort)	Static position for reference	Interference	Considering GI involuntary motion	In vitro or in vivo validation	Ref
RF	ToA, Received Signal Strength Indicator (RSSI)	0.2 cm	NO – all necessary modules for RF localization are already implemented in capsules.	The patients must carry extra hardware (antenna array mounted on a cube). Limits the patient's mobility significantly.	YES- An array of antennas or a belt is required. Antennas must have fixed positions.	Different tissues and muscles lead to inhomogeneous path loss and huge errors in localization.	Involuntary motion makes GI organs move inside the body coordinate while the outside antenna cube is stationary. Results in significant error in localization since the RF method cannot distinguish between these two motions.	None of them	[108]
	DoA	1 cm						None of them	[56]
	ToA/RSS and Spatial Sparsity	0.8 cm						None of them	[109]
Image-based	Hybrid video motion tracking & RF	2.3 cm	NO- The frames captured by the capsule are used for localization	No interference with the patient's mobility	NO- There is no internal reference used to measure the accurate displacement.	Fluctuation or inappropriate light. Poor quality imaging and low frames rate causes error in displacement measurement	Image-based localization is partially immune to peristalsis or involuntary motions, but more errors from the missing frames are introduced over time.	In vivo. The dataset from Pillcam	[110]
	RCNN	3.5 cm						In vitro validation	[45]
Ultrasound imaging	Ultrasonic and MRI	0.2 cm	NO- The capsule is implemented with MRI and ultrasound-friendly materials.	They perform at the hospital. In addition, a doctor or technician must be present at all times.	YES- All distances are measured based on the sensors' position. Hence, it is considered a fixed reference for localization.	Ultrasound's speed in different materials is the basis of displacement. However, it varies in other organs and human bodies, which may cause errors.	The GI organs are visible using this method; hence, we could compensate for the peristalsis motion.	None of them	[93]
Radiation imaging	MRI compatible	0.3 cm	NO- The capsule is implemented with MRI-friendly materials. Capsule	They performed at a hospital by lying on a bed. In addition, a doctor or technician	YES- The position is measured in coordinates of the MRI device	Electronic devices are not allowed because they cause problems with MRI devices and	The GI organs are visible using this method; hence, we could compensate for the peristalsis motion.	None of them	[111]

			fabrication is expensive.	must be present at all times. Risk of exposure to radiation		introduce noises. High level of radiation			
Magnetic	On-board magnetic sensing	0.5 cm	YES- A small magnet is installed inside the capsule.	An array of hall sensors is attached to the body, significantly limiting the patient's mobility.	YES- An array of hall sensors is required. Antennas must have fixed positions.	Interference with other sources of magnets. Such as ferromagnetic materials, wires with high current, etc.	Involuntary motion of the GI system inside the body leads to losing track of the capsule. Similar issues like RF methods	NO	[112]
	Jacobian-based iterative algorithm	0.7 cm						NO	[113]
	Magnetic sensing	0.5 cm						YES- In vivo validation on a porcine	[114]
Proposed method	IMU sensor and sidewall cameras	0.95 cm	YES- Sidewall camera and IMU sensor.	No additional hardware is required—no interference with the patient's mobility.	NO- Track from the beginning to the end of the GI path with no fixed reference point.	External magnetic fields may affect the IMU sensor.	Involuntary and peristalsis motions have no interference with the actual motion.	YES- In vitro validation on a porcine intestine	

Table 7.2 Comparing Method 2 with competitive WCE localization methods

	Localization method	**Positioning error (mm)**	**Considering GI involuntary motion**	**Degree of freedom**	**Number of sensors**	**Notes**
Method 2	Hybrid (magnetic and side wall camera)	3.5	YES	6	9 × Magnetometer 1 × Odometry	It gets global position from magnetic localization and fine-tunes the location using a side wall camera.
(2020) [38]	Hybrid (IMU and side wall camera)	± 3.71%	YES	7	1 × IMU 1 × Odometry	It suffers from an accumulation of errors and loses accuracy over time. It does not require an external reference point.
(2021) [84]	Magnetic	5.2	NO	6	16 × Magnetometer	Eliminate the geomagnetic fields noises by introducing differential signals
(2021) [86]	Magnetic	3.4	NO	6	12 × Magnetometer	An extension of [84]but placing the magnet sensor in a box belt.
(2019) [88]	Magnetic	10	NO	6	18 × Magnetometer	They mounted two extra noise cancellation sensors to reduce drifting error and improve initial guesses.
(2018) [64]	RF (TOA)	50	NO	3	17 × RF antenna	

7.3 Future works

Several future works can be done to take the research to the next level. They are listed below:

- To design and implement the capsule with a small footprint. This can be accomplished by using application-specific integrated circuit (ASIC) design. The side wall camera and optical lenses should be designed and optimized. A suitable capsule enclosure can be designed and printed using 3D printers with bio-compatible and acid-resistive materials.
- To perform experiments on animal trials.
- To integrate a digital camera and lighting system in the capsule to send live images of the GI tract. Then, upgrade the workstation software to label images by their position according to our proposed method. Finally, to create a 3D panoramic view of the entire GI tract.
- To investigate other hybrid methods for WCE localization that can distinguish between the capsule's motion and the relative motion of the GI system.
- To investigate the use of other biosensors, such as temperature, pH, etc., for enhancing localization accuracy.
- To investigate machine learning or other optimization techniques for improving localization accuracy.
- To further investigate magnetic localization and the effect of magnet configuration on the sensor belt.
- To integrate drug delivery, tissue sampling, etc. apparatuses into the capsule.

Publications

A list of publications is shown below, according to the correspondence of the thesis chapters, which are generated from the research during my doctoral program.

[1] S.S. Vedaei, K.A. Wahid, “A localization method for wireless capsule endoscopy using side wall cameras and IMU sensor,” *Scientific Reports*, vol. 11, no.1, pp. 11204-11220, 2021, doi: 10.1038/s41598-021-90523-w.

[2] S.S. Vedaei, K.A. Wahid, “MagnetOFuse: A Hybrid Tracking Algorithm for Wireless Capsule Endoscopy within the GI Track”, *IEEE Transactions on Instrumentation and Measurement*, doi: 10.1109/TIM.2022.3204103.

Other publications

[1] S. S. Vedaei, A. Fotovvat, *et.al.*, "COVID-SAFE: An IoT-Based System for Automated Health Monitoring and Surveillance in Post-Pandemic Life," *IEEE Access*, vol. 8, pp. 188538-188551, 2020, doi: 10.1109/ACCESS.2020.3030194.

[2] M. W. Alam, S. S. Vedaei and K. A. Wahid, “A Fluorescence-Based Wireless Capsule Endoscopy System for Detecting Colorectal Cancer,” *Cancers*, vol. 12, no. 4, 2020, doi: 10.3390/cancers12040890.

[3] M. R. Mohebbian, M. H. A. Sohag, S. S. Vedaei and K. A. Wahid, “Automated Detection of Bleeding in Capsule Endoscopy Using On-Chip Multispectral Imaging Sensors,” *IEEE Sensors Journal*, vol. 21, no. 13, pp. 14121-14130, 2021, doi: 10.1109/JSEN.2020.3034831.

[4] K. M. M. Rahman, S. K. Mohammed, S. S. Vedaei, M. R. Mohebbian, F. S. Chafjiri and K.Wahid, “A low complexity lossless Bayer CFA image compression,” *Signal, Image and Video Processing*, vol. 15, pp. 1767-1775, 2021, doi: 10.1007/s11760-021-01921-6.

[5] M. R. Mohebbian, S. S. Vedaei, K. A. Wahid, A. Dinh, H. R. Marateb and K. Tavakolian, "Fetal ECG Extraction From Maternal ECG Using Attention-Based CycleGAN," *IEEE Journal of Biomedical and Health Informatics*, vol. 26, no. 2, pp. 515-526, 2022, doi: 10.1109/JBHI.2021.3111873.

[6] A. Fotovvat, G. M. E. Rahman, S. S. Vedaei and K. A. Wahid, "Comparative Performance Analysis of Lightweight Cryptography Algorithms for IoT Sensor Nodes," *IEEE Internet of Things Journal*, vol. 8, no. 10, pp. 8279-8290, 15 May15, 2021, doi: 10.1109/JIOT.2020.3044526.

References

[1] J. S. H. Chan *et al.*, “Gastrointestinal disease burden and mortality: A public hospital-based study from 2005 to 2014,” *J. Gastroenterol. Hepatol.*, vol. 34, no. 1, pp. 124–131, Jan. 2019, doi: 10.1111/JGH.14377.

[2] E. Stolow, C. Moreau, H. Sayana, and S. Patel, “Management of Non-Variceal Upper GI Bleeding in the Geriatric Population: An Update,” *Curr. Gastroenterol. Rep.*, vol. 23, no. 4, pp. 1–10, Apr. 2021, doi: 10.1007/S11894-021-00805-6/TABLES/4.

[3] S. Romeo *et al.*, “Diagnostic yield of small bowel capsule endoscopy in obscure gastrointestinal bleeding: a real-world prospective study,” *Intern. Emerg. Med.*, vol. 17, no. 2, pp. 349–358, Mar. 2022, doi: 10.1007/S11739-021-02791-Z/TABLES/3.

[4] S. Fujimori, “Asymptomatic small intestinal ulcerative lesions: Obesity and Helicobacter pylori are likely to be risk factors,” *World J. Gastroenterol.*, vol. 27, no. 28, p. 4484, Jul. 2021, doi: 10.3748/WJG.V27.I28.4484.

[5] S. M. Hong, S. H. Jung, and D. H. Baek, “Diagnostic Yields and Clinical Impacts of Capsule Endoscopy,” *Diagnostics 2021, Vol. 11, Page 1842*, vol. 11, no. 10, p. 1842, Oct. 2021, doi: 10.3390/DIAGNOSTICS11101842.

[6] F. W. D. Tai *et al.*, “Panenteric capsule endoscopy identifies proximal small bowel disease guiding upstaging and treatment intensification in Crohn’s disease: A European multicentre observational cohort study,” *UEG J.*, vol. 9, no. 2, pp. 248–255, Mar. 2021, doi: 10.1177/2050640620948664.

[7] S. Iio *et al.*, “Capsule endoscopy findings reflect the gastrointestinal conditions of patients with systemic sclerosis,” *Sci. Reports 2021 111*, vol. 11, no. 1, pp. 1–8, Oct. 2021, doi: 10.1038/s41598-021-99775-y.

[8] F. E. R. Vuik *et al.*, “Colon capsule endoscopy in colorectal cancer screening: A systematic review,” *Endoscopy*, vol. 53, no. 8, pp. 815–824, Aug. 2021, doi: 10.1055/A-1308-1297/ID/JR18715-10.

[9] H. Mateen, R. Basar, A. U. Ahmed, and M. Y. Ahmad, “Localization of Wireless Capsule

Endoscope: A Systematic Review," *IEEE Sens. J.*, vol. 17, no. 5, pp. 1197–1206, Mar. 2017, doi: 10.1109/JSEN.2016.2645945.

[10] I. Dumic, T. Nordin, M. Jecmenica, M. Stojkovic Lalosevic, T. Milosavljevic, and T. Milovanovic, "Gastrointestinal Tract Disorders in Older Age," *Can. J. Gastroenterol. Hepatol.*, vol. 2019, 2019, doi: 10.1155/2019/6757524.

[11] Z. Liu *et al.*, "Comparison of new magnetic resonance imaging grading system with conventional endoscopy for the early detection of nasopharyngeal carcinoma," *Cancer*, vol. 127, no. 18, pp. 3403–3412, Sep. 2021, doi: 10.1002/CNCR.33552.

[12] G. Ciuti, A. Menciassi, and P. Dario, "Capsule endoscopy: From current achievements to open challenges," *IEEE Rev. Biomed. Eng.*, vol. 4, pp. 59–72, 2011, doi: 10.1109/RBME.2011.2171182.

[13] S. Diallo *et al.*, "Hepatic Artery Aneurysm: An Unusual Cause of Upper Gastrointestinal Bleed in 49 Years Old Patient," *Open J. Gastroenterol.*, vol. 12, no. 3, pp. 64–70, Mar. 2022, doi: 10.4236/OJGAS.2022.123007.

[14] Q.-W. Zhang and X.-B. Li, "Careful Observation Using Magnifying Endoscopy Before Choice of Treatment Strategy for Early Colorectal Lesions," *Endosc. Early Gastrointest. Cancers, Vol. 1*, vol. 1, pp. 153–160, 2021, doi: 10.1007/978-981-10-6769-3_17.

[15] A. G. Ionescu *et al.*, "Clinical impact of wireless capsule endoscopy for small bowel investigation (Review)," *Exp. Ther. Med.*, vol. 23, no. 4, pp. 1–9, Apr. 2022, doi: 10.3892/ETM.2022.11188.

[16] P. Swain, "The future of wireless capsule endoscopy," *World J. Gastroenterol.*, vol. 14, no. 26, pp. 4142–4145, 2008, doi: 10.3748/WJG.14.4142.

[17] Z. Fireman and Y. Kopelman, "New frontiers in capsule endoscopy," *J. Gastroenterol. Hepatol.*, vol. 22, no. 8, pp. 1174–1177, 2007, doi: 10.1111/J.1440-1746.2007.04993.X.

[18] C. Mc Caffrey, O. Chevalerias, C. O'Mathuna, and K. Twomey, "Swallowable-capsule technology," *IEEE Pervasive Comput.*, vol. 7, no. 1, pp. 23–29, Jan. 2008, doi: 10.1109/MPRV.2008.17.

[19] J. L. Toennies, G. Tortora, M. Simi, P. Valdastri, and R. J. Webster, “Swallowable medical devices for diagnosis and surgery: The state of the art,” *Proc. Inst. Mech. Eng. Part C J. Mech. Eng. Sci.*, vol. 224, no. 7, pp. 1397–1414, Jan. 2010, doi: 10.1243/09544062JMES1879.

[20] G. Iddan, G. Meron, A. Glukhovsky, and P. Swain, “Wireless capsule endoscopy.,” *Nature*, vol. 405, no. 6785, p. 417, May 2000, doi: 10.1038/35013140.

[21] U. Deding *et al.*, “Patient-Reported Outcomes and Preferences for Colon Capsule Endoscopy and Colonoscopy: A Systematic Review with Meta-Analysis,” *Diagnostics 2021, Vol. 11, Page 1730*, vol. 11, no. 9, p. 1730, Sep. 2021, doi: 10.3390/DIAGNOSTICS11091730.

[22] M. Mascarenhas, J. Afonso, P. Andrade, H. Cardoso, and G. Macedo, “Artificial intelligence and capsule endoscopy: unravelling the future,” *Ann. Gastroenterol.*, vol. 34, no. 3, p. 300, 2021, doi: 10.20524/AOG.2021.0606.

[23] M. R. Mohebbian, M. H. A. Sohag, S. S. Vedaei, and K. A. Wahid, “Automated Detection of Bleeding in Capsule Endoscopy Using On-Chip Multispectral Imaging Sensors,” *IEEE Sens. J.*, vol. 21, no. 13, pp. 14121–14130, Jul. 2021, doi: 10.1109/JSEN.2020.3034831.

[24] F. Deeba, F. M. Bui, and K. A. Wahid, “Computer-aided polyp detection based on image enhancement and saliency-based selection,” *Biomed. Signal Process. Control*, vol. 55, p. 101530, Jan. 2020, doi: 10.1016/j.bspc.2019.04.007.

[25] M. Souaidi and M. El Ansari, “A New Automated Polyp Detection Network MP-FSSD in WCE and Colonoscopy Images Based Fusion Single Shot Multibox Detector and Transfer Learning,” *IEEE Access*, vol. 10, pp. 47124–47140, 2022, doi: 10.1109/ACCESS.2022.3171238.

[26] Z. Falin, L. Haihua, and P. Ning, “Gastrointestinal Polyps and Tumors Detection Based on Multi-scale Feature-fusion with WCE Sequences,” Apr. 2022, doi: 10.48550/arxiv.2204.01012.

[27] P. M. Vieira, N. R. Freitas, V. B. Lima, D. Costa, C. Rolanda, and C. S. Lima, “Multi-pathology detection and lesion localization in WCE videos by using the instance

segmentation approach," *Artif. Intell. Med.*, vol. 119, p. 102141, Sep. 2021, doi: 10.1016/J.ARTMED.2021.102141.

[28] A. Eshkevari and S. M. S. Sadough, "An Improved Method for Localization of Wireless Capsule Endoscope Using Direct Position Determination," *IEEE Access*, vol. 9, pp. 154563–154577, 2021, doi: 10.1109/ACCESS.2021.3128748.

[29] Y. Wang, S. Yoo, J. M. Braun, and E. S. Nadimi, "A locally-processed light-weight deep neural network for detecting colorectal polyps in wireless capsule endoscopes," *J. Real-Time Image Process.*, vol. 18, no. 4, pp. 1183–1194, Aug. 2021, doi: 10.1007/S11554-021-01126-7/TABLES/9.

[30] P. B. Pedersen, D. Bar-Shalom, S. Baldursdottir, P. Vilmann, and A. Müllertz, "Feasibility of Capsule Endoscopy for Direct Imaging of Drug Delivery Systems in the Fasted Upper-Gastrointestinal Tract," *Pharm. Res. 2014 318*, vol. 31, no. 8, pp. 2044–2053, Feb. 2014, doi: 10.1007/S11095-014-1306-6.

[31] N. Takase *et al.*, "Preoperative detection and localization of small bowel hemangioma: Two case reports," *World J. Gastroenterol.*, vol. 23, no. 20, pp. 3752–3757, May 2017, doi: 10.3748/WJG.V23.I20.3752.

[32] J. C. Martinez, J. L. Thomas, and J. J. Lukaszczyk, "Single incision laparoscopic surgery approach for obscure small intestine bleeding localized by CT guided percutaneous injection of methylene blue," *Int. J. Surg. Case Rep.*, vol. 5, no. 12, p. 1082, 2014, doi: 10.1016/J.IJSCR.2014.06.020.

[33] Y. Xu *et al.*, "A Review of magnetic sensor-based positioning techniques for capsule endoscopy," *Int. Arch. Photogramm. Remote Sens. Spat. Inf. Sci. - ISPRS Arch.*, vol. 46, no. 3/W1-2022, pp. 219–226, 2022, doi: 10.5194/ISPRS-ARCHIVES-XLVI-3-W1-2022-219-2022.

[34] F. Bianchi *et al.*, "Localization strategies for robotic endoscopic capsules: a review," *https://doi.org/10.1080/17434440.2019.1608182*, vol. 16, no. 5, pp. 381–403, May 2019, doi: 10.1080/17434440.2019.1608182.

[35] K. Muhammad, S. Khan, N. Kumar, J. Del Ser, and S. Mirjalili, "Vision-based

personalized Wireless Capsule Endoscopy for smart healthcare: Taxonomy, literature review, opportunities and challenges," *Futur. Gener. Comput. Syst.*, vol. 113, pp. 266–280, Dec. 2020, doi: 10.1016/J.FUTURE.2020.06.048.

[36] A. A. Mohd Faudzi, Y. Sabzehmeidani, and N. K. Al-Shammari, "Innovations of Wireless Capsule Robots in Gastrointestinal Endoscopy: A Review," *Adv. Intell. Syst. Comput.*, vol. 1223, pp. 99–109, 2021, doi: 10.1007/978-3-030-52180-6_12/FIGURES/4.

[37] Q. François, A. André, B. Duplat, S. Haliyo, and S. Régnier, "Tracking systems for intracranial medical devices: A review," *Med. Devices Sensors*, vol. 2, no. 2, p. e10033, Apr. 2019, doi: 10.1002/MDS3.10033.

[38] S. S. Vedaei and K. A. Wahid, "A localization method for wireless capsule endoscopy using side wall cameras and IMU sensor," *Sci. Reports 2021 111*, vol. 11, no. 1, pp. 1–16, May 2021, doi: 10.1038/s41598-021-90523-w.

[39] "Welcome to Olympus - Olympus EMEA." https://www.olympus-europa.com/ (accessed Jun. 17, 2022).

[40] "IntroMedic." https://www.intromedic.com:549/eng/main/ (accessed Jun. 17, 2022).

[41] "Capsule Endoscopy Products | Medtronic." https://www.medtronic.com/covidien/en-us/products/capsule-endoscopy.html (accessed Jun. 17, 2022).

[42] P. Narmatha, V. Thangavel, and D. S. Vidhya, "A Hybrid RF and Vision Aware Fusion Scheme for Multi-Sensor Wireless Capsule Endoscopic Localization," *Wirel. Pers. Commun.*, vol. 123, no. 2, pp. 1593–1624, Mar. 2022, doi: 10.1007/S11277-021-09205-5/TABLES/6.

[43] B. Jiang, Y. Zhang, M. Wu, J. Li, and J. Yu, "Consistent wce video frame interpolation based on endoscopy image motion estimation," *Proc. - Int. Symp. Biomed. Imaging*, vol. 2021-April, pp. 334–338, Apr. 2021, doi: 10.1109/ISBI48211.2021.9434049.

[44] Y. Xu, K. Li, and M. Q. H. Meng, "Unsupervised learning based relative localization for WCE in a deformable tubular environment," *2021 6th IEEE Int. Conf. Adv. Robot. Mechatronics, ICARM 2021*, pp. 119–124, Jul. 2021, doi: 10.1109/ICARM52023.2021.9536182.

[45] M. Turan, Y. Almalioglu, H. Araujo, E. Konukoglu, and M. Sitti, “Deep EndoVO: A recurrent convolutional neural network (RCNN) based visual odometry approach for endoscopic capsule robots,” *Neurocomputing*, vol. 275, pp. 1861–1870, Jan. 2018, doi: 10.1016/j.neucom.2017.10.014.

[46] A. Koulaouzidis *et al.*, “Novel experimental and software methods for image reconstruction and localization in capsule endoscopy,” *Endosc. Int. Open*, vol. 06, no. 02, pp. E205–E210, Feb. 2018, doi: 10.1055/s-0043-121882.

[47] M. Mackiewicz, J. Berens, and M. Fisher, “Wireless capsule endoscopy color video segmentation,” *IEEE Trans. Med. Imaging*, vol. 27, no. 12, pp. 1769–1781, Dec. 2008, doi: 10.1109/TMI.2008.926061.

[48] J. P. S. Cunha, M. Coimbra, P. Campos, and J. M. Soares, “Automated topographic segmentation and transit time estimation in endoscopic capsule exams,” *IEEE Trans. Med. Imaging*, vol. 27, no. 1, pp. 19–27, Jan. 2008, doi: 10.1109/TMI.2007.901430.

[49] H. Vu *et al.*, “Color analysis for segmenting digestive organs in VCE,” *Proc. - Int. Conf. Pattern Recognit.*, pp. 2468–2471, 2010, doi: 10.1109/ICPR.2010.604.

[50] N. Marques, E. Dias, J. P. S. Cunha, and M. Coimbra, “Compressed domain topographic classification for capsule endoscopy.,” *Annu. Int. Conf. IEEE Eng. Med. Biol. Soc. IEEE Eng. Med. Biol. Soc. Annu. Int. Conf.*, vol. 2011, pp. 6631–6634, Jan. 2011, doi: 10.1109/IEMBS.2011.6091635.

[51] Y. Shen, P. P. Guturu, and B. P. Buckles, “Wireless Capsule Endoscopy Video Segmentation Using an Unsupervised Learning Approach Based on Probabilistic Latent Semantic Analysis With Scale Invariant Features,” *IEEE Trans. Inf. Technol. Biomed.*, vol. 16, no. 1, pp. 98–105, Jan. 2012, doi: 10.1109/TITB.2011.2171977.

[52] G. Bao and K. Pahlavai, “Motion estimation of the endoscopy capsule using region-based Kernel SVM classifier,” *IEEE Int. Conf. Electro Inf. Technol.*, 2013, doi: 10.1109/EIT.2013.6632652.

[53] G. Bao, L. Mi, Y. Geng, M. Zhou, and K. Pahlavan, “A video-based speed estimation technique for localizing the wireless capsule endoscope inside gastrointestinal tract,” *2014*

36th Annu. Int. Conf. IEEE Eng. Med. Biol. Soc. EMBC 2014, pp. 5615–5618, Nov. 2014, doi: 10.1109/EMBC.2014.6944900.

[54] G. Dimas, E. Spyrou, D. K. Iakovidis, and A. Koulaouzidis, "Intelligent visual localization of wireless capsule endoscopes enhanced by color information," *Comput. Biol. Med.*, vol. 89, pp. 429–440, Oct. 2017, doi: 10.1016/J.COMPBIOMED.2017.08.029.

[55] A. R. Nafchi, S. T. Goh, and S. A. R. Zekavat, "Circular arrays and inertial measurement unit for DOA/TOA/TDOA-based endoscopy capsule localization: Performance and complexity investigation," *IEEE Sens. J.*, vol. 14, no. 11, pp. 3791–3799, Nov. 2014, doi: 10.1109/JSEN.2014.2331244.

[56] S. T. Goh, S. A. R. Zekavat, and K. Pahlavan, "DOA-based endoscopy capsule localization and orientation estimation via unscented kalman filter," *IEEE Sens. J.*, vol. 14, no. 11, pp. 3819–3829, Nov. 2014, doi: 10.1109/JSEN.2014.2342720.

[57] C. Hekimian-Williams, B. Grant, X. Liu, Z. Zhang, and P. Kumar, "Accurate localization of RFID tags using phase difference," *RFID 2010 Int. IEEE Conf. RFID*, pp. 89–96, 2010, doi: 10.1109/RFID.2010.5467268.

[58] Y. Wang, R. Fu, Y. Ye, U. Khan, and K. Pahlavan, "Performance bounds for RF positioning of endoscopy camera capsules," *2011 IEEE Radio Wirel. Week, RWW 2011 - 2011 IEEE Top. Conf. Biomed. Wirel. Technol. Networks, Sens. Syst. BioWireleSS 2011*, pp. 71–74, 2011, doi: 10.1109/BIOWIRELESS.2011.5724349.

[59] R. Chandra, A. J. Johansson, and F. Tufvesson, "Localization of an RF source inside the human body for wireless capsule endoscopy," *BODYNETS 2013 - 8th Int. Conf. Body Area Networks*, pp. 48–54, Oct. 2013, doi: 10.4108/ICST.BODYNETS.2013.253713.

[60] P. Brida and J. MacHaj, "A novel enhanced positioning trilateration algorithm implemented for medical implant in-body localization," *Int. J. Antennas Propag.*, vol. 2013, 2013, doi: 10.1155/2013/819695.

[61] G. Bao, L. Mi, and K. Pahlavan, "A video aided RF localization technique for the wireless capsule endoscope (WCE) inside small intestine," *BODYNETS 2013 - 8th Int. Conf. Body Area Networks*, pp. 55–61, Oct. 2013, doi: 10.4108/ICST.BODYNETS.2013.253642.

[62] T. Ito, D. Anzai, and J. Wang, “A Modified Particle Filter Algorithm for Wireless Capsule Endoscope Location Tracking,” Nov. 2013, doi: 10.4108/ICST.BODYNETS.2013.253650.

[63] B. Moussakhani, R. Chavez-Santiago, and I. Balasingham, “Multi model tracking for localization in wireless capsule endoscopes,” *ACM Int. Conf. Proceeding Ser.*, 2011, doi: 10.1145/2093698.2093857.

[64] U. Khan, Y. Ye, A. U. Aisha, P. Swar, and K. Pahlavan, “Precision of em Simulation Based Wireless Location Estimation in Multi-Sensor Capsule Endoscopy,” *IEEE J. Transl. Eng. Heal. Med.*, vol. 6, Mar. 2018, doi: 10.1109/JTEHM.2018.2818177.

[65] C. Xu, J. He, Y. Li, X. Zhang, X. Zhou, and S. Duan, “Optimal estimation and fundamental limits for target localization using IμTOA fusion method,” *IEEE Access*, vol. 7, pp. 28124–28136, 2019, doi: 10.1109/ACCESS.2019.2902127.

[66] G. Cummins *et al.*, “Gastrointestinal diagnosis using non-white light imaging capsule endoscopy,” *Nat. Rev. Gastroenterol. Hepatol.*, vol. 16, no. 7, pp. 429–447, 2019, doi: 10.1038/s41575-019-0140-z.

[67] S. Zeising, A. Thalmayer, G. Fischer, and J. Kirchner, “Toward Magnetic Localization of Capsule Endoscopes during Daily Life Activities,” *Proc. 2021 Kleinheubach Conf. KHB 2021*, Sep. 2021, doi: 10.23919/IEEECONF54431.2021.9598378.

[68] Y. Xu, K. Li, Z. Zhao, and M. Q. H. Meng, “Adaptive Simultaneous Magnetic Actuation and Localization for WCE in a Tubular Environment,” *IEEE Trans. Robot.*, 2022, doi: 10.1109/TRO.2022.3161766.

[69] S. Zeising, D. Anzai, A. Thalmayer, G. Fischer, and J. Kirchner, “Innovative Differential Magnetic Localization Method for Capsule Endoscopy to Prevent Interference Caused by the Geomagnetic Field,” *Adv. Radio Sci.*, vol. 19, pp. 207–213, Dec. 2021, doi: 10.5194/ARS-19-207-2021.

[70] S. Song, X. Qiu, J. Wang, and M. Q. H. Meng, “Design and Optimization Strategy of Sensor Array Layout for Magnetic Localization System,” *IEEE Sens. J.*, vol. 17, no. 6, pp. 1849–1857, Mar. 2017, doi: 10.1109/JSEN.2017.2652470.

[71] S. Song, X. Qiu, J. Wang, and M. Q. H. Meng, “Real-Time Tracking and Navigation for Magnetically Manipulated Untethered Robot,” *IEEE Access*, vol. 4, pp. 7104–7110, 2016, doi: 10.1109/ACCESS.2016.2618949.

[72] W. Yang, C. Hu, M. Li, M. Q. H. Meng, and S. Song, “A new tracking system for three magnetic objectives,” *IEEE Trans. Magn.*, vol. 46, no. 12, pp. 4023–4029, Dec. 2010, doi: 10.1109/TMAG.2010.2076823.

[73] Y. Xu, K. Li, and M. Q. H. Meng, “A Novel Approach for Automatic State Detection of A Magnetically Actuated Capsule,” *Annu. Int. Conf. IEEE Eng. Med. Biol. Soc. IEEE Eng. Med. Biol. Soc. Annu. Int. Conf.*, vol. 2020, pp. 4766–4769, Jul. 2020, doi: 10.1109/EMBC44109.2020.9176691.

[74] Y. Xu, Z. Zhao, K. Li, and M. Q. H. Meng, “Towards external sensor based simultaneous magnetic actuation and localization for WCE,” *IEEE Int. Conf. Robot. Biomimetics, ROBIO 2019*, pp. 2332–2337, Dec. 2019, doi: 10.1109/ROBIO49542.2019.8961756.

[75] Y. Xu, K. Li, Z. Zhao, and M. Q. H. Meng, “A Novel System for Closed-Loop Simultaneous Magnetic Actuation and Localization of WCE Based on External Sensors and Rotating Actuation,” *IEEE Trans. Autom. Sci. Eng.*, vol. 18, no. 4, pp. 1640–1652, Oct. 2021, doi: 10.1109/TASE.2020.3013954.

[76] K. M. Popek, A. W. Mahoney, and J. J. Abbott, “Localization method for a magnetic capsule endoscope propelled by a rotating magnetic dipole field,” *Proc. - IEEE Int. Conf. Robot. Autom.*, pp. 5348–5353, 2013, doi: 10.1109/ICRA.2013.6631343.

[77] A. W. Mahoney and J. J. Abbott, “Generating rotating magnetic fields with a single permanent magnet for propulsion of untethered magnetic devices in a Lumen,” *IEEE Trans. Robot.*, vol. 30, no. 2, pp. 411–420, 2014, doi: 10.1109/TRO.2013.2289019.

[78] V. Cavlu and P. Brennan, “Determining the Position and Orientation of In-Body Medical Instruments Using Near-Field Magnetic Field Mapping,” *IEEE J. Electromagn. RF Microwaves Med. Biol.*, vol. 4, no. 1, pp. 10–16, Mar. 2020, doi: 10.1109/JERM.2019.2914402.

[79] R. Shimizu, R. Shirai, and M. Hashimoto, “Position and Posture Estimation of Capsule

Endoscopy with a Single Wearable Coil Toward Daily Life Diagnosis," *Midwest Symp. Circuits Syst.*, vol. 2020-August, pp. 57–60, Aug. 2020, doi: 10.1109/MWSCAS48704.2020.9184448.

[80] K. Li, Y. Xu, Z. Zhao, and M. Q.-H. Meng, "External and Internal Sensor Fusion Based Localization Strategy for 6-DOF Pose Estimation of a Magnetic Capsule Robot," *IEEE Robot. Autom. Lett.*, vol. 7, no. 3, pp. 6878–6885, Jul. 2022, doi: 10.1109/LRA.2022.3178473.

[81] S. Zeising, K. Ararat, A. Thalmayer, D. Anzai, G. Fischer, and J. Kirchner, "Systematic Performance Evaluation of a Novel Optimized Differential Localization Method for Capsule Endoscopes," *Sensors 2021, Vol. 21, Page 3180*, vol. 21, no. 9, p. 3180, May 2021, doi: 10.3390/S21093180.

[82] "A Study on Simultaneous Magnetic Actuation and Localization Based Robotic Navigation System for Active Wireless Capsule Endoscopy - ProQuest." https://www.proquest.com/docview/2650007215?pq-origsite=gscholar&fromopenview=true (accessed Jun. 18, 2022).

[83] Y. Fu and Y. X. Guo, "Wearable Permanent Magnet Tracking System for Wireless Capsule Endoscope," *IEEE Sens. J.*, vol. 22, no. 8, pp. 8113–8122, Apr. 2022, doi: 10.1109/JSEN.2022.3153896.

[84] S. Song, S. Wang, S. Yuan, J. Wang, W. Liu, and M. Q. H. Meng, "Magnetic Tracking of Wireless Capsule Endoscope in Mobile Setup Based on Differential Signals," *IEEE Trans. Instrum. Meas.*, vol. 70, 2021, doi: 10.1109/TIM.2021.3069488.

[85] Q. Ji, "Foundation and basics," *Probabilistic Graph. Model. Comput. Vis.*, pp. 11–29, Jan. 2020, doi: 10.1016/B978-0-12-803467-5.00007-1.

[86] S. Zeising, A. Thalmayer, G. Fischer, and J. Kirchner, "Differential Geomagnetic Compensation Method for the Static Magnetic Localization of Capsule Endoscopes during Activities of the Daily Life," *IEEE Trans. Instrum. Meas.*, vol. 71, 2022, doi: 10.1109/TIM.2021.3129206.

[87] P. S. Boroujeni, H. N. Pishkenari, H. Moradi, and G. Vossoughi, "Model-Aided Real-

Time Localization and Parameter Identification of a Magnetic Endoscopic Capsule Using Extended Kalman Filter," *IEEE Sens. J.*, vol. 21, no. 12, pp. 13667–13675, Jun. 2021, doi: 10.1109/JSEN.2021.3071432.

[88] G. Shao, Y. Tang, L. Tang, Q. Dai, and Y. X. Guo, "A Novel Passive Magnetic Localization Wearable System for Wireless Capsule Endoscopy," *IEEE Sens. J.*, vol. 19, no. 9, pp. 3462–3472, May 2019, doi: 10.1109/JSEN.2019.2894386.

[89] Y. Xu, K. Li, Z. Zhao, and M. Q. H. Meng, "Improved Multiple Objects Tracking based Autonomous Simultaneous Magnetic Actuation & Localization for WCE," *Proc. - IEEE Int. Conf. Robot. Autom.*, pp. 5523–5529, May 2020, doi: 10.1109/ICRA40945.2020.9197142.

[90] H. Kobayashi, D. Anzai, and J. Wang, "Em imaging-based capsule endoscope localization with peak-formed incident electric fields," *EAI/Springer Innov. Commun. Comput.*, vol. 3, pp. 399–405, 2020, doi: 10.1007/978-3-030-29897-5_35/FIGURES/6.

[91] K. Li *et al.*, "Autonomous Navigation of an Ultrasound Probe Towards Standard Scan Planes with Deep Reinforcement Learning," *Proc. - IEEE Int. Conf. Robot. Autom.*, vol. 2021-May, pp. 8302–8308, 2021, doi: 10.1109/ICRA48506.2021.9561295.

[92] "US20060285638A1 - Method for determining the position and orientation of an object, especially of a catheter, from two-dimensional X-ray images - Google Patents." https://patents.google.com/patent/US20060285638A1/en (accessed Jun. 17, 2022).

[93] N. Pagoulatos, W. S. Edwards, D. R. Haynor, and Y. Kim, "Interactive 3-D registration of ultrasound and magnetic resonance images based on a magnetic position sensor," *IEEE Trans. Inf. Technol. Biomed.*, vol. 3, no. 4, pp. 278–288, 1999, doi: 10.1109/4233.809172.

[94] K. Kalantar-Zadeh *et al.*, "A human pilot trial of ingestible electronic capsules capable of sensing different gases in the gut," *Nat. Electron.*, vol. 1, no. 1, pp. 79–87, Jan. 2018, doi: 10.1038/s41928-017-0004-x.

[95] F. N. Alsunaydih, M. S. Arefin, J. M. Redoute, and M. R. Yuce, "A Navigation and Pressure Monitoring System Toward Autonomous Wireless Capsule Endoscopy," *IEEE Sens. J.*, vol. 20, no. 14, pp. 8098–8107, Jul. 2020, doi: 10.1109/JSEN.2020.2979513.

[96] A. Noureldin, T. B. Karamat, and J. Georgy, “Fundamentals of inertial navigation, satellite-based positioning and their integration,” *Fundam. Inert. Navig. Satell. Position. their Integr.*, pp. 1–313, Jan. 2013, doi: 10.1007/978-3-642-30466-8/COVER.

[97] D. Fernandez and A. Price, “Visual odometry for an outdoor mobile robot,” *2004 IEEE Conf. Robot. Autom. Mechatronics*, pp. 816–821, 2004, doi: 10.1109/RAMECH.2004.1438023.

[98] N. Nourani-Vatani, J. Roberts, and M. V. Srinivasan, “Practical visual odometry for car-like vehicles,” *Proc. - IEEE Int. Conf. Robot. Autom.*, pp. 3551–3557, 2009, doi: 10.1109/ROBOT.2009.5152403.

[99] H. C. Lee, C. W. Jung, and H. C. Kim, “Real-time endoscopic image orientation correction system using an accelerometer and gyrosensor,” *PLoS One*, vol. 12, no. 11, Nov. 2017, doi: 10.1371/journal.pone.0186691.

[100] W. Koo, S. Sung, and Y. J. Lee, “Error calibration of magnetometer using nonlinear integrated filter model with inertial sensors,” *IEEE Trans. Magn.*, vol. 45, no. 6, pp. 2740–2743, 2009, doi: 10.1109/TMAG.2009.2020542.

[101] L. Wang, Z. Zhang, and P. Sun, “Quaternion-Based Kalman Filter for AHRS Using an Adaptive-Step Gradient Descent Algorithm:,” *https://doi.org/10.5772/61313*, vol. 12, no. 9, Jan. 2015, doi: 10.5772/61313.

[102] D. Roetenberg, H. J. Luinge, C. T. M. Baten, and P. H. Veltink, “Compensation of magnetic disturbances improves inertial and magnetic sensing of human body segment orientation,” *IEEE Trans. Neural Syst. Rehabil. Eng.*, vol. 13, no. 3, pp. 395–405, Sep. 2005, doi: 10.1109/TNSRE.2005.847353.

[103] D. L. Means and K. W. Chan, “Evaluating Compliance with FCC Guidelines for Human Exposure to Radiofrequency Electromagnetic Fields Additional Information for Evaluating Compliance of Mobile and Portable Devices with FCC Limits for Human Exposure to Radiofrequency Emissions AUTHORS,” 2001, Accessed: Jun. 17, 2022. [Online]. Available: http://www.fcc.gov/oet/.

[104] S. H. Lee *et al.*, “A wideband spiral antenna for ingestible capsule endoscope systems:

Experimental results in a human phantom and a pig," *IEEE Trans. Biomed. Eng.*, vol. 58, no. 6, pp. 1734–1741, Jun. 2011, doi: 10.1109/TBME.2011.2112659.

[105] T. H. Khan and K. A. Wahid, "An advanced physiological data logger for medical imaging applications," *Eurasip J. Embed. Syst.*, vol. 2012, no. 1, pp. 1–14, Dec. 2012, doi: 10.1186/1687-3963-2012-10/TABLES/7.

[106] O. F. Aje, A. A. Josephat, O. F. Aje, and A. A. Josephat, "The particle swarm optimization (PSO) algorithm application – A review," *http://gjeta.com/sites/default/files/GJETA-2020-0033.pdf*, vol. 3, no. 3, pp. 001–006, Jun. 2020, doi: 10.30574/GJETA.2020.3.3.0033.

[107] M. Suzan Miah, A. N. Khan, C. Icheln, K. Haneda, and K. I. Takizawa, "Antenna system design for improved wireless capsule endoscope links at 433 MHz," *IEEE Trans. Antennas Propag.*, vol. 67, no. 4, pp. 2687–2699, Apr. 2019, doi: 10.1109/TAP.2019.2900389.

[108] T. Ito, D. Anzai, and J. Wang, "Novel joint TOA/RSSI-based WCE location tracking method without prior knowledge of biological human body tissues," in *2014 36th Annual International Conference of the IEEE Engineering in Medicine and Biology Society, EMBC 2014*, Nov. 2014, vol. 2014, pp. 6993–6996, doi: 10.1109/EMBC.2014.6945237.

[109] M. Pourhomayoun, Z. Jin, and M. L. Fowler, "Accurate localization of in-body medical implants based on spatial sparsity," *IEEE Trans. Biomed. Eng.*, vol. 61, no. 2, pp. 590–597, Feb. 2014, doi: 10.1109/TBME.2013.2284271.

[110] G. Bao, K. Pahlavan, and L. Mi, "Hybrid Localization of Microrobotic Endoscopic Capsule Inside Small Intestine by Data Fusion of Vision and RF Sensors," *IEEE Sens. J.*, vol. 15, no. 5, pp. 2669–2678, May 2015, doi: 10.1109/JSEN.2014.2367495.

[111] A. Krieger *et al.*, "An MRI-compatible robotic system with hybrid tracking for MRI-guided prostate intervention," *IEEE Trans. Biomed. Eng.*, vol. 58, no. 11, pp. 3049–3060, Nov. 2011, doi: 10.1109/TBME.2011.2134096.

[112] M. Salerno *et al.*, "A discrete-time localization method for capsule endoscopy based on on-board magnetic sensing," *Meas. Sci. Technol.*, vol. 23, no. 1, p. 015701, Nov. 2012,

doi: 10.1088/0957-0233/23/1/015701.

[113] C. Di Natali, M. Beccani, N. Simaan, and P. Valdastri, “Jacobian-Based Iterative Method for Magnetic Localization in Robotic Capsule Endoscopy,” *IEEE Trans. Robot.*, vol. 32, no. 2, pp. 327–338, Apr. 2016, doi: 10.1109/TRO.2016.2522433.

[114] D. M. Pham and S. M. Aziz, “A real-time localization system for an endoscopic capsule using magnetic sensors,” *Sensors (Switzerland)*, vol. 14, no. 11, pp. 20910–20929, Nov. 2014, doi: 10.3390/s141120910.